Light-Induced Crystallization of Germanium Diselenide Glass and Its Medium Range Structures

by

Osamu Matsuda

DISSERTATION IN PHYSICS

THE OSAKA UNIVERSITY

GRADUATE SCHOOL OF SCIENCE

TOYONAKA, OSAKA

Light-Induced Crystallization of Germanium Diselenide Glass and Its Medium Range Structures

by

Osamu Matsuda

Dissertation in Physics

Department of Physics

Faculty of Science

Osaka University

1991

Contents

List of Tables

List of Figures

Abstract

For the understanding of the light-induced crystallization process in amorphous $GeSe_2$, the vibrational and the electronic structures in crystalline and amorphous $GeSe_2$ are studied in detail by Raman scattering experiment with various excitation photon energies and by optical absorption experiment.

In the Raman spectra of single crystals, we have found resonance effects which connect electronic excitations (excitons) with lattice vibrations. With usual non-resonant excitation, there are one strong band at about 211 cm^{-1} and one weak band at about 216 cm^{-1} in the Raman spectra in the region between 190 and 220 cm^{-1}. At the excitation of 2.71 eV at RT, which corresponds to the exciton transition energy 2.70 eV at RT, the 216 cm^{-1} band increases in its intensity at the expense of the 211 cm^{-1} band. The relation between the resonance effect and the exciton transition is confirmed by a temperature-tuning of an exciton transition energy at low temperatures; the resonance effect is observed at the 2.81 eV excitation around 200 K where the exciton transition energy becomes close to the excitation energy.

In relation to this resonance experiment, it is concluded that 1) the 211 cm^{-1} band is ascribed to the breathing motion extended over the corner-sharing $GeSe_{4/2}$ tetrahedra which form chains in the crystal, whereas the 216 cm^{-1} band is ascribed to the breathing motion quasi-localized at the edge-sharing $Ge_2Se_{8/2}$ bi-tetrahedra which connect the chains mutually like bridges. 2) The initial state of the 2.70 eV exciton transition is the Se $4p$ lone-pair states at the edge-sharing $Ge_2Se_{8/2}$ bi-tetrahedra and the exciton is quasi-localized at the edge-sharing bi-tetrahedra. 3) The resonant effect comes from a strong interaction between the 216 cm^{-1} vibration and the 2.70 eV exciton.

In the absorption spectra of the polycrystalline films, it is found that the exciton transition energy, which is 2.70 eV in the single crystal, is significantly lowered by disorder in the polycrystals. The resonant Raman effect is also observed in the polycrystals at the excitation energy near the exciton transition energy. The

observation of the resonance provides a powerful method to investigate the disorder in the crystal.

In the Raman spectra of amorphous $GeSe_2$ in the region between 190 and 220 cm^{-1}, there are two bands, A_1 and A_1^C, corresponding to the breathing vibration of the $GeSe_{4/2}$ tetrahedra. Among single-crystalline, polycrystalline, and amorphous $GeSe_2$, the degree of disorder in samples is considered to increase in this series. We explain the energy splitting between two breathing modes, A_1 and A_1^C, by a structural model where topologically layered-crystal-like fragments are contained in the amorphous state. The A_1 band corresponds to the crystalline 211 cm^{-1} band, and the A_1^C band, to the 216 cm^{-1} band.

The resonant Raman experiment of the light-induced crystals also shows the lowering of the exciton transition energy, which suggests that the light-induced crystal is significantly disordered. The light-induced crystallization process at various environmental temperatures is investigated by the time-resolved Raman experiment. It is concluded that the photo-crystallization is not caused by a pure thermal process. The electronic excitation by light irradiation is essentially important in the crystallization. The coupling between electronic excitations and lattice vibrations is also important in the light-induced crystallization process. In a pure thermal crystallization, the final states of the crystallization, which are two modifications of the $GeSe_2$ crystal, α–$GeSe_2$ (three dimensional form) and β–$GeSe_2$ (layered form), are uniquely destined by the annealing temperature through a thermal equilibrium process. On the other hand, the final crystalline state of the light-induced crystallization, that is the type A (β–$GeSe_2$) or the type B (α–$GeSe_2$ + β–$GeSe_2$), depends on medium-range structures in the initial amorphous state which has been frozen in by the glass forming process.

Acknowledgments

The author wishes to express his sincere gratitude for the valuable suggestions and continuous encouragements and supports from Professor K. Murase throughout this research. He is also very indebted to Dr. K. Inoue for guidance on the experiment, stimulating discussion, calculation on the vibrational modes, and valuable advice in this research. He thanks Mr. T. Katayama and Mr. K. Kawamoto for their guidance on the experiment. He also thanks Mr. T. Wakabayashi, Mr. K. Oto, and Mr. H. Okada for their assistances in the experiment on the light-induced crystallization, Mr. T. Nakane, Mr. A. Otani, Mr. H. Sato, and Mr. K. Tanaka for their assistances in the resonant Raman experiment of the polycrystalline films. He is also grateful to Dr. S. Takaoka and Dr. S. Sugai for their various suggestions on the experiment and writing this manuscript.

The author would like to thank Professor Y. Mori and the staff of Ohkura Laboratory at Osaka City University for the photo-luminescence experiment, to Professor S. Kashida in Niigata University for the X–ray analysis of the crystalline axes, to the staff of the Crystallographic Research Center, Institute for Protein Research, Osaka University, for the use of the precession camera in the X-ray analysis of the crystalline axes, and to the staff of the X–ray Diffraction Service of the Department of Chemistry, Faculty of Science, Osaka University for the X-ray powder diffraction measurement.

Finally the author thanks all the members of Murase Laboratory for their encouragements during this study.

1 Introduction

Chalcogenide amorphous semiconductors are the compounds containing chalcogen elements (S, Se, and Te) and elements of group IV and/or V (Si, Ge, P, As, etc.), for example Ge_xSe_{1-x}, Ge_xS_{1-x}, As_xSe_{1-x}, etc..[1] These compounds are roughly characterized by following two features: 1) over the wide range of the composition ratio of the chalcogen element to the other constituents, one can easily obtain glassy forms of the compounds which have various physical properties (energy gap value, for example) depending on the composition ratio. At a stoichiometric composition, a crystalline form can also be obtained. Thus the compounds are good objects to study the physics of glass by comparing the properties of the glassy form with those of the crystalline form. 2) In the glassy form, the compounds show various kinds of light-induced persistent or transient structural changes such as:

- Photo-darkening:[2] Narrowing of the optical energy-gap induced by irradiation of light.
- Photo-bleaching:[3] Widening of the optical gap by the irradiation of light.
- Photo-crystallization (light-induced crystallization):[4,5] Crystallization by the irradiation of light.
- Photo-doping:[6] Doping of some metal atoms into the glass by the irradiation of light.

These structural changes are not only intriguing in the solid state physics but also important from the viewpoint of industrial application. The phenomena of the light-induced structural changes can be applied to the optical erasable and ultra-high-density mass-memories,[7] to the photo-resist materials for the micro-fabrication,[8,9] and so on.

The purpose of this work is to understand the atomic arrangements, the electronic properties, and the vibrational properties of crystalline and amorphous $GeSe_2$ and further to explore the light-induced crystallization process in $GeSe_2$.

The light-induced crystallization process in this material proceeds within the time period of several ten minutes which is an appropriate time-scale for the detailed observation of the process. In the light-induced crystallization, there are two key processes; 1) the interaction between the incident photon and the electrons in the material and 2) the change of the atomic arrangements in the material. For the understanding of the light-induced crystallization process, overall knowledge is important about the atomic arrangements and the electronic structures for both amorphous initial state and crystalline final state.

The satisfactory knowledge about the structure of amorphous $GeSe_2$ (a–$GeSe_2$) has not been obtained yet, while the structure of crystalline $GeSe_2$ (c–$GeSe_2$) has been well determined by the diffraction methods. One of the difficulties in the structural investigation of the glass is that the diffraction analysis brings less information about the materials without the long-range order. The analysis of vibrational modes observed in Raman scattering experiment becomes one of the effective methods to investigate the short- and medium-range structures in such disordered materials. The Raman spectra in a–$GeSe_2$ have been extensively studied up to the present.[10–18] The precise assignment of the Raman bands, however, has not been accomplished, though a resemblance of the spectra of a–$GeSe_2$ to those of c–$GeSe_2$ strongly suggests that a–$GeSe_2$ contains atomic structures which are topologically like the c–$GeSe_2$ structure. To obtain further knowledge about the a–$GeSe_2$ structure from the Raman spectra, the knowledge about the vibrational modes of c–$GeSe_2$ is indispensable. However, because of the complexity of the crystalline structure, the full analysis of the vibrational modes in c–$GeSe_2$ has not been achieved yet.

As for the electronic states, several optical measurement has been reported.[19–22] However, more detailed knowledge of near band-edge excitations will be necessary for the understanding of the photo-structural changes.

In this thesis, the vibrational and the electronic structures in crystalline and amorphous $GeSe_2$ are studied in detail by Raman scattering experiment with various excitation photon energies and by optical absorption experiment both at several

temperatures. From the experimental results, the atomic arrangement, the vibrational structure, and the electronic structure in crystalline and amorphous $GeSe_2$ are discussed. In the Raman spectra of single crystals, we have first observed resonance effects which connect electronic excitations (excitons) with lattice vibrations. The vibrational modes and the nature of the exciton are discussed. In the experiment on polycrystalline films, it has been found out that the characteristic excitation energy relating to the resonance effect is significantly lowered by disorder. The observation of the resonance plays an important role in the understanding of the relation among the Raman spectra of single-crystalline, polycrystalline, and amorphous $GeSe_2$, in which series the degree of disorder in samples is considered to be increasing. From the experiment on the single-crystal and polycrystal, we discuss the structure of amorphous $GeSe_2$. The coupling between electronic excitations and lattice vibrations are important also in the light-induced crystallization process. We try to distinguish the photo-process from thermal heating process by light irradiation using time-resolved Raman scattering measurement at various environmental temperatures. The difference between the light-induced crystallization and the thermal crystallization suggests that the medium-range structure in the amorphous state plays an important role in the light-induced crystallization.

The contents of this thesis are as follows. In Sec. 2, background knowledge about both crystalline and amorphous $GeSe_2$ obtained up to the present time are reviewed. Section 3 contains the details of the sample preparation, the Raman experiment, and the optical absorption measurement. Section 4 shows the results of the experiments and the procedures of the data analysis. In this section, the vibrational structure, the electronic structure, and the atomic arrangement of crystalline and amorphous $GeSe_2$, and the light-induced crystallization will be discussed. Section 5 is devoted to a summary of this thesis.

2 Review of $GeSe_2$

2.1 Crystalline $GeSe_2$

2.1.1 Atomic Arrangements

For crystalline $GeSe_2$, three polymorphic modifications have been reported, namely α–, β–, and γ–$GeSe_2$.[23] Among three polymorphs, β–$GeSe_2$ which is a yellow micaceous modification is most easily obtained by usual preparation methods like the Bridgman technique. Dittmer and Schäfer have determined the atomic arrangement of β–$GeSe_2$ by the X–ray diffraction analysis.[24] The crystallographic data of β–$GeSe_2$ are shown in Table 1. Figures 1 (a) and (b) show the projection of the atomic arrangement of one mono-layer of β–$GeSe_2$ onto the (001)–plane and the view along the [100]–direction. The Ge and Se atoms within a layer are covalently bonded to each other, while the neighboring layers are bound by weak van der Waals coupling. A basic building-block in β–$GeSe_2$ is a $GeSe_{4/2}$ tetrahedron in which four selenium atoms are located at its corners and one germanium atom at its center as shown in Fig. 1. Each Se atom is shared by two neighboring tetrahedra. In the structure, there are corner-sharing $GeSe_{4/2}$ tetrahedra (A, in the figure) that compose chains along the a axis and edge-sharing $Ge_2Se_{8/2}$ bi-tetrahedra (B) that connect chains mutually like bridges.

In GeS_2, two polymorphic modifications have been known, namely α– and β–GeS_2 which are the low temperature phase and the high temperature phase, respectively. The crystallographic data for these two modifications obtained by Dittmer and Schäfer are shown in Table 2.[25,26] The α–GeS_2 crystal consists of a three dimensional network of corner-sharing $GeS_{4/2}$ tetrahedra, while β–GeS_2, which is isotypic with β–$GeSe_2$, has the two dimensional micaceous structure. The atomic arrangement of α–GeS_2 is shown in Figs. 2 and 3. As for $GeSe_2$, it is difficult to obtain bulk single crystals of the α phase. However, it has been reported that a crystalline phase different from the β phase is grown in the a-$GeSe_2$ film annealed at about 375 °C

Table 1: Crystallographic data for β–$GeSe_2$. V: Volume of a unit cell; Z: Number of $GeSe_2$ molecules in a unit cell; M: Molecular weight; D_x: Calculated density; D_m: Measured density.

β–$GeSe_2$	
Crystal structure: monoclinic	
Space group: $P_{2_1/c}$	
Parameters:	
$V = 1394.0$ Å^3	$Z = 16$
$a = 7.016(3)$ Å	$M = 230.52$ g/mol
$b = 16.796(8)$ Å	$D_x = 4.39$ g/cm^3
$c = 11.831(5)$ Å	$D_m = 4.37$ g/cm^3
$\beta = 90.65(5)°$	

From Ref. 24.

[27] or is obtained as small crystals by subliming $GeSe_2$ in a current of Ar gas.[28] The crystalline phase in those reports is considered to have the three dimensional structure like α–GeS_2 (See Sec. 2.1.2).

There is still another polymorphic form named γ–$GeSe_2$.[29] Although the crystal structure and the lattice parameters have not been known, the differential thermal analysis (DTA) shows that the melting point of γ–$GeSe_2$ is 850 °C which is much higher than those of α– and β–$GeSe_2$ (740 ± 5 and 743 ± 5 °C, respectively).[29] There has been reports on the Raman spectra[29] and the reflection spectra[30] of γ–$GeSe_2$.

2.1.2 Raman Spectra

There are 48 atoms in a unit cell of β–$GeSe_2$ crystal, which make 144 phonon branches in the Brillouin zone. The symmetries of the normal modes at the Γ point lead $36A_g$ Raman active modes, $36B_g$ Raman active modes, $35A_u$ infrared active modes, $34B_u$ infrared active modes and 3 translational modes.[23]

Table 2: Crystallographic data for α– and β–GeS_2. V: Volume of a unit cell; Z: Number of GeS_2 molecules in a unit cell; M: Molecular weight; D_x: Calculated density; D_m: Measured density.

α–GeS_2	
Crystal structure: monoclinic	
Space group: P_c	
Lattice parameters:	
$V = 910.01$ Å^3	$Z = 12$
$a = 6.875(5)$ Å	
$b = 22.55(1)$ Å	$D_x = 2.99$ g/cm^3
$c = 6.809(5)$ Å	$D_m = 3.01$ g/cm^3
$\beta = 120.45(5)°$	
β–GeS_2	
Crystal structure: monoclinic	
Space group: $P_{2_1/c}$	
Lattice parameters:	
$V = 1237.2$ Å^3	$Z = 16$
$a = 6.720(3)$ Å	$M = 136.732$ g/mol
$b = 16.101(3)$ Å	$D_x = 2.935$ g/cm^3
$c = 11.436(3)$ Å	$D_m = 2.89$ g/cm^3
$\beta = 90.88(5)°$	

From Refs. 25 and 26.

Popović and Stolz have reported the polarized Raman spectra of β–$GeSe_2$ at 300 K and 4.2 K using 5145 Å (2.41 eV) and 5017 Å (2.47 eV) lines of an argon ion laser as the excitation light and have found 69 Raman lines.[23] Figure 4 shows their spectra in which the most strong band is located around 212 cm^{-1}.

The band around 212 cm^{-1} is assigned to a breathing motion of the $GeSe_{4/2}$ tetrahedra. This assignment is justified as follows: 1) The vibrational energy of the breathing motion in $GeBr_4$ tetrahedral gas molecule is around 234 cm^{-1} which is very close to 212 cm^{-1}.[14] 2) Assuming the bond polarizability model for the Raman scattering intensity,[31] the breathing motion of the tetrahedra which implies the stretching motion of Ge–Se bonds is expected to lead the most intense Raman band, because the stretching motion of the bonds causes large deviations of their bond polarizabilities from their equilibrium values. Bridenbaugh et al. have pointed out that the 212 cm^{-1} band is resolved into two modes: a strong mode at 210.3 cm^{-1} due to the breathing motion of the corner-sharing chain $GeSe_{4/2}$ tetrahedra and a weak mode at 215.3 cm^{-1} due to the breathing motion of the edge-sharing bridge $Ge_2Se_{8/2}$ bi-tetrahedra.[12] These assignments on the Raman bands around 212 cm^{-1} are supported by a recent vibrational calculation by Inoue et al..[32,33]

There are small discrepancies about the energy of each Raman band among the literatures. Hereafter, in this thesis, the modes that Bridenbaugh et al. observed at 210.3 and 215.3 cm^{-1} will be referred as the 211 and the 216 cm^{-1} bands, respectively.

Generally, a vibration of weak bonds like van der Waals bonds has a lower frequency than that of strong bonds like covalent bonds. The lowest band around 17 cm^{-1} is supposed to be due to the inter-layer vibration. Assignments on other Raman bands have not been accomplished well, because the crystalline structure is very complicated.

Raman measurement has not been made on single crystalline α–$GeSe_2$. Inoue et al. have measured the Raman spectra of the polycrystalline $GeSe_2$ films; the amorphous $GeSe_2$ films on glass substrates were annealed at various temperatures to

obtain the polycrystalline films.[27] Figure 5 shows the spectra of the films annealed at (c) 325 °C, (a) 375 °C, and (b) 425 °C in Ar gas for 18 hours. The spectrum (c) is almost the same as the spectra of as-deposited amorphous films and the spectrum (b) corresponds to the spectra of β–$GeSe_2$. In the spectrum (a), there are two new Raman peaks (E and F) at about 200 cm^{-1} and 90 cm^{-1} which are not observed in the spectra of β–$GeSe_2$. In order to explain the Raman bands E and F of crystalline $GeSe_2$, the spectra of GeS_2 have been investigated. In Fig. 6, the spectra of amorphous GeS_2, α–GeS_2, and β–GeS_2 are shown. There is strong similarity between the Raman bands A–D in the spectra of β–$GeSe_2$ and β–GeS_2 except for their energies. One will notice that there is a similar correspondence between the Raman bands E–F in the spectra of Fig. 5 (a) and Fig. 6 (a) (α–GeS_2). The result strongly suggests that there is a new crystalline phase in the polycrystalline film annealed at 375 °C and that the new phase has the similar atomic arrangement to α–GeS_2. Thus the new phase is considered to be α–$GeSe_2$. It should be noted that the annealing temperature for obtaining α–$GeSe_2$ is lower than that for obtaining β–$GeSe_2$, which corresponds to the fact that $\alpha(\beta)$–GeS_2 is the low (high) temperature crystalline phase. The 200 cm^{-1} band of α–$GeSe_2$ is considered to be due to the breathing motion of the $GeSe_{4/2}$ tetrahedra.

2.1.3 Optical Properties and Electronic Structure

Single crystalline β–$GeSe_2$ has strongly anisotropic optical properties. Almost all optical measurement on β–$GeSe_2$ has been done using a (001) surface of the crystal, because it is easy to get the (001) surface by cleaving the crystal, but obtaining other surfaces is much more difficult. Boiko et al. have measured the transmittance of the visible light propagating normal to the (001) surface of single crystalline β–$GeSe_2$.[22] Figure 7 shows the absorption spectra at 4.2 K. In the spectrum of the polarization parallel to the a axis ($\boldsymbol{E} \parallel \boldsymbol{a}$, curve 1 in the figure), they found an exciton absorption peak at 2.854 eV which is not observed in the $\boldsymbol{E} \parallel \boldsymbol{b}$ spectrum (curve 2). Although the absolute values of the absorption coefficients are not shown

Table 3: Energy gap values of β–$GeSe_2$.

T (K)	E_g (eV)	
	$\boldsymbol{E} \parallel \boldsymbol{a}$	$\boldsymbol{E} \parallel \boldsymbol{b}$
300	2.50	2.49
77	2.675	2.685
4.2	2.725	2.735

From Ref. 20.

in the figure, the maximum of the exciton peak is $\alpha \sim 10^4$ cm^{-1}. The exciton absorption peak energy decreases with increasing sample temperature as shown in Fig. 8. The exciton transition energy is about 2.7 eV at room temperature. The temperature dependence of energy gap values derived from the plot of α^2 versus $h\nu$ by Popović and Breitschwerdt is shown in Table 3.

The dielectric functions ϵ_1 and ϵ_2 of β–$GeSe_2$ for $\boldsymbol{E} \parallel \boldsymbol{a}$ and $\boldsymbol{E} \parallel \boldsymbol{b}$ have been investigated by Aspnes et al. and by Inoue et al..[19,21] The dielectric function spectra at room temperature by Inoue et al. are shown in Fig. 9. There are two small humps at about 2.7 eV and about 2.9 eV in ϵ_2 of $\boldsymbol{E} \parallel \boldsymbol{a}$. The former corresponds to the exciton absorption at 2.7 eV. The more gross shape of the low energy region of the ϵ_2 spectra are characterized by two bands: one is located around 3 eV and the other is around 5 eV.

Inoue et al. have reported the valence-band photo-emission spectrum of β–$GeSe_2$ excited by 70 eV light as shown in Fig. 10 (a).[21] In the spectra, five valence bands (a_1, a_2, a_3, b, c) appear. For the conduction bands, they introduced two critical points (s^*, p^*) from the core-exciton excitation spectra. Finally, combining the photo-emission spectra, the core-exciton excitation spectra, and the reflectance spectra by the synchrotron radiation (SR), they concluded that the a_1 band consists of two bands, a_1 and a_1'. Therefore, there are six valence bands and two critical points in

the conduction band. Figure 11 shows a schematic energy diagram for the valence and conduction bands.[34] Ordering the energy levels in the valence band after the manner of decreasing energy, the highest two levels a_1 and a_1' come from the Se $4p$ lone-pair electrons, the next two levels a_2 and a_3 from the Ge–Se bonding electrons, the next b from the Ge s–like bonding electrons, and the lowest c from the Se $4s$ electrons. The conduction bands are due to the Ge–Se anti-bonding electrons. These assignments are also supported by the calculation on the electronic band structure by Louie.[35] Energy levels of these bands are listed in Table 4. The ϵ_2 spectra around 3 eV are explained as the transitions of $a_1 \rightarrow s^*$ and $a_1' \rightarrow s^*$ and the spectra around 5 eV are explained as those of $a_1 \rightarrow p^*$ and $a_1' \rightarrow p^*$.

Table 4: Energy levels (in eV) referred to the valence band maximum (VBM) of β–$GeSe_2$ and a–$GeSe_2$. p^* and s^*: critical points in the conduction band; CBM: the conduction band minimum; a_1 and a_1': Se lone-pair electrons; a_2 and a_3: Ge–Se bonding electrons; b: Ge 4s–like electrons; c: Se 4s electrons.

Levels	β–$GeSe_2$	a–$GeSe_2$
p^*	3.9	3.8
s^*	2.8	2.5
CBM (Eg)	2.6	2.2
Fermi level	1.8	1.4
VBM	0	0
a_1'	-0.6	-0.8
a_1	-1.3	-1.4
a_2	-3.2	-3.5
a_3	-4.9	-5.2
b	-7.9	-8.1
c	-13.0	-13.3
Ge 3d $(\frac{5}{2})$	-29.6	-29.6
Ge 3d $(\frac{3}{2})$	-30.2	-30.2
Se 3d $(\frac{5}{2})$	-53.1	-53.1
Se 3d $(\frac{3}{2})$	-54.0	-54.0

From Ref. 21.

2.2 Amorphous $GeSe_2$

2.2.1 Diffractional Analysis

Although the diffraction technique is the most powerful method to investigate an atomic arrangement in a periodic lattice, it can not uniquely determine the atomic arrangement in an amorphous material where the long-range order is completely destroyed. However, even for amorphous materials, there are important informations in the neutron and X–ray scattering experiments.

The neutron diffraction of a–$GeSe_2$ has been studied by Uemura et al..[36] The total radial distribution function shows that the first and the second nearest neighbor distances are 2.365 Å and 3.86 Å, respectively, and that the average coordination number of the first nearest neighbor is 2.62. A possible structure is that each Ge atom is fourfold and each Se atom twofold coordinated which gives the average coordination number $4\times\frac{1}{3}+2\times\frac{2}{3} = 2.66$. In the case of β–$GeSe_2$, the atomic distance between a Ge atom and a Se atom belonging to the same $GeSe_{4/2}$ tetrahedron is $2.3 \sim 2.4$ Å and that between two Se atoms belonging to the same tetrahedron is $3.8 \sim 4.0$ Å. Recently the differential anomalous X–Ray scattering technique using the SR light has given the partial structure factors which show that the first-neighbor coordination numbers are 3.8 atoms for Ge and 2.3 atoms for Se.[37] An EXAFS study by Sayers et al. also has shown that the average numbers of Ge atoms around Ge and Se are 0.1 and 1.9, respectively, whereas the number of Se atoms around Ge and Se are 3.8 and 0.2, respectively.[38] From these results, the short range structure of a–$GeSe_2$ can be described as follows: 1) most of atoms are forming the $GeSe_{4/2}$ tetrahedra similar to atoms in crystalline $GeSe_2$; 2) the $GeSe_{4/2}$ tetrahedra are connected at their corners; 3) there are appreciable amount of Se–Se and Ge–Ge bonds due to partially-broken chemical order called as wrong bonds, which are also evidenced by characteristic Raman bands (See Sec. 2.2.2).

Another interesting problem in the diffraction studies is an existence of the first sharp diffraction peak (FSDP) in the structure factor $S(k)$. Figure 12 shows $S(k)$

of neutron scattering in a–$GeSe_2$.[39] The FSDP appears at 1.01 $Å^{-1}$ corresponding to a correlation length of about $2\pi/k = 6.22$ Å which suggests that there is some medium-range order (MRO). The FSDP shows anomalous thermal behaviors as follows: 1) the peak height increases with increasing temperature; 2) It still remains as a sharp peak in the structure factor of liquid $GeSe_2$.

Vashishta et al. have made extensive molecular dynamics (MD) studies of the structure and dynamics of glassy and liquid $GeSe_2$, using three body potentials.[40] They followed the motion of the atoms from the melt to the glass by quenching. The calculated structure factors in glassy and molten $GeSe_2$ agree well with the experimental result. The most important benefit of the MD calculation is the capabilities of directly obtaining various statistics which are hardly obtained by experiments. Figure 13 shows the calculated partial structure factor in a–$GeSe_2$ at 300 K. The FSDP comes mainly from the Ge–Ge correlation and partially from the Ge–Se correlation. The calculation of $S(k)$ with the distribution function $\rho(x)$ which is constant beyond $x_c = 4$ Å provides no FSDP. The FSDP grows with increasing x_c to 8 Å, and becomes constant with $x_c > 8$ Å. Thus the intermediate-range correlations between 4 and 8 Å are responsible for the FSDP. The calculated FSDP decreases with increasing glass density at a fixed temperature, which was explained as that the increasing in the density enhances the frustration associated with the packing of $GeSe_{4/2}$ tetrahedra. The decrease in the height of the FSDP with decreasing temperature was ascribed to the fact that larger density at low temperature offsets the increase of the FSDP resulting from cooling alone. The result of this MD calcuration will be re-examined in Sec. 4.3.2.

2.2.2 Raman Spectra

Raman scattering measurement is one of the most powerful method to investigate the short- and medium-range structures in amorphous solids, because the vibrational properties are closely related to the manner of the atomic connections.

Figure 14 shows the Raman spectra of a–$GeSe_2$ at 60 K excited by 6328 Å (1.96

eV) light of a He–Ne laser.[41] There are three prominent bands in the (HH) spectra, namely the A_1 band at about 203 cm^{-1}, the A_1 companion (A_1^C) band at about 219 cm^{-1}, and the A_G band at about 180 cm^{-1}. These lines were observed around 198 cm^{-1}, 216 cm^{-1}, and 178 cm^{-1} at 300 K.[42] The fact that there are intense bands around 200 cm^{-1} all for amorphous, α–, and β–$GeSe_2$ suggests that the structure of a–$GeSe_2$ roughly resembles those of both crystalline phases.[14] Then a basic structural unit in a–$GeSe_2$ has been considered to be a $GeSe_{4/2}$ tetrahedron as well as in both crystals. This structural model agrees with the result of the diffraction analysis where the Ge atom is fourfold coordinated and the Se atom twofold coordinated. The number of dangling bonds in a–$GeSe_2$ is supposed to be negligible, because ESR investigations carried out in different chalcogenide glasses (As_2Se_3, As_2S_3) lead to the result that the number of defects with spins is negligible.[43,44] The model should make almost all valencies be satisfied.

To understand the origin of three bands, A_1, A_1^C, and A_G, the composition dependence of Raman spectra of Ge_xSe_{1-x} bulk glass, which is available in the range of $0 \leq x \leq 0.42$, have been investigated.[10,14,17,45] As shown in Fig. 15,[45] the A_1 band appears in all spectra except for $x = 0$ which is pure amorphous Se. The A_1 band has been ascribed to the breathing motion of $GeSe_{4/2}$ tetrahedra. This assignment is supported by the argument similar to that on the breathing motion of $GeSe_{4/2}$ tetrahedra in β–$GeSe_2$ (See Sec. 2.1.2).

The Raman scattered light due to the symmetric breathing motion of XY_4 tetrahedral molecule in gaseous phase is polarized parallel to the polarization of the excitation light. According to the short range structure described above, the bond angle of Ge–Se–Ge is nearly 90° which makes it possible roughly to say that each $GeSe_{4/2}$ tetrahedra in a–$GeSe_2$ vibrates quasi-independently. This molecular-like treatment of the vibration of the $GeSe_{4/2}$ tetrahedra predicts that the Raman signal from the breathing motion of the tetrahedra has small de-polarization ratio I_{VH}/I_{VV}, which is the case for the A_1 and A_1^C bands. Thus the A_1^C band seems to be also related to the breathing motion of the $GeSe_{4/2}$ tetrahedra.

As shown in Fig. 15, the growth of the A_1 band with increasing x up to $x = 1/3$ is accompanied by the consumption of the band around 250 cm^{-1} which is due to the Se–Se stretching motion. This observation indicates that the density of the $GeSe_{4/2}$ tetrahedra increases with the consumption of the Se–Se bonds. For $x \geq 1/3$ where the formation of the Ge–Ge bonds is unavoidable, the A_G band appears and grows with increasing x. The A_G band has been assigned to the Ge–Ge bonds. The absence of the A_G band in $x < 1/3$ indicates that the Ge–Ge bonds are not favorable and that the Ge atoms are likely to be connected to the Se atoms.

The behavior of the A_1^C band is somewhat mysterious; 1) there are two intense bands (A_1 and A_1^C) in the spectra of amorphous $GeSe_2$, while there is one intense band (the 211 cm^{-1} band) due to the breathing motion of the $GeSe_{4/2}$ tetrahedra in the spectra of crystalline $GeSe_2$. 2) The width of the A_1^C band (10.4 cm^{-1} FWHM at RT) is narrower than that of the A_1 band (19.1 cm^{-1} FWHM at RT). 3) Assuming that the intensity of the A_1 band increases in proportion to x, that of the A_1^C band increases slowly in small x region and then rapidly as x approaches to 1/3. In the region of $x > 1/3$, the A_1^C band gradually decreases up to $x = 0.42$.[11] The non-linear behavior of the A_1^C intensity with respect to x indicates that the A_1^C band is assigned to the vibration of the structures composed of several $GeSe_{4/2}$ tetrahedral units (cluster or medium-range structure). Nemanich et al. have studied $(As_2Se_3)_x(GeSe_2)_{1-x}$ glass and have observed that the A_1^C band decreases with increasing x as shown in Fig. 16.[17] A basic building-block in amorphous As_2Se_3 is an $AsSe_{3/2}$ unit. With increasing x, the $AsSe_{3/2}$ blocks become to break clusters of $GeSe_{4/2}$ tetrahedra which are responsible for the A_1^C band. The existence of the cluster has been also suggested by the observation of a broad band in the Raman spectra of a–$GeSe_2$ at the low energy region around several 10 cm^{-1} (Bose peak).[46] The fact that the vibration energy is low might mean that there is the cluster with a large mass which moves collectively and that the restoring force between the clusters is weak.

The actual structure of the cluster of $GeSe_{4/2}$ tetrahedra has not been clearly

understood yet. The investigation of the cluster-structure is one of main subjects of this thesis. The structural models which have been proposed to explain the origin of the A_1^C band up to the present will be discussed together with our result in Sec. 4.3.2.

2.2.3 Optical Properties and Electronic Structure

Figure 17 shows the absorption spectra of the Ge_xSe_{1-x} glasses reported by Tronc et al..[10] The absorption coefficients of a–$GeSe_2$ around 2 eV are considerably higher than those of β–$GeSe_2$. For both compositions x higher and lower than the stoichiometry, $x = 1/3$, the optical absorption edge moves to the lower energy side than that of a–$GeSe_2$. The increase in the density of the wrong bonds Ge–Ge and Se–Se is supposed to be responsible for the increase of the absorption coefficients for $x \neq 1/3$ glasses.

The dielectric functions of a–$GeSe_2$ have been investigated by Aspnes et al.[19] and Inoue et al..[21] The functions shown in Fig. 18 resemble those of β–$GeSe_2$, though there are tail states within the region where β–$GeSe_2$ is transparent and the fine structures around absorption tail, which are observed in the crystalline spectra, are smeared out. The photo-emission and reflectance studies of a–$GeSe_2$ show that there are six characteristic bands in the valence band and two bands in the conduction band similarly to β–$GeSe_2$ (Fig. 10 at page 25). These results suggest that the structure of a–$GeSe_2$ very much resembles that of β–$GeSe_2$ and that the conclusion on the electronic structure described in Sec. 2.1.3 can also be applied to a–$GeSe_2$. In Table 4 (Page 11), the energy levels of a–$GeSe_2$ are shown.[21]

2.3 Photo-Induced Structural Change

When the glassy $GeSe_2$ is irradiated, the photo-bleaching occurs.[3] Griffiths et al. have discovered that the irradiation of the sub-band-gap light (1.92 eV) on the $GeSe_2$ bulk glass at 77 K causes the crystallization of the glass.[4] The investigation has been developed by several workers.[27,42,47–49] Murase et al. have investigated the

crystallization process which is induced by the irradiation of the 5145 Å (2.41 eV) light of an Ar ion laser onto the amorphous $GeSe_2$ film at RT. The excitation light whose power was $10 \sim 40$ mW was focused to region of $30 \sim 50$ μm diameter on the sample surface. A time-resolved Raman measurement technique was utilized to get sets of Raman spectra which are successively measured in every one minute during the laser irradiation.[42] The excitation light for the crystallization is also used as the probe light for the Raman measurement. Two representative sets of spectra are shown in Fig. 19. One is referred to as the type A where only β–$GeSe_2$ grows, and the other is as the type B where both α–$GeSe_2$ and β–$GeSe_2$ grow.

Figure 20 shows one of the time evolution of the peak height $I(t)$ of the crystalline 211 cm^{-1} band (β–$GeSe_2$) in the type A light-induced crystallization.[27] There is a latent period t_0 (incubation period) where no crystallization is observed and after that the crystalline peak begins to grow. The growth curve $I(t)$ is fitted by an empirical function:

$$I(t) = \begin{cases} I_{sat}\{1 - \exp(-k(t-t_0)^n)\} + I_0, & \text{for } t > t_0, \\ I_0, & \text{otherwise,} \end{cases}$$

where I_{sat} is the saturation intensity at large t, I_0 is the initial intensity due to the amorphous band, and k is the growth rate. The best fit is given by $n = 1$.

The latent period t_0 depends on the excitation laser power. As shown in Fig. 21, there is a threshold power near 14 mW over which the crystallization occurs and near the threshold the latent period becomes divergently long.

The type A crystallization is more frequently observed than the type B. It seems that there is no distinction between the excitation powers or other external conditions for the appearance of each type of the crystallization, A and B.

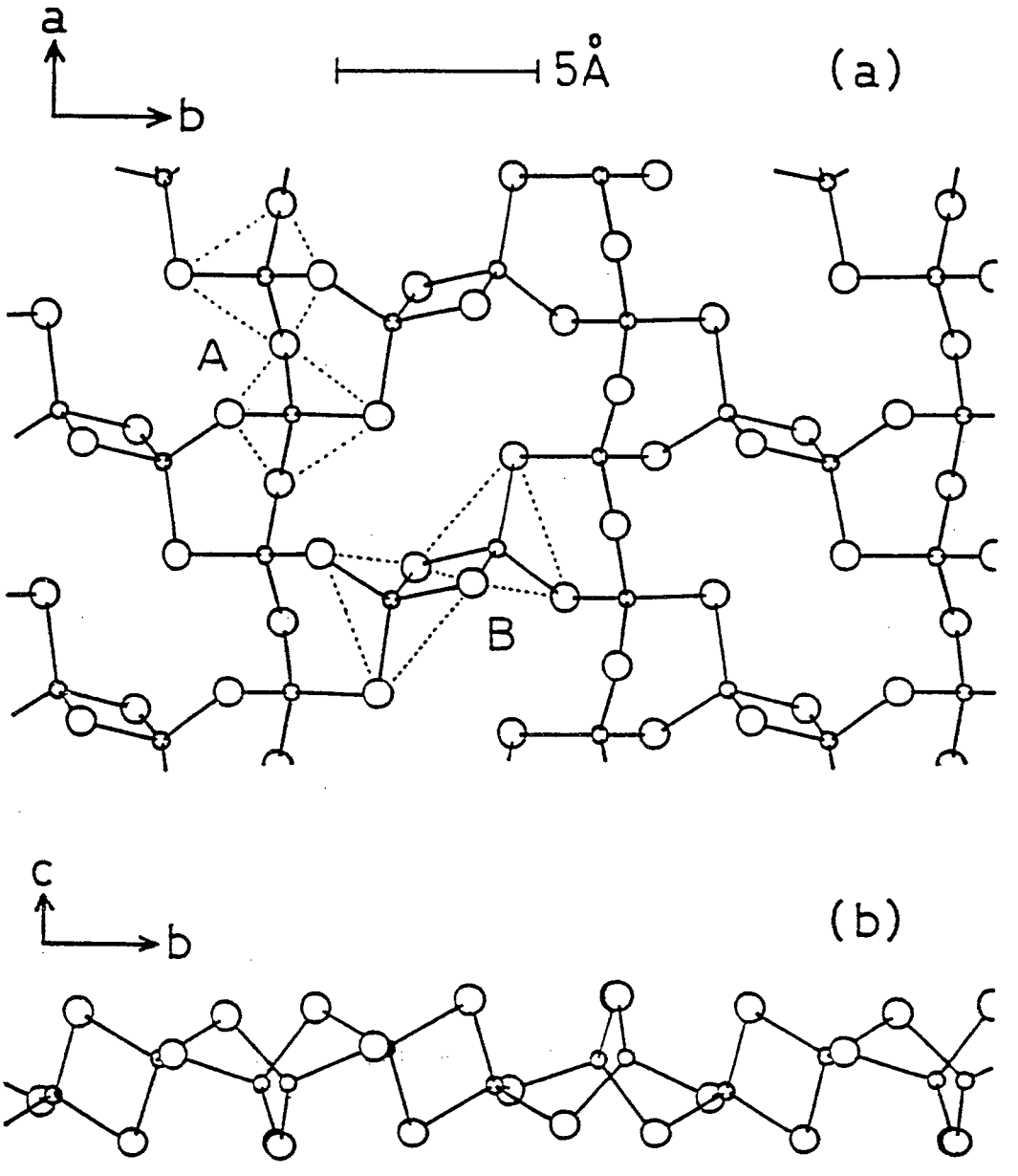

Figure 1: Atomic arrangement of one mono-layer of β–$GeSe_2$. (a) Projection onto the (001)–plane and (b) view along the [100]–direction. Smaller circles denote Ge atoms, and larger ones Se atoms. Broken lines display $GeSe_{4/2}$ tetrahedra; A: corner sharing chain tetrahedra, B: edge-sharing bridge bi-tetrahedra.

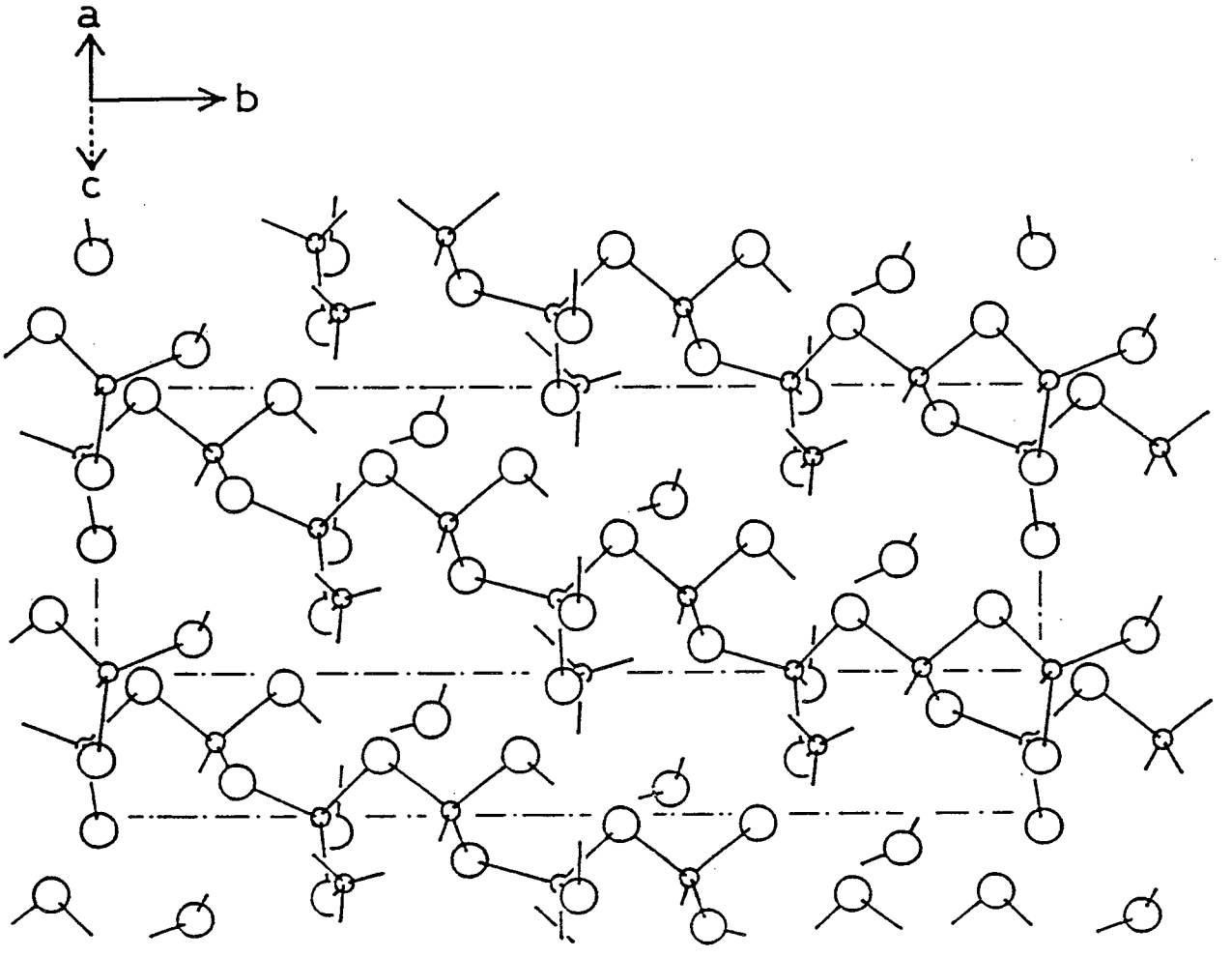

Figure 2: Projection of atomic arrangement of α–GeS_2 onto the (001)–plane. Smaller circles denote Ge atoms, and larger ones S atoms. All $GeS_{4/2}$ tetrahedra are connected mutually by their corners. The c axis is at an angle of 120.45° to the a axis and is directed toward the back of the figure. Dashed-and-dotted line shows the projection of the wire frame of the unit cell.

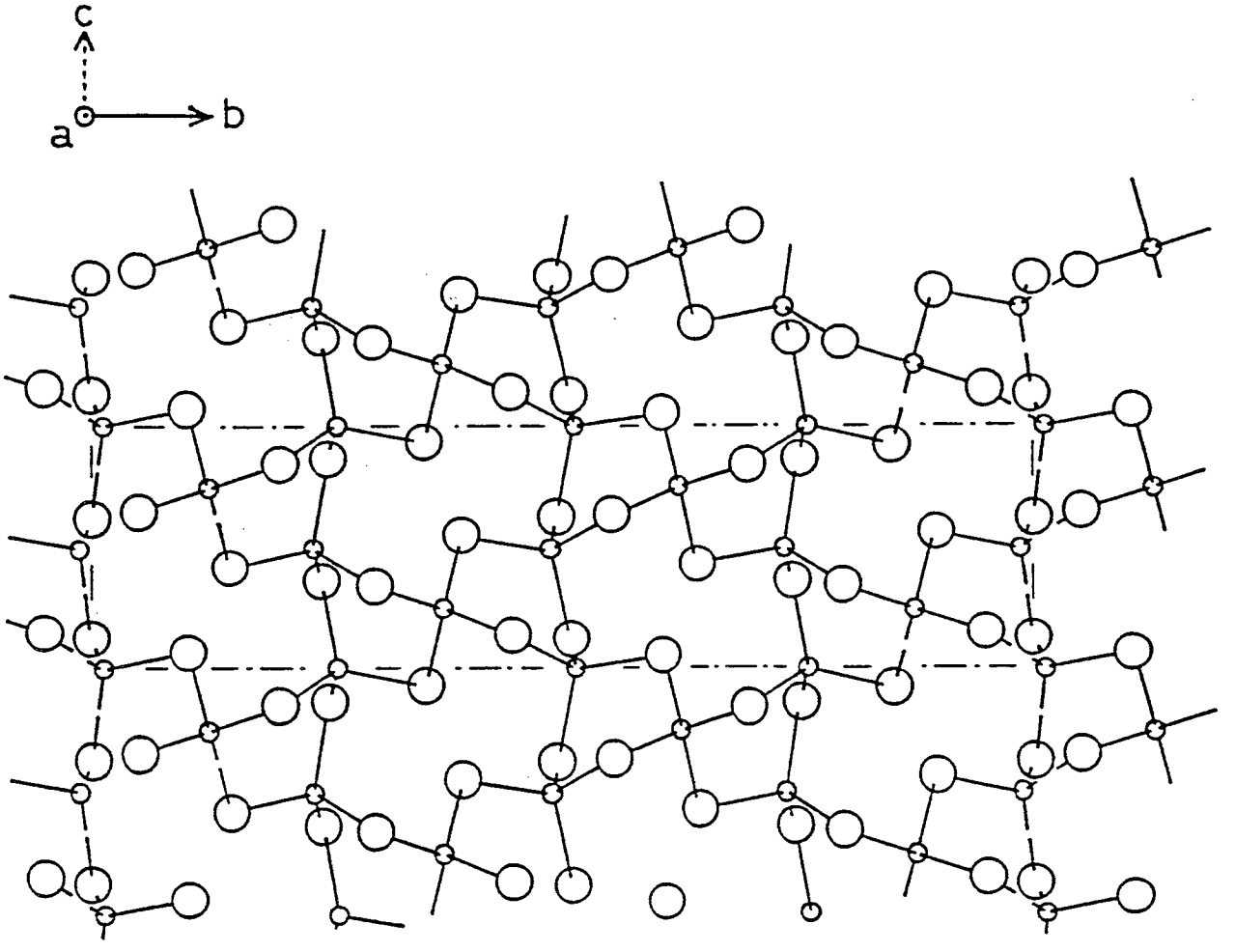

Figure 3: View of atomic arrangement of α–GeS_2 along the [100]–direction. Smaller circles denote Ge atoms, and larger ones S atoms. All $GeS_{4/2}$ tetrahedra are connected mutually by their corners. The a axis is perpendicular to the plane of the figure and is directed toward the front of the figure. The c axis is at an angle of 120.45° to the a axis and is directed toward the back of the figure. Dashed-and-dotted line shows the projection of the wire frame of the unit cell.

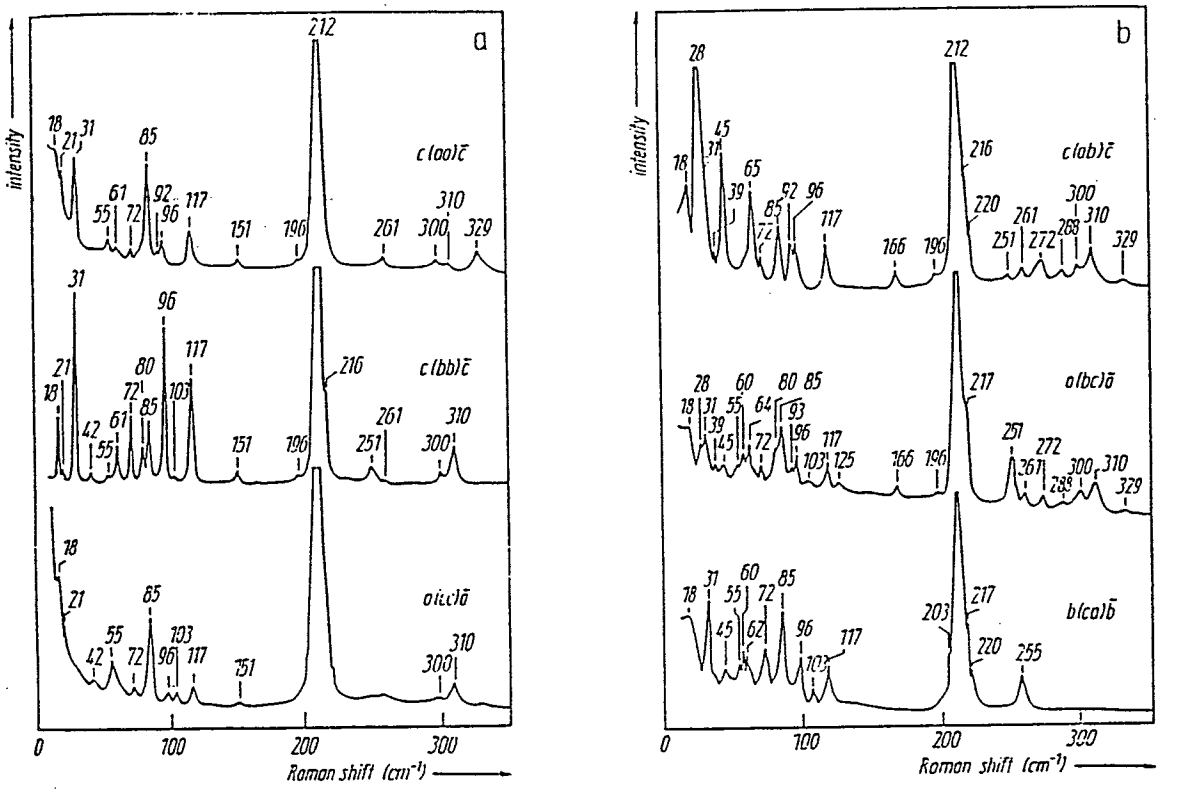

Figure 4: Polarized Raman spectra of β–$GeSe_2$ at room temperature. Excitation photon energy is 2.41 eV (5145 Å). The most intense band around 212 cm^{-1} is due to the breathing motion of $GeSe_{4/2}$ tetrahedra (From Ref. 23).

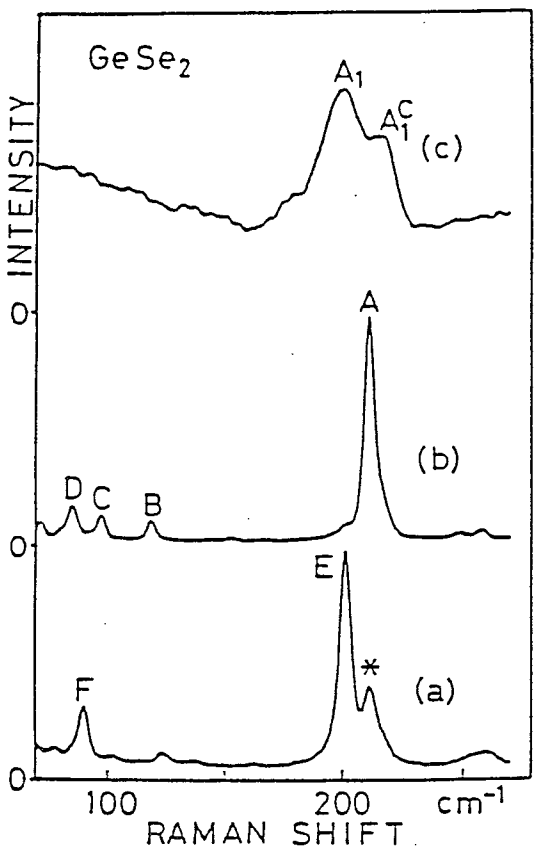

Figure 5: Raman spectra of annealed amorphous $GeSe_2$ films measured at room temperature. The excitation photon energy was 2.41 eV (5145 Å). The annealing temperatures were (a) 375 °C, (b) 425 °C, and (c) 325 °C. The spectrum (c) is almost the same with those of as-deposited amorphous films and the spectrum (b) corresponds to those of β–$GeSe_2$. It is considered that the spectrum (a) is of α–$GeSe_2$. The line $*$ is due to the contamination with β–$GeSe_2$ (From Ref. 27).

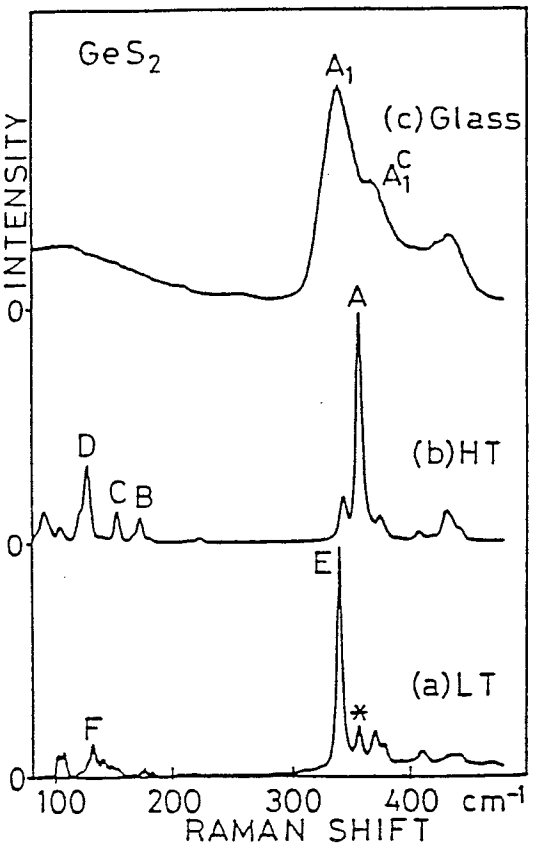

Figure 6: Room temperature Raman spectra of (a) α–, (b) β–, and (c) amorphous GeS_2. The line $*$ is due to the contamination with β–GeS_2. The lines A through F correspond to the lines A through F in Fig. 5 (From Ref. 27).

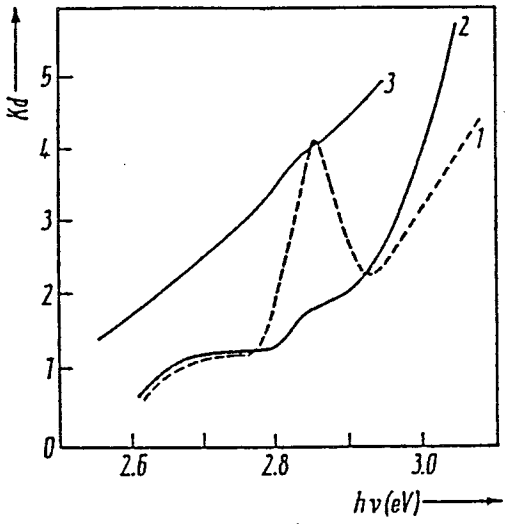

Figure 7: Absorption spectra of (1) β–$GeSe_2$ in $\boldsymbol{E} \parallel \boldsymbol{a}$ polarization, (2) β–$GeSe_2$ in $\boldsymbol{E} \parallel \boldsymbol{b}$ polarization, and (3) amorphous $GeSe_2$ at 4.2 K. In the $\boldsymbol{E} \parallel \boldsymbol{a}$ polarization, an exciton absorption peak is observed at about 2.854 eV (From Ref. 22).

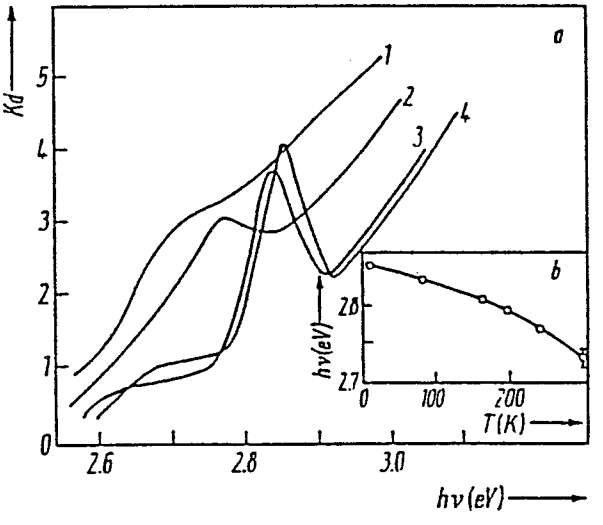

Figure 8: Absorption spectra of β–$GeSe_2$ in the $\boldsymbol{E} \parallel \boldsymbol{a}$ polarization, at (1) 300 K, (2) 240 K, (3) 77 K, and (4) 4.2 K. The inset shows temperature dependence of the exciton transition energy. The exciton absorption peak becomes sharp and moves toward the higher energy side with decreasing temperature (From Ref. 22).

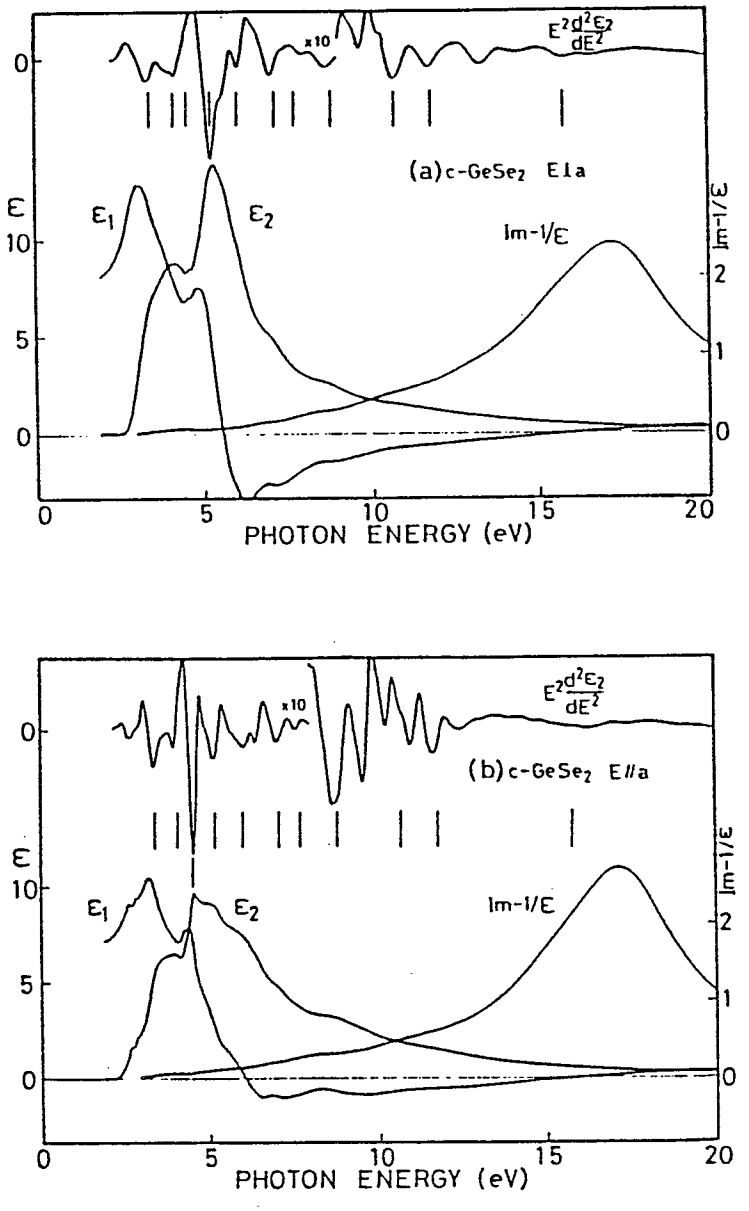

Figure 9: Dielectric functions of β–$GeSe_2$ at room temperature: (a) $\boldsymbol{E} \parallel \boldsymbol{b}$ polarization and (b) $\boldsymbol{E} \parallel \boldsymbol{a}$ polarization. The overall shape of ϵ_2 spectra consists of two peaks around 3 eV and 5 eV. The vertical bars are calculated transition energies from the characteristic energy levels in Table 4. The detail of the assignment is described in Ref. 21 (From Ref. 21).

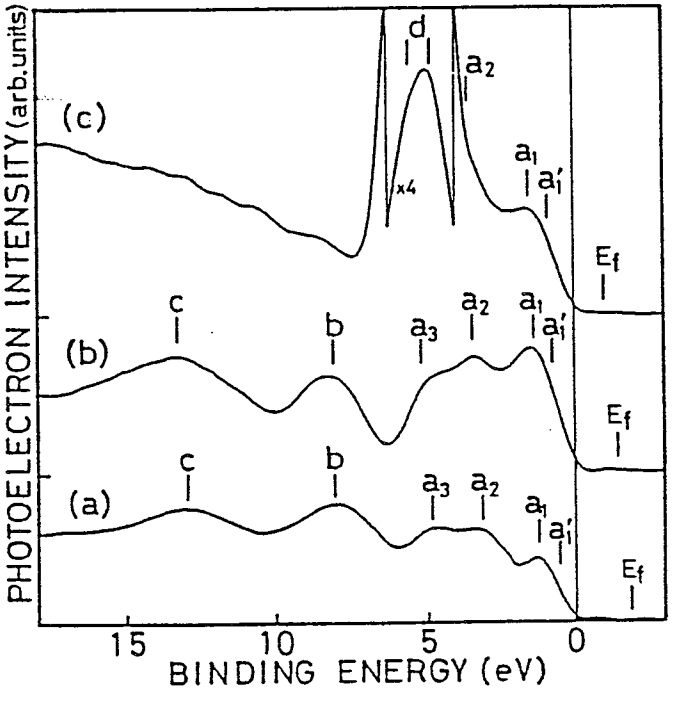

Figure 10: Valence band photo-emission spectra of (a) β–, (b) a–$GeSe_2$ and (c) a–$GeSe_2$:$Ag_{0.5}$. Binding energy is taken from the valence band maximum. E_f: Fermi energy; a_1 and a_1': Se lone-pair electrons; a_2 and a_3: Ge–Se bonding electrons; b: Ge s-like bonding electrons; c: Se $4s$ electrons. The detail of the spectrum (c) is described in Ref. 21 (From Ref. 21).

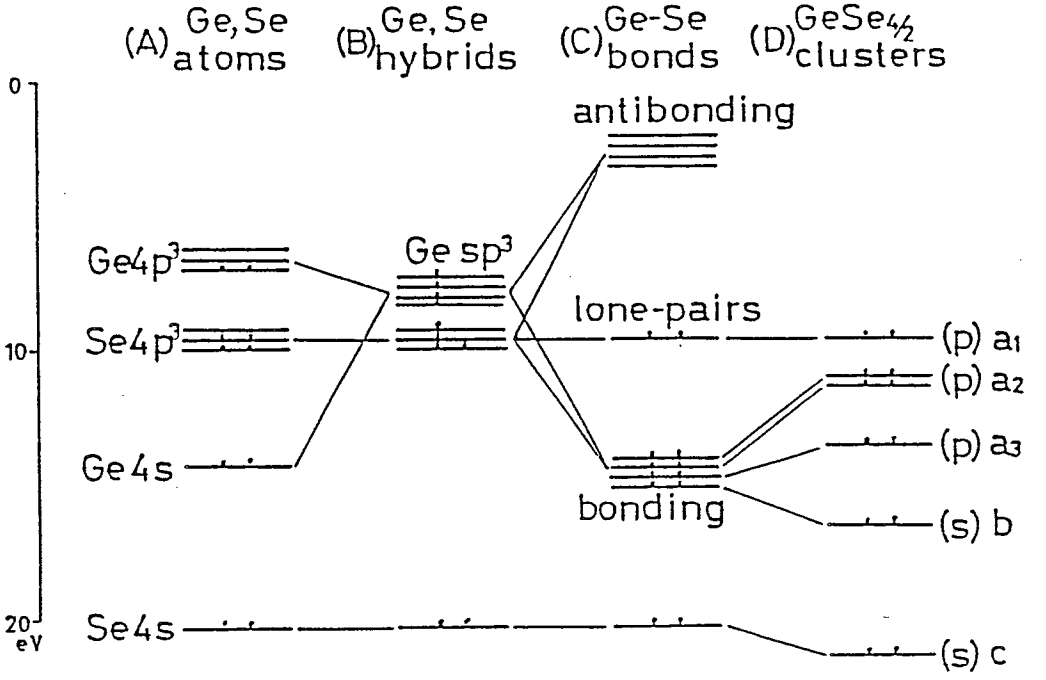

Figure 11: Schematic energy diagram in $GeSe_2$. (A) Energy levels of valence electrons for separated Ge and Se atoms. (B) Three Ge $4p$ and one Ge $4s$ orbitals hybridize to a sp^3 orbital. (C) A Ge sp^3 hybrid and one of Se $4p$ orbitals make Ge–Se bonding and anti-bonding states. There remains two Se $4p$ orbitals as lone-pair electrons. (D) Clustering of $GeSe_{4/2}$ tetrahedra resolves the degeneracy of four Ge–Se bonding orbitals at a Ge site (From Ref. 34).

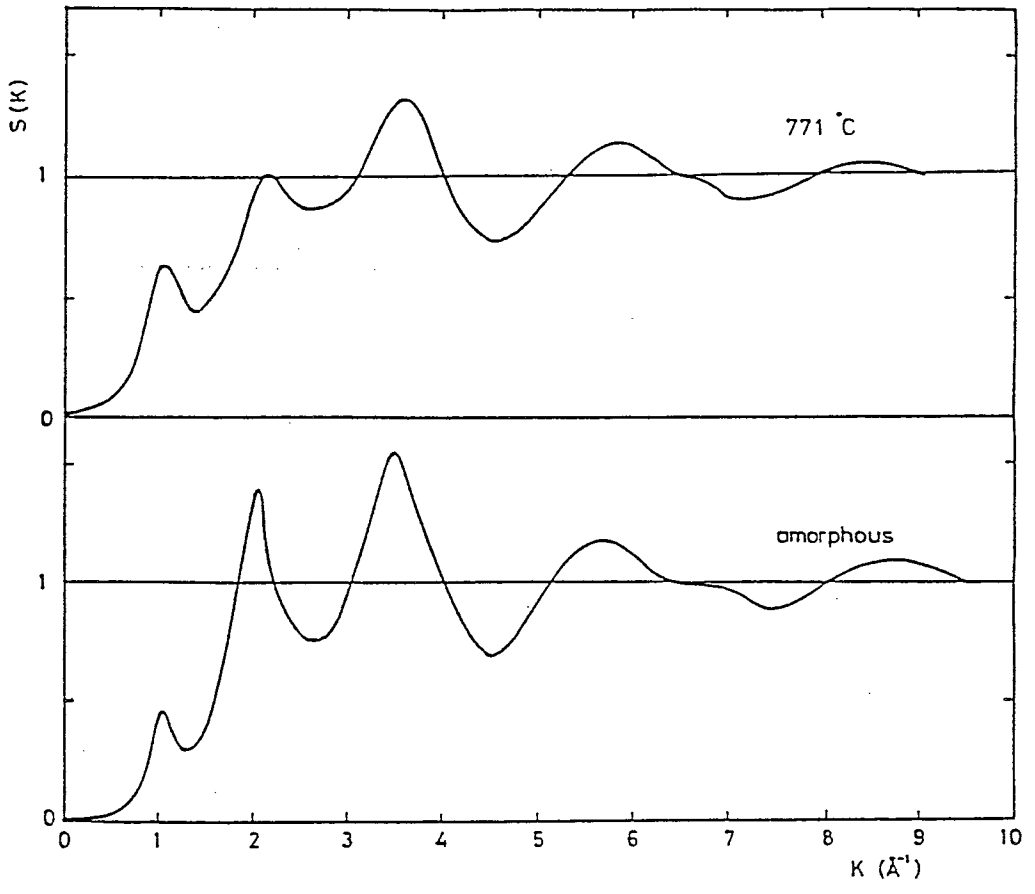

Figure 12: Structure factor $S(k)$ of amorphous $GeSe_2$ at room temperature and liquid $GeSe_2$ at 771 °C. A peak at 1.01 $Å^{-1}$ is called as FSDP which corresponds to the medium range structure whose correlation length is 6.22 Å. The FSDP is still remained in the structure factor of liquid phase (From Ref. 39).

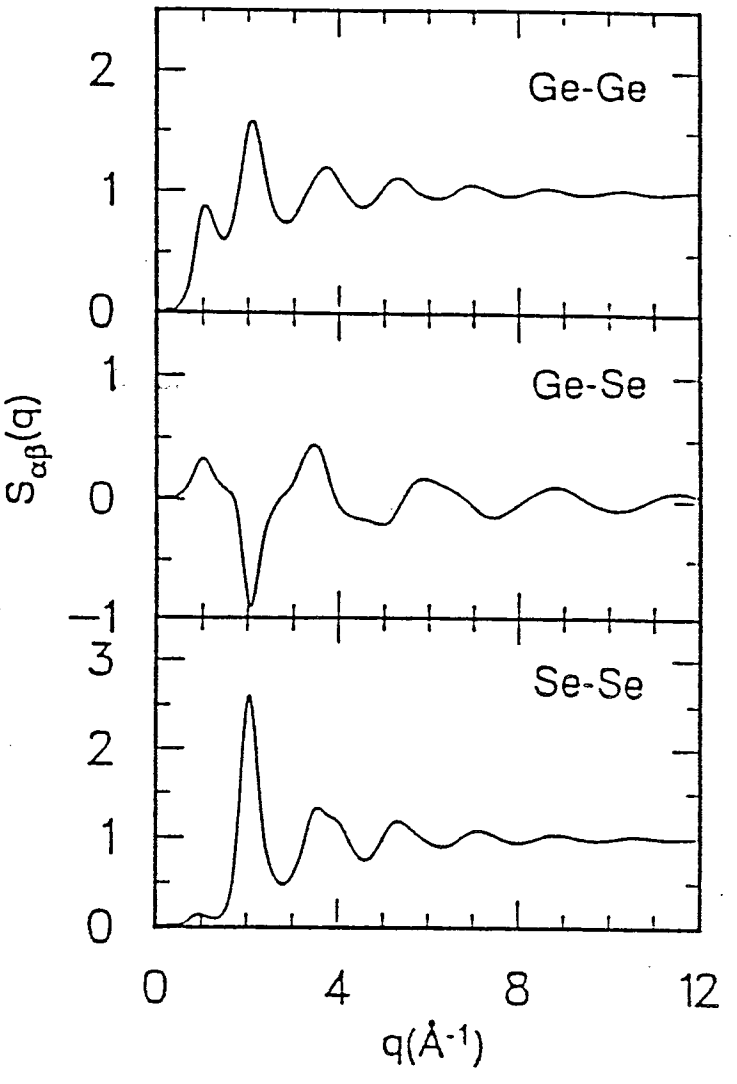

Figure 13: Partial structure factor for a–$GeSe_2$ at 300 K obtained by the molecular dynamics calculation. The FSDP mainly comes from the Ge–Ge correlation and partially from the Ge–Se correlation (From Ref. 40).

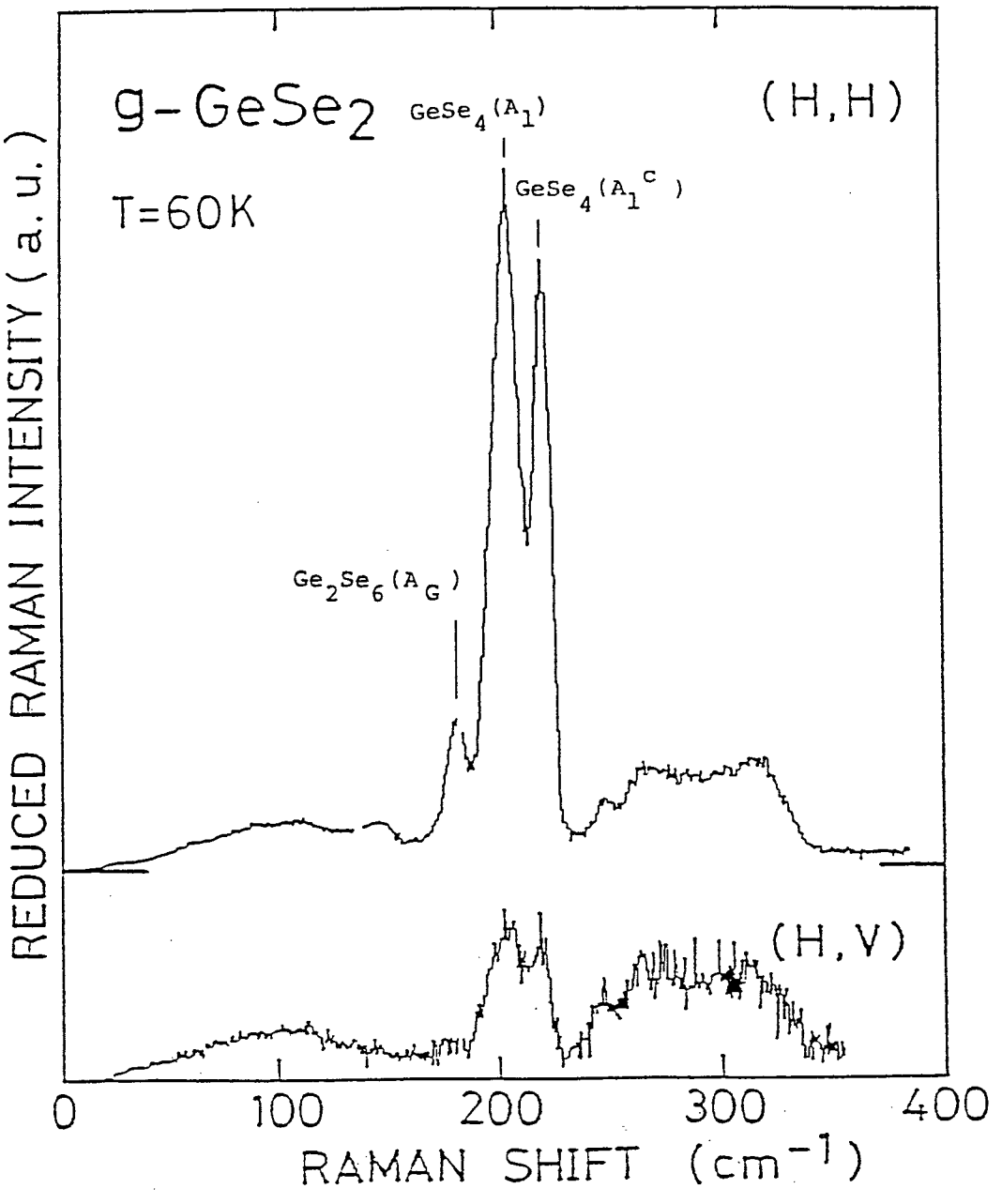

Figure 14: Polarized reduced Raman spectra of $GeSe_2$ bulk glass at 60 K. Excitation photon energy is 1.96 eV (6328 Å). The A_1 mode is due to the breathing motion of $GeSe_{4/2}$ tetrahedra. The A_G mode is due to the stretching motion of Ge–Ge wrong bonds. The origin of the A_1^C mode has been under controversy (From Ref. 41).

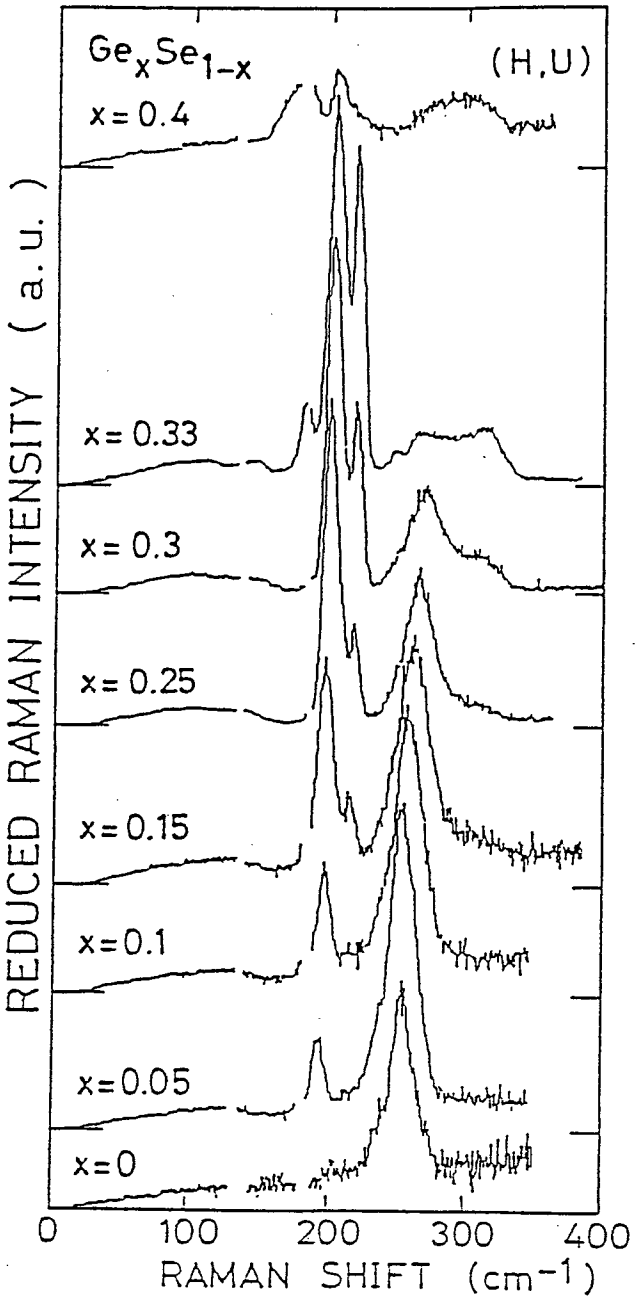

Figure 15: Reduced Raman spectra of Ge_xSe_{1-x} bulk glass over various compositions at 50 K. Excitation photon energy is 1.96 eV (He–Ne). The A_1 band increases with the consumption of the Se–Se mode at about 250 cm^{-1} as x increases. The A_C band appears and grows in the region of $x \geq 1/3$. Assuming that the intensity of the A_1 band increases in proportion to x, that of the A_1^C band increases slowly in small x region and then rapidly as x approaches to 1/3 (From Ref. 41).

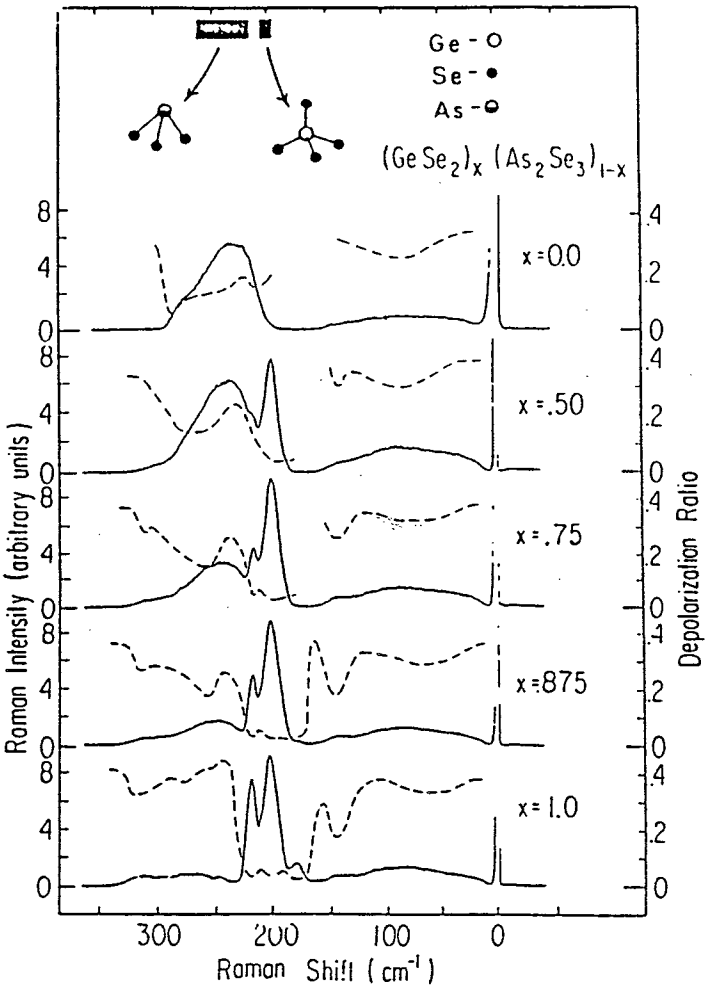

Figure 16: The Raman (—) and depolarization (- - -) spectra of $(GeSe_2)_x(As_2Se_3)_{1-x}$ at 11 K. The excitation photon energy is 1.55 eV (7993 Å, Krypton ion laser). The relevant local atomic structures and the frequency range of their bond stretching modes are shown in the top of the figure. The A_1^C band decreases with decreasing x. The increase of $AsSe_{3/2}$ molecules is supposed to destroy the medium-range structure of $GeSe_{4/2}$ tetrahedra (From Ref. 17).

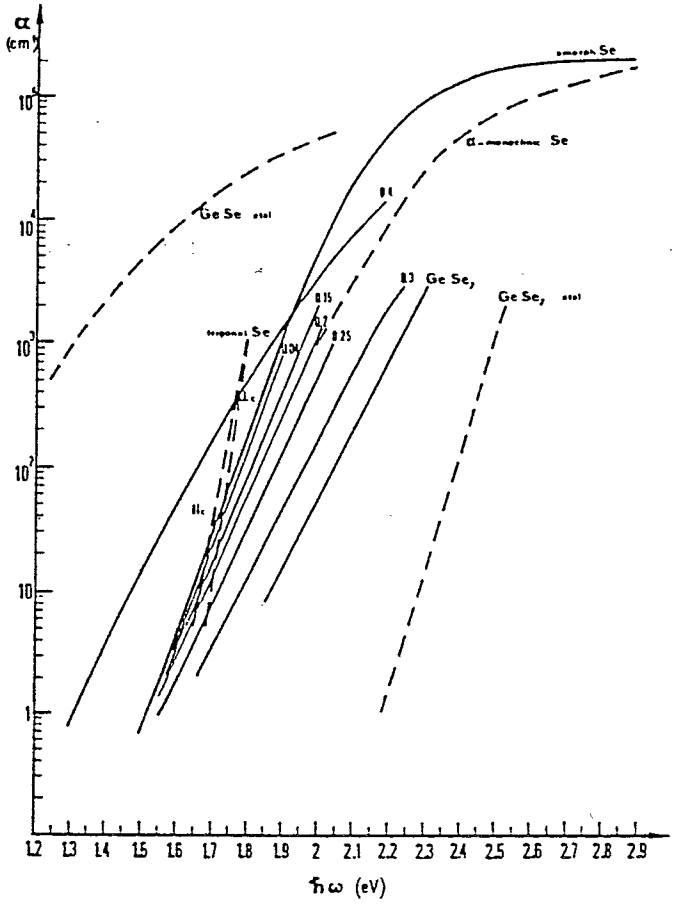

Figure 17: Absorption spectra of glassy Ge_xSe_{1-x}. Both for $x > 1/3$ and $x < 1/3$, the energy gap values are shifted to the lower energy side (From Ref. 10).

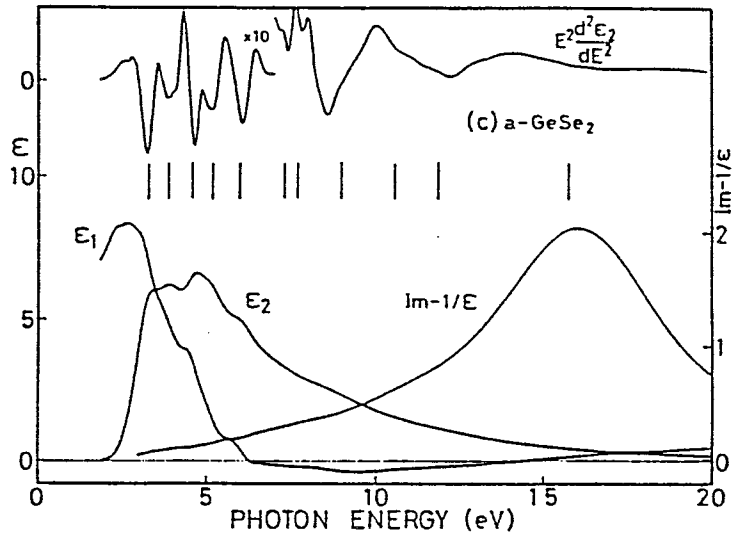

Figure 18: Dielectric functions of amorphous $GeSe_2$ at room temperature. The overall shape of ϵ_2 spectra consists of two peaks around 3 eV and 5 eV. The spectra resemble those of β–$GeSe_2$ very much. The vertical bars are calculated transition energies from the characteristic energy levels in Table 4. The detail of the assignment is described in Ref. 21 (From Ref. 21).

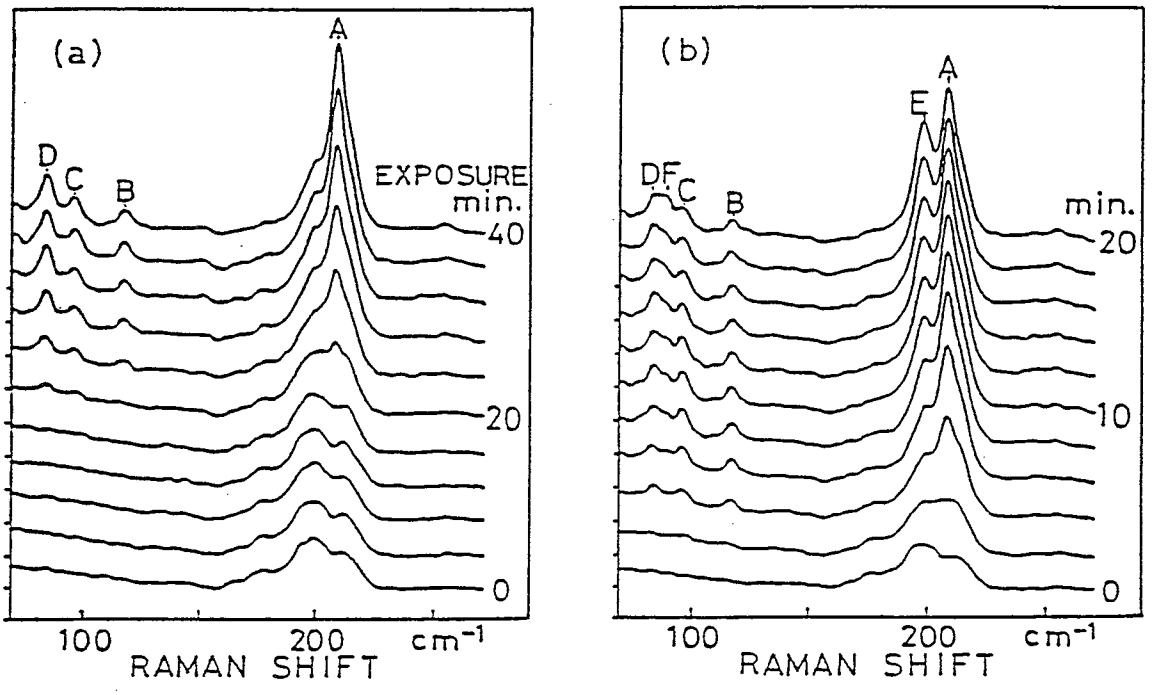

Figure 19: Time resolved Raman spectra of laser induced crystallization in $GeSe_2$. The Ar ion laser 5145 Å (2.41 eV) light are used for both crystallization and probing. (a) Type A: Only one crystalline phase β–$GeSe_2$ grows. (b) Type B: Two crystalline phases, α– and β–$GeSe_2$ grow successively. The peaks A through D correspond to β–$GeSe_2$ and the peaks E through F, α–$GeSe_2$ (From Ref. 42).

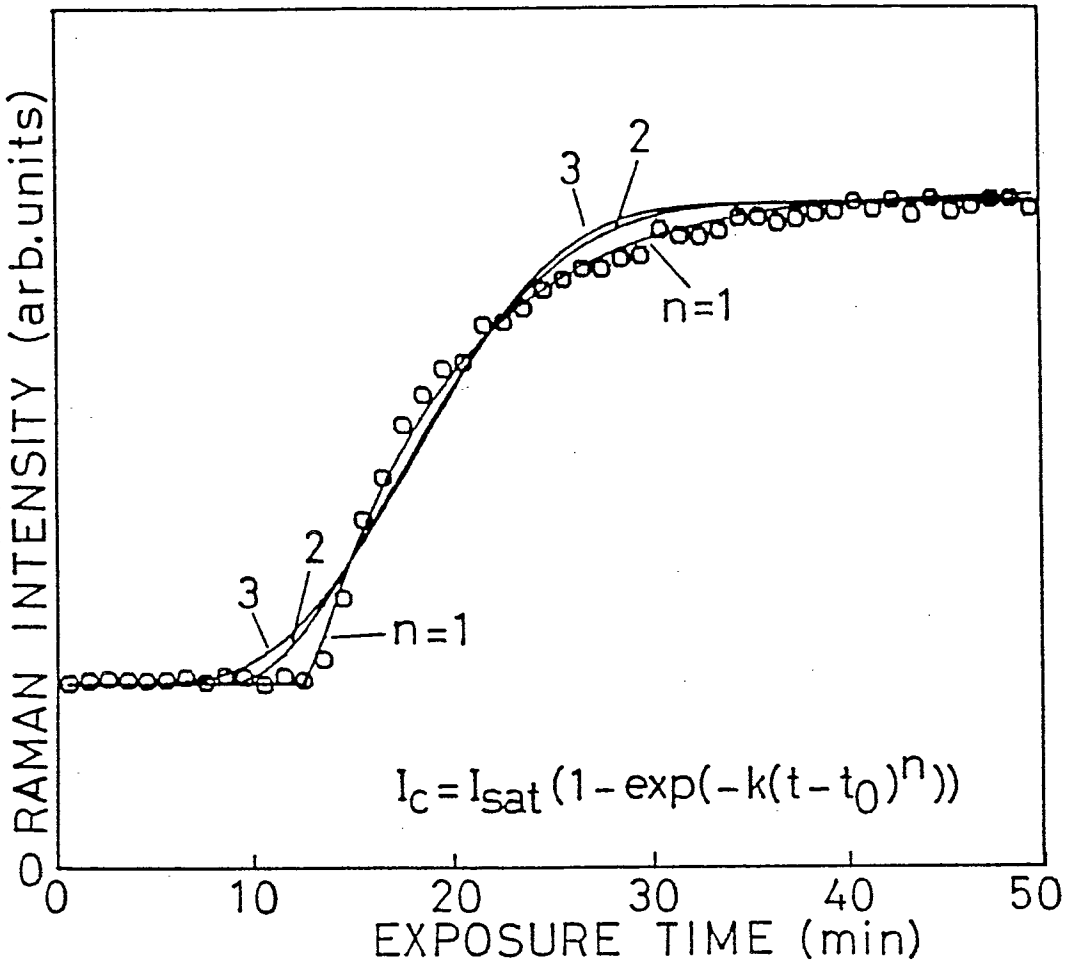

Figure 20: Growth curve of β–$GeSe_2$ in light-induced crystallization. The peak height of the 211 cm^{-1} band is plotted against the exposure time. Solid lines illustrate the empirical functions: $I_{sat}\{1-\exp(-k(t-t_0)^n)\}$ for $n = 1, 2, 3$. The best fit is given by $n = 1$ (From Ref. 27).

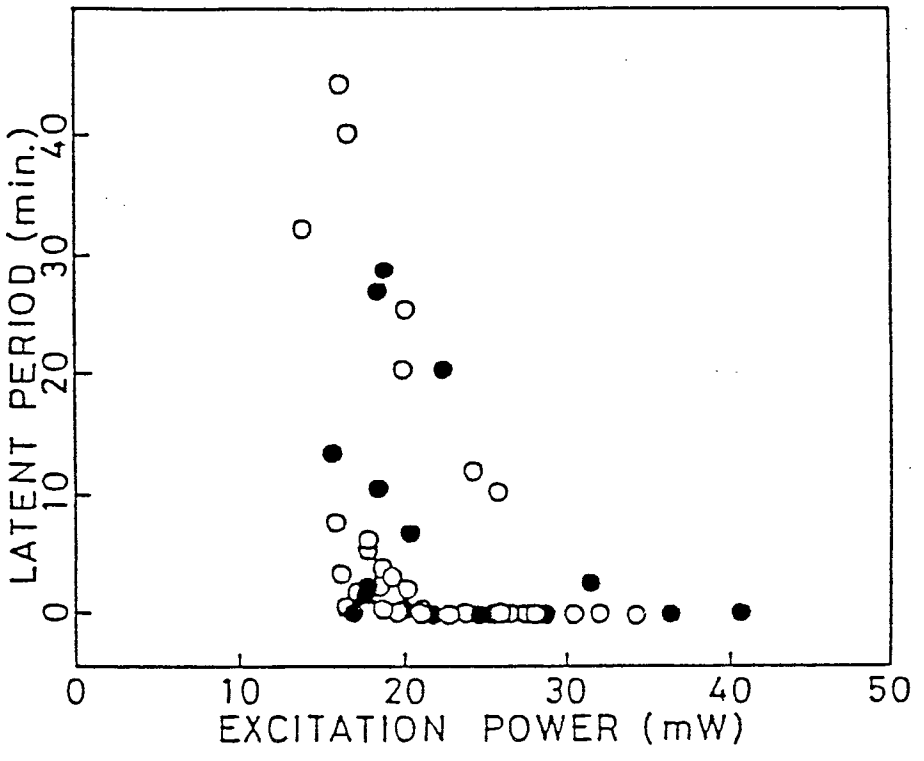

Figure 21: Excitation power dependence of the latent period t_0 in the light-induced crystallization at RT. The excitation photon energy is 2.41 eV (5145 Å). A threshold laser power exists at nearly 14 mW under which no crystallization is observed in the finite time period of the experiments. Open circles: type A, and closed circles: type B (From Ref. 27).

3 Experimental Procedure

3.1 Sample Preparation

Various types of $GeSe_2$ samples are prepared; (1) bulk single crystals; (2) amorphous films by vacuum-evaporation; (3) polycrystalline films by thermal annealing of vacuum-evaporated amorphous films and (4) polycrystalline films by thermal annealing of gas-evaporated amorphous films. Details of the preparation are described as follows.

3.1.1 Single Crystals

Bulk single crystalline β–$GeSe_2$ was grown from molten $GeSe_2$ by the Bridgman technique for more than ten days. The compound was made by the reaction of the 5N-grade elements, Ge and Se, in a 1:2 mole-ratio above 940 °C in a vacuum-sealed fused-silica tube. The crystalline axes a and b were determined by X-ray diffraction measurement using a precession camera. The precession photograph is shown in Fig. 22. Assuming $\beta = 90.65°$, the lattice constants are calculated to be $a = 7.09$ Å and $b = 16.9$ Å from the photograph. The values agree well with those in Table 1. Hereafter, β–$GeSe_2$ will be sometimes merely referred to as crystal or c–$GeSe_2$ and other two crystalline forms, α– and γ–$GeSe_2$, will be described explicitly.

For fear that there might be some residual strain in the crystals grown by the Bridgman technique, we also used the vapor phase growing technique. The mixture of Ge and Se elements in a vacuum-sealed fused-silica tube was pre-reacted in a rocking electric furnace above 940 °C over 12 hours. The same ampoule was set in a horizontal electric furnace and the crystals were grown in a temperature gradient of 654.6 °C → 653.0 °C for about 150 hours. There was no difference observed in the Raman spectra and the absorption spectra between the Bridgman grown sample and the vapor-phase grown sample.

3.1.2 Amorphous Films

Amorphous $GeSe_2$ films were made by vacuum-evaporation of $Ge_{0.34}Se_{0.66}$ bulk glass onto silica glass substrates (CORNING 7059) under the pressure of about 2×10^{-6} Torr. For the preparation of the evaporation source, Ge and Se elements weighted in a 0.34 : 0.66 mole ratio were sealed under a vacuum in a fused silica tube and were reacted in the rocking furnace above 940 °C over 12 hours. The heated ampoule was quenched directly from the furnace into iced water to obtain bulk glass. The predominant mode of sublimation of $GeSe_2$ is given by the reaction, $2GeSe_2(s)=2GeSe(g)+Se_2(g)$.[28,50] Because of the vapor pressure difference between GeSe(g) and $Se_2(g)$, the composition of the evaporation source should be to some extent Ge-rich composition to obtain the stoichiometric films. Thickness of the film during the evaporation was monitored by the transmissivity of He–Ne laser (6328 Å) where the transmissivity shows an oscillation by the interference due to multiple reflection in the film. If there are N transmissivity maxima except for the first maximum during the evaporation, the film thickness d is given by

$$d = \frac{N\lambda}{2n},$$

where λ is the wavelength of the laser (6328 Å) and n is the refractive index (about 2.7 at 6328 Å). The thicknesses were about 6000 Å for all amorphous samples.

3.1.3 Films Deposited by Evaporation in Ar Gas

Gas-evaporation films have prepared by the sublimation of $Ge_{0.34}Se_{0.66}$ bulk glass in Ar gas onto silica glass substrates (CORNING 7059). The evaporation system is shown in Fig. 23. The pressure of Ar gas is ranged from 0.08 Torr to 2 Torr. The nature of the films varied with the position of the substrate as well as with the gas pressure. In this experiment, all films are grown in front of the gas nozzle. The obtained films were observed by a scanning electron microscope. The photos will be shown in Sec. 4.2.1.

3.1.4 Polycrystalline Films

Polycrystalline films were prepared by two methods. 1) By thermal annealing of the amorphous films (Sec. 3.1.2) in $\sim$ 360 Torr Ar gas at various temperatures (425 $\sim$ 460 °C) for various time periods (30 min $\sim$ 18 hours). The thicknesses of the films were about 6000 Å $\sim$ 3 μm. 2) By thermal annealing of the gas-evaporated films (Sec. 3.1.3) in $\sim$ 360 Torr Ar gas at about 425 °C for 18 hours. The obtained films were observed by a scanning electron microscope. The photos will be shown in Sec. 4.2.1.

3.2 Raman Measurement

As excitation light sources of Raman measurement, a dye-laser (Rhodamine 6G), an Ar ion laser, and a He–Cd laser were used. The available wave length was ranged from 6060 Å (2.05 eV) to 4416 Å (2.81 eV) (Table 5). All Raman spectra were acquired in a back scattering configuration. The incident light was polarized vertical (V) to the plane of incident and scattered light and was focused onto a rectangular region of about 5mm×0.1mm of the sample surface by a cylindrical lens (line-focusing) or onto a point with diameter of 30 $\sim$ 50 μm on the sample surface by a spherical lens (point-focusing). Usually, the incident laser power was less than 10 mW. The line-focusing was used when we need to avoid light-induced effect and/or to reduce heating effect by laser irradiation. The scattered light polarized horizontal (H), vertical (V) or unanalyzed (U) was dispersed by a triple grating monochromator (JASCO TRS-505, double filter monochromator + single main monochromator, 1800 g/mm, 1 m) and was detected by a multi-channel photo-diode array with an image intensifier (Tracor Northern TN-6122). The width of the slit was 200 μm and the spectral resolution was about 1 cm^{-1} FWHM. The block diagram of Raman measurement system is shown in Fig. 24.

For the bulk single crystals, the natural-cleavage (001) surfaces were used for the Raman measurement. For the amorphous and polycrystalline films, the surfaces

Table 5: Energy and wave length of laser lines used in this experiment.

Energy (eV)	Wave length (Å)	
2.05	6046.0	Dye laser (Rhodamine 6G)
2.06	6019.6	
2.07	5992.5	
2.08	5964.9	
2.09	5935.6	
2.10	5907.3	
2.11	5880.6	
2.12	5852.7	
2.13	5824.5	
2.41	5145.33	Ar ion laser
2.47	5017.17	
2.50	4965.07	
2.54	4879.86	
2.60	4764.88	
2.62	4726.89	
2.66	4657.95	
2.71	4579.36	
2.81	4415.6	He–Cd laser

of the films were used for the measurement. The environmental temperatures of the samples were changed from 20 K to 700 K by a gas-flow-type cryostat (Janis 10CNDT, Fig. 25) or a furnace.

The sensitivity of overall measurement system was calibrated by the spectra of a halogen lamp as follows. The light from the halogen lamp can be approximately regarded as the black-body radiation. The number of radiated photons between the frequency of ν and that of $\nu + d\nu$ is given by

$$N(\nu)d\nu \propto \frac{\nu^2}{\exp(h\nu/k_BT) - 1}d\nu,$$

where T is the temperature of the lamp which is measured by an optical pyrometer. The light is dispersed by the system and brings the output $I(n)$ to the n-th cell of the detector, which is given by

$$I(n) = C(n)N(\nu(n))\Delta\nu(n),$$

where $\nu(n)$ is the central frequency of the dispersed light detected by the n-th cell, $\Delta\nu(n)$ the frequency range of the n-th cell, and $C(n)$ the sensitivity calibration function of the n-th cell. The measurement of $I(n)$ and T gives $C(n)\Delta\nu(n)$. Once determined the $C(n)\Delta\nu(n)$, the relation between a measured spectrum $x(n)$ and a true spectrum $X(\nu)$ is given by

$$X(\nu(n)) = \frac{x(n)}{C(n)\Delta\nu(n)}.$$

The spectrum $X(\nu)$ is proportional to the photon density with respect to the unit energy.

3.3 Optical Absorption Measurement

As the single crystalline samples for the optical absorption measurement, a piece of bulk single crystal was pealed off by using Scotch tape into thin pieces whose thickness ranged from 5 to 100 μm. The halogen-lamp light polarized parallel to the crystalline axis a or b ($\boldsymbol{E} \parallel \boldsymbol{a}$ or $\boldsymbol{E} \parallel \boldsymbol{b}$) by a polarizer was used as the light

source in the normal incidence to the (001) surface of the samples. Spectra ranged from 2.0 to 3.0 eV were measured by use of a double monochromator (SPEX 1680B, 1200 g/mm, 22 cm) and a photo-multiplier (HAMAMATSU R928). The environmental temperatures of the sample was changed from 20 K to 300 K by a cryostat. Absorption spectra were derived from these transmission spectra, taking account of the refractive index,[21] and the sample thickness which was calculated from the interference pattern in the transparent region of the transmission spectra.

The transmission spectra of amorphous films and polycrystalline films were measured by the same method described above. However, the transmission spectra were analyzed by assuming constant reflectivity instead of obtaining true absorption coefficients. This treatment does not cause significant error on the evaluation of the exciton transition energies in this experiment.

3.4 Light-Induced Crystallization

All the experiment of the light-induced crystallization were made in the amorphous $GeSe_2$ films (thickness: 6000 Å) on the silica glass substrates (CORNING 7059). The 5145 Å (2.41 eV) light of the Ar ion laser whose power was 5 $\sim$ 70 mW was focused onto the spot of 30 $\sim$ 50 μm diameter on the sample surface. The time resolved Raman spectra are recorded every one minute during the laser irradiation using the same equipment described in Sec. 3.2 where the excitation light was also used as the probing light. In order to clarify the roles of light irradiation and thermal excitation, the observation of the light-induced crystallization process was made at various environmental temperatures, 30 K, 90 K, 300 K, and 480 K using the cryostat or a sample holder heated by Ni–Cr heater.

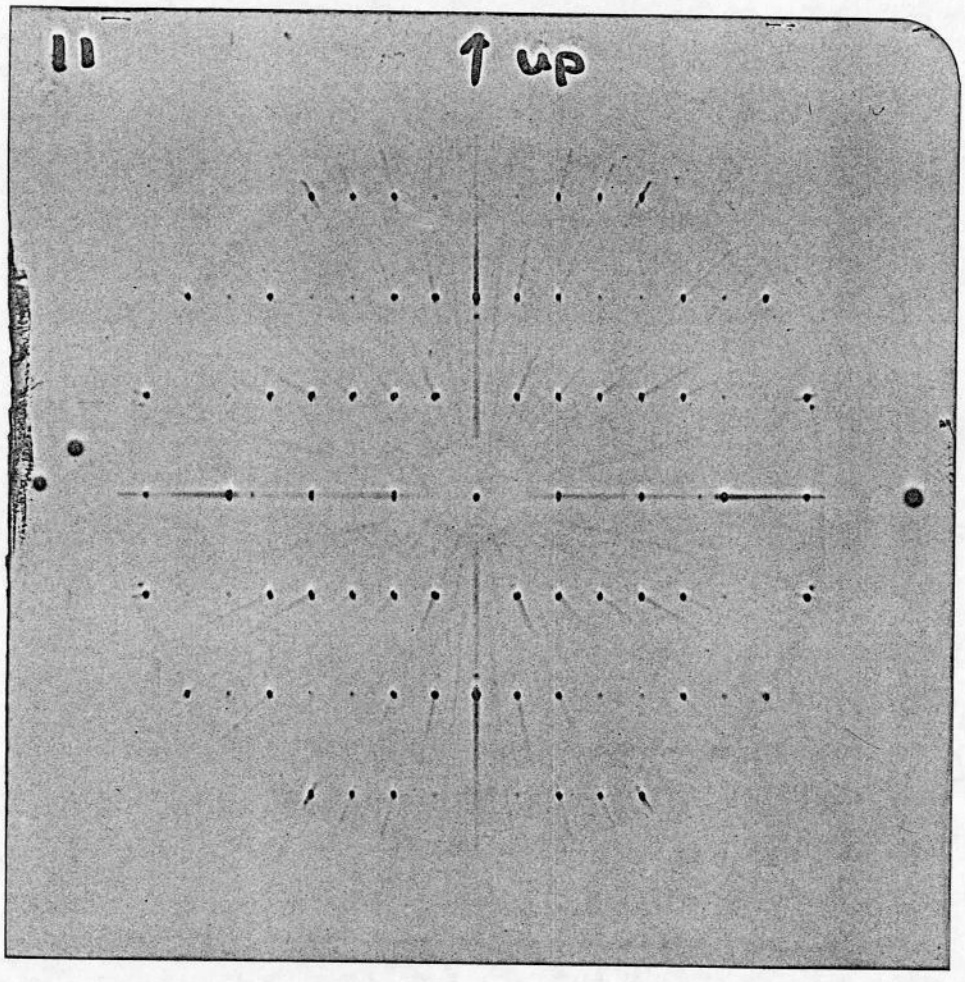

Figure 22: X-ray diffraction pattern of β–$GeSe_2$ using a precession camera. Cu k_α: $\lambda = 1.5418$ Å; distance between the sample and the film $d = 60.0$ mm; precession angle $\mu = 23.0°$; radius of the slit $R = 20$ mm; width of the slit $\Delta = 2$ mm; distance between the sample and the slit $r = 47.1$ mm. Assuming $\beta = 90.65°$, lattice constants are calculated to be $a = 7.09$ Å and $b = 16.9$ Å.

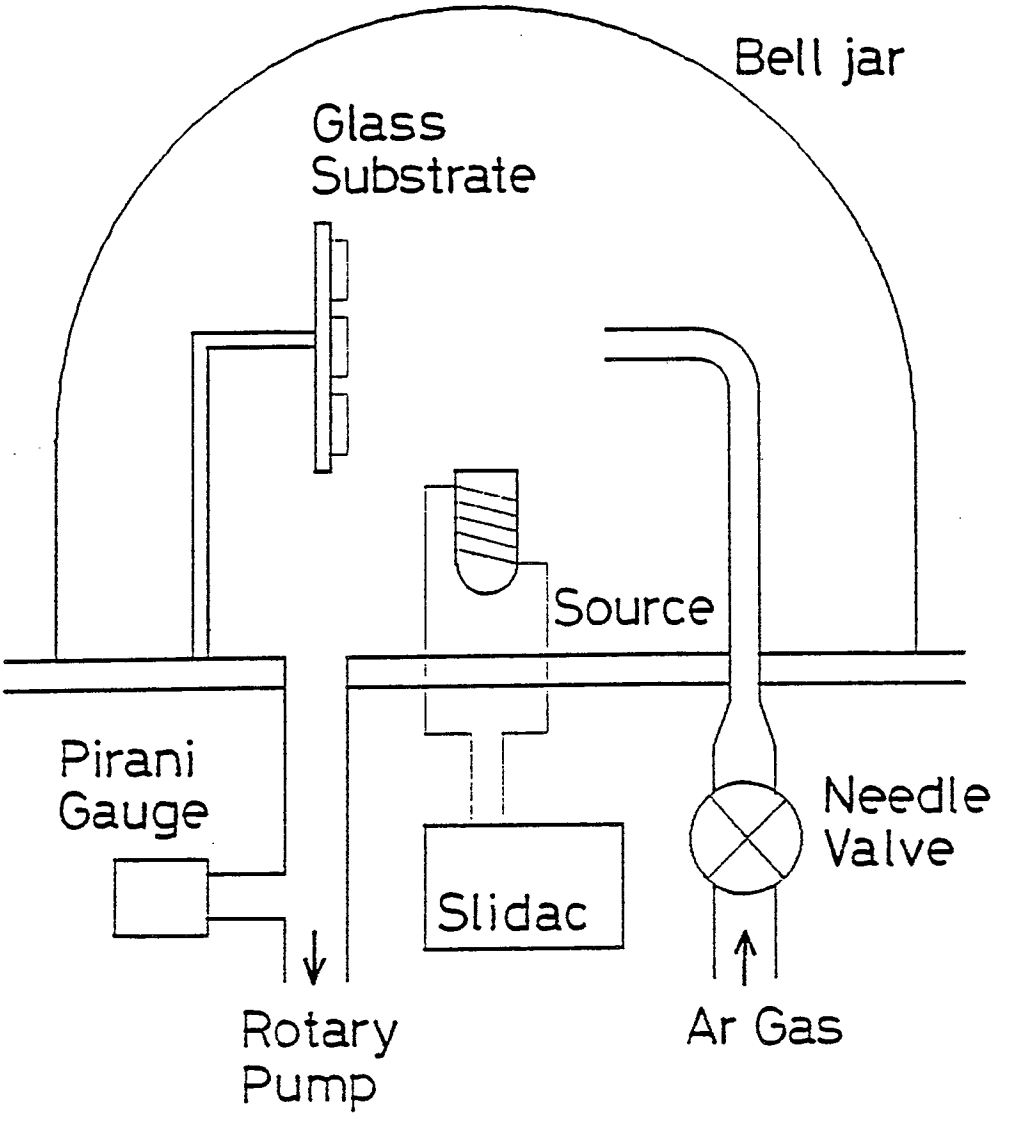

Figure 23: Schematic illustration of gas-evaporation film growth system.

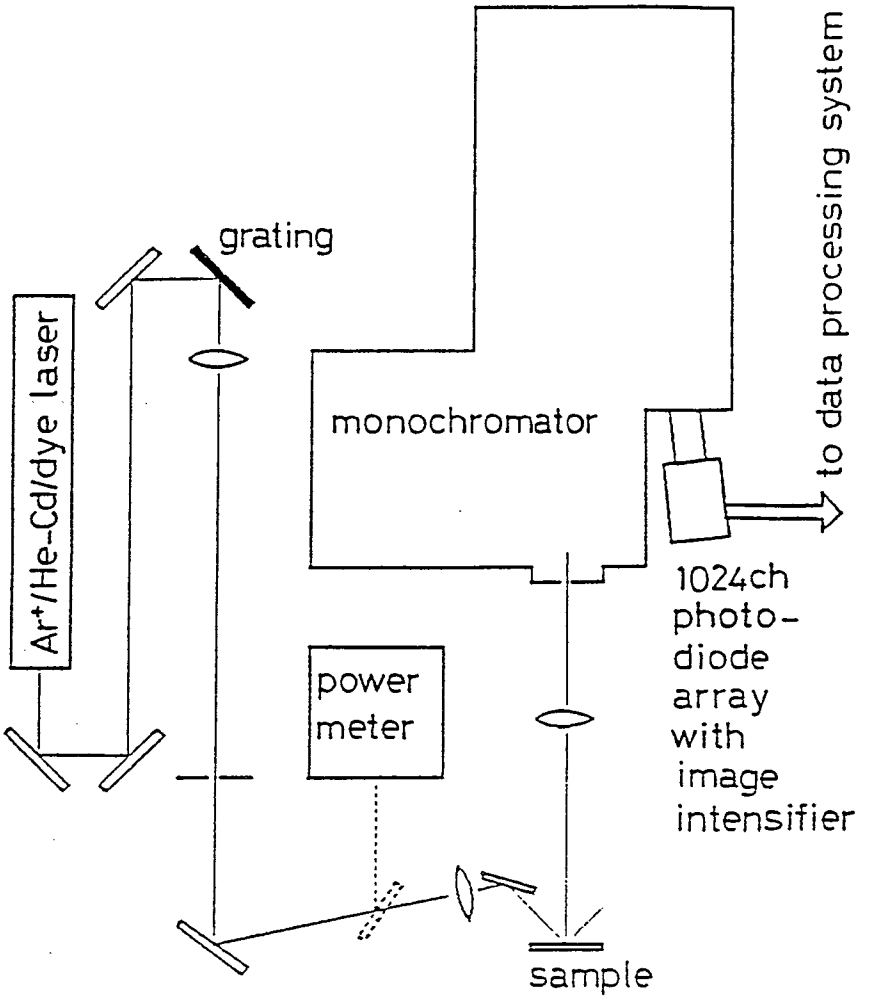

Figure 24: Block diagram of Raman measurement system.

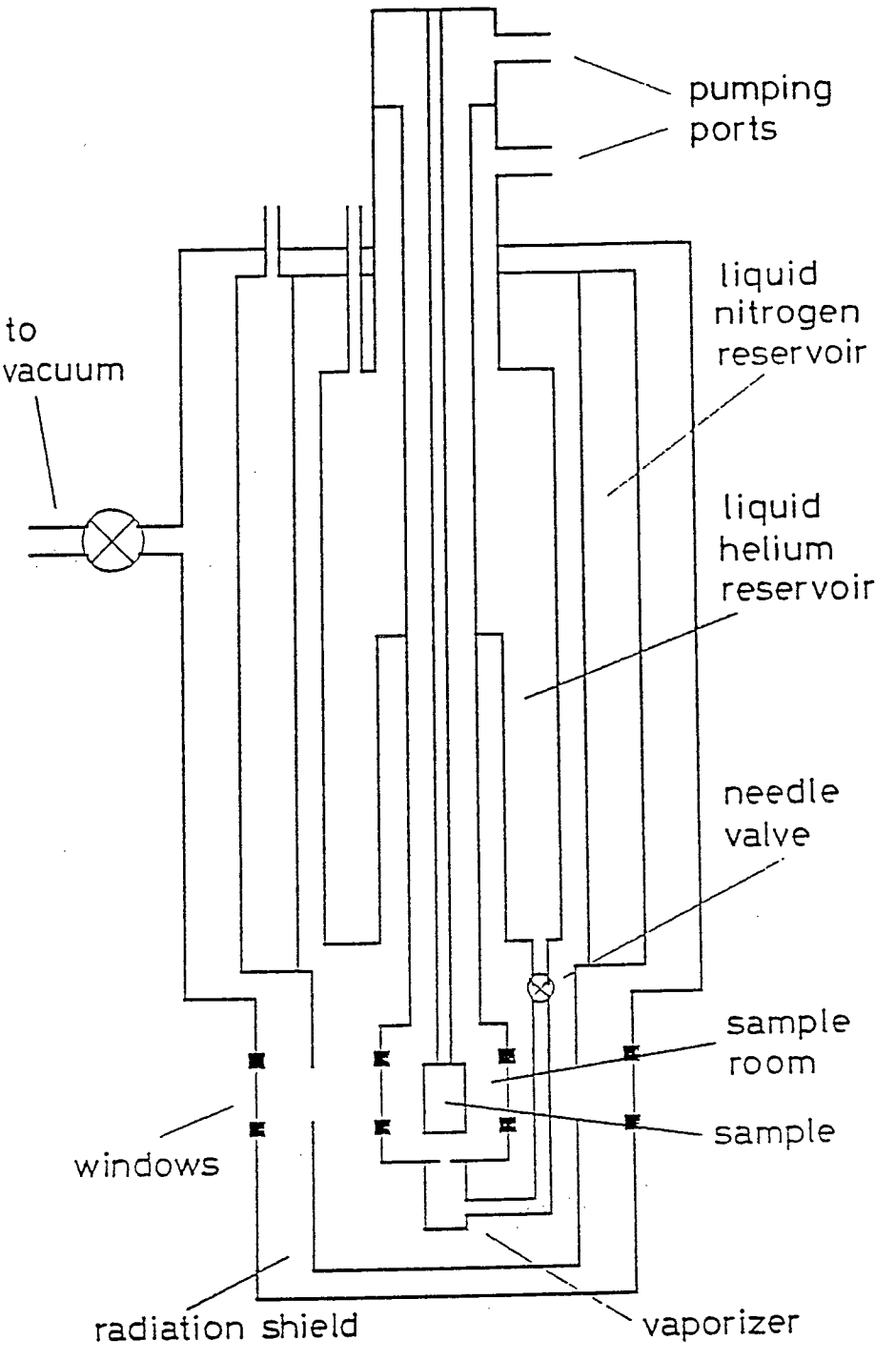

Figure 25: Schematic illustration of cryostat for low temperature measurement.

4 Results and Discussion

4.1 Single Crystal

4.1.1 Optical Absorption Spectra

Figure 26 shows the absorption spectra of the β–$GeSe_2$ bulk single crystal in the $\boldsymbol{E} \parallel \boldsymbol{a}$ and $\boldsymbol{E} \parallel \boldsymbol{b}$ polarizations at room temperature. For both polarizations, the absorption coefficients rise at about 2.4 eV. In the $\boldsymbol{E} \parallel \boldsymbol{a}$ polarization, two humps are observed at about 2.70 eV and 2.91 eV.[19–22]

As described in Sec. 2.1.3, the absorption measurement at low temperatures clarifies that the hump at about 2.70 eV is ascribed to an exciton transition. Figure 27 shows the absorption spectra of the β–$GeSe_2$ single crystal at various temperatures from 60 to 300 K in the $\boldsymbol{E} \parallel \boldsymbol{a}$ configuration. It is confirmed that, as the temperature decreases, the energy position of the exciton absorption peak shifts toward the higher energy side and the width of the peak becomes sharp.

4.1.2 Raman Spectra

Stokes Raman spectra of the β–$GeSe_2$ single crystal excited by the 2.41 eV (5145 Å) and 2.71 eV (4579 Å) light at RT in the c(a,a)$\bar{c}$ and c(b,b)$\bar{c}$ configurations are shown in Fig. 28. In Fig. 28 (a) (2.41 eV excitation), there is a strong Raman peak at about 211 cm^{-1}. The line shape of the 211 cm^{-1} peak is slightly asymmetric and is decomposed into three bands: one strong band at about 211 cm^{-1} and two weak bands at about 208 cm^{-1} and 216 cm^{-1}. The splitting of these three bands was clearly shown in the spectra at low-temperature by Popović and Stolz[23] where the 208 cm^{-1} and 216 cm^{-1} modes are also very weak. As described in Sec. 2.1.2, the 211 cm^{-1} band is ascribed to the breathing motion of the corner-sharing chain $GeSe_{4/2}$ tetrahedra and the 216 cm^{-1} band is due to the breathing motion of the edge-sharing bridge $Ge_2Se_{8/2}$ bi-tetrahedra.

Under the 2.71 eV (4579 Å) excitation in the c(a,a)$\bar{c}$ configuration, we have found

Table 6: Raman peak positions and widths (FWHM) of single crystalline β–$GeSe_2$ in the c(a,a)$\bar{c}$ configuration at RT. The spectral resolution is about 1 cm^{-1} FWHM.

	211 cm^{-1} band		216 cm^{-1} band		
Excitation energy (eV)	Position (cm^{-1})	Width (cm^{-1})	Position (cm^{-1})	Width (cm^{-1})	216–211 splitting (cm^{-1})
2.06	210.8	4.5	216.2	3.7	5.4
2.07	210.3	4.6	215.7	3.8	5.4
2.09	212.5	4.5	217.8	4.0	5.3
2.10	212.8	4.5	218.2	3.6	5.4
2.11	210.7	4.7	216.1	4.0	5.4
2.12	210.5	4.7	215.8	4.1	5.3
2.13	211.8	4.7	217.7	3.9	5.5
2.41	211.4	5.0	217.3	4.1	5.9
2.47	211.8	5.1	217.7	4.5	5.9
2.50	210.6	5.2	216.5	5.3	5.9
2.54	211.4	5.1	217.3	4.5	5.9
2.60	211.7	5.3	217.6	5.9	5.9
2.62	212.8	5.2	218.7	5.4	5.9
2.66	212.0	5.5	217.9	4.6	5.9
2.71	210.5	5.7	216.6	5.8	6.1
2.81	213.1	5.8	219.0	5.6	5.9

Table 7: Raman peak positions and widths (FWHM) of single crystalline β–$GeSe_2$ in the c(b,b)$\bar{c}$ configuration at RT. The spectral resolution is about 1 cm^{-1} FWHM.

	211 cm^{-1} band		216 cm^{-1} band		
Excitation energy (eV)	Position (cm^{-1})	Width (cm^{-1})	Position (cm^{-1})	Width (cm^{-1})	216–211 splitting (cm^{-1})
2.06	211.0	4.5	216.4	3.8	5.4
2.07	210.7	4.6	216.1	3.8	5.4
2.09	212.4	4.5	217.8	4.1	5.4
2.10	212.8	4.5	218.2	3.5	5.4
2.11	210.6	4.6	216.0	3.8	5.4
2.12	210.6	4.5	215.9	4.0	5.3
2.13	211.7	4.5	217.0	4.0	5.3
2.41	211.4	5.0	217.3	4.0	5.9
2.47	211.7	5.1	217.6	4.3	5.9
2.50	210.6	5.2	216.5	4.6	5.9
2.54	211.3	5.2	217.2	4.6	5.9
2.60	211.8	5.2	217.2	4.4	5.4
2.62	212.6	5.2	218.5	4.6	5.9
2.66	212.0	5.3	217.9	5.9	5.9
2.71	210.7	5.9	216.6	6.4	5.9
2.81	213.0	5.8	218.9	5.3	5.9

that a drastic change occurs in the spectra:[51] the 216 cm^{-1} band becomes stronger than the 211 cm^{-1} band as shown in Fig. 28 (b). Among the available excitation laser lines of the present experiments, this relative intensity change of two bands is most remarkable under the 2.71 eV excitation in the c(a,a)$\bar{c}$ configuration. On increasing excitation energy to 2.81 eV (4416 Å) in the c(a,a)$\bar{c}$ configuration, the 216 cm^{-1} band becomes weaker than the 211 cm^{-1} band again but is still as strong as half of the 211 cm^{-1} band. The change seems to be related to the 2.70 eV exciton transition which is observed only in the $\boldsymbol{E} \parallel \boldsymbol{a}$ polarization. There is no appreciable change in the spectra of the c(b,b)$\bar{c}$ configuration by varying the excitation photon energy. In Tables 6 and 7, the peak positions and the peak widths (FWHM) of the 211 cm^{-1} and 216 cm^{-1} bands for various excitation photon energies are shown. The values are obtained through the least-squares fitting of the peak around 211 cm^{-1} by two or three gaussians. The peak positions agree with each other within the experimental accuracy. The peak widths do not change so much depending on the excitation energy and depending on the configurations, c(a,a)$\bar{c}$ and c(b,b)$\bar{c}$.

4.1.3 Resonance Effect

The Raman scattering intensities and the Raman cross-sections of the 211 cm^{-1}, 216 cm^{-1}, and 153 cm^{-1} bands versus the excitation photon energy are shown in Figs. 29 (a) and (b). The Raman intensity is defined to be the area of each peak which is proportional to the scattered photon-number normalized to the incident photon-number. If one ignores the interference between the multiple reflections in thin sample films, the Raman cross-section S is obtained from the relation:

$$I_s \propto I_e(1-R_s)(1-R_e)\int_0^D e^{-\alpha_s x}e^{-\alpha_e x}S\,dx,$$

where I_s denotes the Raman scattering intensity, I_e the intensity of the incident light, D the sample thickness, R the reflectivity, and α the absorption coefficient. The suffix letters s and e denote the quantity for the scattered and the incident lights, respectively. In reality, the ignorance of the interference might be inappropriate for

the transparent region $h\nu \sim 2.0$ eV, but the error would not be important here.

In Fig. 29 (a), the Raman scattering intensity first increases and then decreases with increasing excitation photon energy. On the other hand, the Raman cross-section increases monotonically with increasing excitation photon energy except for the region near 2.71 eV as shown in Fig. 29 (b). The result that the scattering intensity decreases in the high excitation energy region is explained by the decrease in total scattering volume, which results from increase in the absorption coefficients. In the Raman cross-section of the c(a,a)$\bar{c}$ configuration, there is a peak or a shoulder at 2.71 eV for the 216 cm^{-1} band. On the other hand, it seems that there is a dip around 2.71 eV for the 211 cm^{-1} band. The 216 cm^{-1} band becomes slightly stronger than the 211 cm^{-1} band at the 2.71 eV excitation in the c(a,a)$\bar{c}$ configuration at the expense of the 211 cm^{-1} intensity.

The absence of $\triangle$ in Fig. 29 around 2.6 eV is due to a practical lack of the 153 cm^{-1} peak. The 153 cm^{-1} band in the c(a,a)$\bar{c}$ configuration reappears around 2.7 eV and becomes strong at the 2.71 eV excitation. On the other hand, that for the c(b,b)$\bar{c}$ configuration remains undetectable around 2.7 eV. The nature of the 153 cm^{-1} band will be discussed in Ref. 32.

As described above, the "resonant" effect, which is the relative enhancement of the 216 cm^{-1} band to the 211 cm^{-1} band, is related to the 2.7 eV exciton transition. The exciton transition energy increases with decreasing temperature. If one measures the Raman spectra of the single crystalline β–$GeSe_2$ in the c(a,a)$\bar{c}$ configuration with the excitation energy higher than 2.71 eV at various temperatures, the "resonant" effect will be observed at the temperature lower than RT (the temperature-tuning of the exciton energy). The temperature dependence of the exciton transition energy is shown by the open circles in the upper half of Fig. 30. Each energy value is determined by the second-energy-derivative of the absorption coefficient curves in Fig. 27. The result well agrees with the previous survey by Boiko et al..[22] Figure 31 shows the Raman spectra of the single crystalline $GeSe_2$ in the c(a,a)$\bar{c}$ configuration with the 4416 Å (2.81 eV) excitation at 200 K and 20

K. At 20 K, the exciton transition energy is greater than 2.81 eV and the 211 cm^{-1} band is much greater than the 216 cm^{-1} band. On the other hand, at 200 K where the exciton transition energy is comparable with the excitation light energy, the 216 cm^{-1} band becomes enhanced at the expense of the 211 cm^{-1} band. The 153 cm^{-1} band becomes appreciable at 200 K in concordance with the enhancement of the 216 cm^{-1} band. The temperature dependence of the intensity ratio of the 216 cm^{-1} band to the 211 cm^{-1} band in the spectra excited by the 2.81 eV light is shown in the lower half of Fig. 30. At the temperature where the ratio is maximized, the exciton transition energy is near the excitation photon energy 2.81 eV.

Let us consider about the microscopic origin of the relative enhancement of the 216 cm^{-1} band to the 211 cm^{-1} band at the 2.71 eV excitation in the c(a,a)$\bar{c}$ configuration and about the 2.70 eV exciton transition in the $\boldsymbol{E} \parallel \boldsymbol{a}$ polarization at RT.

As described in Sec. 2.1.2, it has been pointed out that the vibration of 216 cm^{-1} is the symmetric breathing mode of the edge-sharing bridge $Ge_2Se_{8/2}$ bi-tetrahedra.[12] We would like to further propose that the 216 cm^{-1} vibration is quasi-localized at the edge-sharing bi-tetrahedra. The term "quasi-localized" means that the vibrations at each edge-sharing bi-tetrahedra are (quasi-) independent of each other. Our recent calculation on the vibrational modes of c–$GeSe_2$ supports this assignment.[32] The schematic illustration of the 216 cm^{-1} vibration from this calculation is shown in Fig. 32. In the figure, the vibrational amplitude of the Se atoms in the edge-sharing tetrahedra (B,C,D) is much greater than that of the Se atoms in the corner-sharing tetrahedra (A).

As for the electronic structure, the valence band maximum of c–$GeSe_2$ consists of the Se 4p lone-pair electrons (See Sec. 2.1.3). The lone-pair electrons of the Se atoms at the edge-sharing-sites D (D′) in Fig. 32 and at the corner-sharing-sites A (A′) will have higher energy than those of the Se atoms at the corner-sharing sites B and C. The reason is explained as follows: 1) The 4p lone-pair orbitals at two neighboring Se atoms at D–D′ or A–A′ are parallel; 2) These lone-pair orbitals are

slightly overlapping each other to form bonding (π^*) and anti-bonding (π) orbitals which are quasi-localized at the edge-sharing bi-tetrahedra. Both π and π^* are occupied; 3) The energy level of π^* has the higher energy than the non-splitting Se $4p$ lone-pair states. The vector which is directed along the lone-pair orbitals at the D (D′) site has a large component along the a axis and the vector along the orbitals at the A (A′) site has a large component along the b axis. Therefore the lone-pair electrons at D are excited by the $\boldsymbol{E} \parallel \boldsymbol{a}$ light, while those at A, by the $\boldsymbol{E} \parallel \boldsymbol{b}$ light. In the case of the $\boldsymbol{E} \parallel \boldsymbol{a}$ excitation, the 2.70 eV exciton will be created by the optical excitation of electrons from the π^* band of the Se atoms at the edge-sharing bi-tetrahedra (site D) to the s–like anti-bonding state of the Ge atoms which belongs to the edge-sharing bi-tetrahedra. The 2.70 eV exciton will be quasi-localized around the edge-sharing bi-tetrahedra. On the other hand, in the case of the $\boldsymbol{E} \parallel \boldsymbol{b}$ excitation, the exciton transition is not observed. The fact will be explained as follows: 1) The transition is forbidden from the symmetry of the crystal. 2) The π^* orbitals of the Se atoms at the corner-sharing chain (site A) are extended over the chain, while the π^* at the edge-sharing site (D) are quasi-localized. In such case, the exciton originated from π^* at A will have lower binding energy and will be more difficult to be created than that from D.

In above assignments of the 216 cm^{-1} vibration and the 2.70 eV exciton, the resonant enhancement of the 216 cm^{-1} band will be understood because such excited state of electrons will be strongly coupled with the 216 cm^{-1} vibration quasi-localized on $Ge_2Se_{8/2}$ bi-tetrahedra. For further clarification, a detailed theoretical calculation on the electronic band structure will be necessary.

The exciton transition energy varies with pressure as well as with temperature. The pressure dependence of the energy gap value for single crystalline β–$GeSe_2$ has not been reported yet. However, the energy gap value of β–$GeSe_2$ is supposed to decrease with increasing pressure, since in glassy $GeSe_2$, glassy GeS_2, α–GeS_2, and β–GeS_2, such pressure dependence has been reported.[52,53] Thus, by applying high pressure to β–$GeSe_2$, it is expected that the exciton energy can be tuned to the

excitation photon energy for Raman scattering and the relative enhancement of the 216 cm^{-1} band to the 211 cm^{-1} band will be observed. Murase et al. have studied the Raman spectra of β–$GeSe_2$ at high pressures.[54] As shown in Figs. 33 and 34, an extra Raman band γ appears and grows at just above the 211 cm^{-1} band with increasing pressure. The γ–band corresponds to the 216 cm^{-1} band at the standard pressure. The existence of the γ–band is clear under the pressure higher than $\sim$ 30 kbar. The appearance of this extra line may be explained as follows: 1) The applied pressure causes the energy of the 2.70 eV exciton transition at the standard pressure to shift towards the low energy side. 2) The 216 cm^{-1} band is enhanced relatively to the 211 cm^{-1} band around the pressure where the 2.70 exciton transition energy becomes close to the excitation photon energy (6328 Å (1.96 eV), in this case). Another extra band β appears in Fig. 33 under the pressure higher than $\sim$ 40 kbar. This band may be ascribed to some phase transition induced by high pressure.[54]

4.2 Polycrystalline Film

The vibrational and electronic structures of the crystal will be affected by the disorder in the crystal. In order to know these disorder-induced effects, various types of polycrystalline films are prepared and investigated.

4.2.1 Scanning Electron Microscope Observations

The preparing conditions of the polycrystalline films are listed in Table 8. All the as-deposited and annealed films are observed by a scanning electron microscope (JEOL, JSM–6400). The as-deposited films by vacuum-evaporation (#1$\sim$#4) have flat featureless surfaces, while the as-deposited films by gas-evaporation (#5$\sim$#9) show various structures depending on the preparing conditions (Figs. 35$\sim$42). The Ar gas pressure at the evaporation decreases in a series of the films #5 to #9. In the as-deposited films #5$\sim$#7, a cotton-candy-like structure is observed. The width of fibers is less than 0.1 μm. In the films #8 and #9, there are finer structure

Table 8: Preparing conditions of the polycrystalline films #1~#9. Films by a vacuum-evaporation or a gas-evaporation in Ar gas are annealed in ~ 360 Torr Ar gas to obtain the polycrystalline films.

Sample No.	Thickness of film	Deposition method	Annealing temperature	Annealing period
#1	6000 Å	vacuum-evaporation	425 °C	18 hours
#2	3 μm	vacuum-evaporation	435 °C	18 hours
#3	3 μm	vacuum-evaporation	460 °C	90 min.
#4	6000 Å	vacuum-evaporation	425 °C	18 hours
#5	unknown	gas-evaporation (2 Torr)	421 °C	18 hours
#6	unknown	gas-evaporation (1.2 Torr)	423 °C	18 hours
#7	unknown	gas-evaporation (0.45 Torr)	423 °C	18 hours
#8	unknown	gas-evaporation (0.1 Torr)	424 °C	18 hours
#9	unknown	gas-evaporation (0.08 Torr)	424 °C	18 hours

like) than in the films #5~#7. The structure becomes cotton-candy-like for the Ar gas pressure higher than 0.3 Torr and cloud-like for the pressure lower than 0.3 Torr. After the annealing, the following structures appear:

- #5: the glue-like structure where the width of the channel is less than 1 μm.
- #6 and #7: the coral-like structure.
- #8 and #9: the glassy-lava-like structure with worm holes. In the film #9, the needle-like structure is embedded in the glassy-lava-like region.
- #1~#4: The initial flat surface is divided by many cracks to form islands. In the flat islands, the small platlet-structure is embedded.

A rough relation between the Ar gas pressure at the depostion of the film and the morphology of the as-deposited and annealed films are shown in Fig. 43.

4.2.2 Optical Absorption Spectra

Figure 44 shows the optical densities of the polycrystalline film #1. In the spectra, there is a hump around 2.57 eV at 300 K. This hump is related to the exciton transition because it becomes sharpened as the temperature decreases from 300 K to 60 K as shown in Fig. 44. The exciton transition energy of the polycrystalline film #1 (2.57 eV) is considerably lower than that of the single crystal (2.70 eV).

4.2.3 Raman Spectra

The Raman spectra and its excitation energy dependences are different among the polycrystalline film samples depending on their preparing conditions. First, the RT Raman spectra of the polycrystalline film #1 are shown in Fig. 45. The excitation photon energies are 2.41 eV (C) and 2.54 eV (D). For the convenience, the changes in the RT Raman spectra of the single crystalline β–$GeSe_2$ by varying the excitation photon energy are again shown in Figs. 45 A and B. Figure 45 C shows the spectra of the polycrystalline film #1 by the 2.41 eV excitation in the (VV) configuration

at RT. There is an intense line at 211 cm^{-1} which is accompanied by a shoulder at about 216 cm^{-1}. The shoulder at about 216 cm^{-1} is much stronger than that in the spectra of the single crystal by the same 2.41 eV excitation in Fig. 45 A. As shown in Fig. 45 D, further enhancement of the 216 cm^{-1} band is observed by 2.54 eV excitation in the polycrystalline film.

In Fig. 46, the excitation energy dependence of the Raman scattering intensities of the 211 cm^{-1} and the 216 cm^{-1} band for the polycrystalline film #1 and the single crystalline β–$GeSe_2$ are shown. The 216 cm^{-1} band becomes slightly strong than the 211 cm^{-1} band at the expense of the 211 cm^{-1} intensity for the polycrystalline film at 2.54 eV excitation as is observed for the single crystal at 2.71 eV excitation.

In Fig. 47, the intensity ratio of the 216 cm^{-1} band to the 211 cm^{-1} band at RT versus the excitation photon energy for the polycrystalline film #1 is shown with that for the single crystal.[55] In both cases, strong peaks are observed. The peak position in the polycrystalline film #1 is located at about 2.54 eV, whereas that in the single crystal is located at about 2.71 eV. These peak energies (resonance energy) agree with the exciton transition energies 2.57 eV for the polycrystalline film #1 and 2.70 eV for the single crystal. The problem is why the resonance energies differ between the polycrystalline film #1 and the single crystal. One of differences between poly- and single-crystals is that the grain orientation in the polycrystalline film is random, while the orientation of the single crystal is fixed in $c(a,a)\bar{c}$. However, in the other configurations, $c(b,b)\bar{c}$ and $a(c,c)\bar{a}$, no noticeable enhancement of the ratio is observed for the single crystal in the excitation energy range from 2.41 to 2.81 eV. The difference between the resonance energy of the polycrystalline film #1 and that of the single crystal is not explained by the random orientation of grains in the film, but most likely by the fact that the polycrystalline film is more disordered and contains more defects than the single crystal.

The behavior of the resonance varies depending on the preparing conditions of the polycrystalline films. Figures 48 and 49 show some Raman spectra of other polycrystalline films #2~#5. The intensity ratio of the 216 cm^{-1} band to the 211

cm^{-1} band of those polycrystalline films are shown in Figs. 50 and 51. The results can be roughly divided into two groups: 1) One is the case for the film #2. The 216 cm^{-1} band is rather weak in the spectrum of 2.41 eV (5145 Å) excitation (Fig. 48 A) and slightly increases at 2.71 eV (4579 Å) excitation (Fig. 48 B). There is a peak at 2.71 eV in the intensity-ratio spectra for the sample #2. The behavior corresponds to that of the single crystal. 2) The other group is the cases for the films #3~#5. The 216 cm^{-1} band is relatively maximized at the 2.54 eV (4880 Å) excitation (Figs. 48 C–E and Figs. 49 A–D). There is a peak at 2.54 eV excitation in the intensity-ratio spectra for films #3~#5. The behavior corresponds to that of the film #1.

For the films #2~#5, the intensity-ratio peaks are much broader than that for the sample #1. The differences of the energy and the shape of the intensity-ratio peak are attributed to the fact that the degrees of disorder are different between the samples. Although the relation between the resonant behavior and the morphology of the sample has not been clarified, it should be stressed that the resonant Raman scattering experiments described here provide a powerful method to investigate the disorder in the crystal.

The concrete picture of the disorder has not been clarified. One of the possible disorder in the polycrystals is the stacking fault of the a–b planes. The results of the X–ray powder diffraction measurement show that the distance of the (002) plane is 5.98 Å for the single crystal and is 5.94 Å for the polycrystalline film #1. Moreover, the (002) peak in the film #1 is accompanied by a satellite peak corresponding to 5.61 Å correlation (Fig. 52). Another information comes from the calculation of the Raman scattering intensity.[32] The calculated intensity of one mono-layer of the crystal shows that the relative Raman intensity of the 216 cm^{-1} band to the 211 cm^{-1} band is larger than that of the non-resonant spectra by the experiment. The calculated ratio is reduced by considering the interaction between the neighboring layers. In other words, the low intensity-ratio of the 216 cm^{-1} band to the 211 cm^{-1} band in the non-resonant Raman spectra of the single crystals is due to the

inter-layer interactions in the rightly stacked layers. The increase of the 216 cm^{-1} band over wide excitation photon energy range in the disordered polycrystals might be due to the disorder in the stacking of the layers.

In Table 9, the peak positions and the peak widths (FWHM) of the 211 cm^{-1} and 216 cm^{-1} bands for the polycrystalline film #1~#3 at various excitation photon energies are shown. The energy position of the 211 cm^{-1} band is regarded as constant within the experimental accuracy. The energy position of the 216 cm^{-1} band shifts about 2 cm^{-1} toward the higher energy side than that of the single crystalline β–$GeSe_2$. The shift of the peak might be due to the residual strain in the film or the stacking fault of the layered-structure. The peak widths for both bands, 211 and 216 cm^{-1} for the polycrystalline films are slightly broader than those for the single crystal shown in Table 6 and 7.

In the Raman spectra of the sample #3 (Figs. 48, C–E), there is a Raman band at about 200 cm^{-1} which is due to α–$GeSe_2$. As the excitation photon energy increases, the intensity ratio of the 200 cm^{-1} band to the 211 cm^{-1} band rapidly increases. The observation will be due to the fact that the energy gap of α–$GeSe_2$ is greater than that of β–$GeSe_2$.

4.3 Amorphous Film

4.3.1 Raman Spectra

Figure 53 shows the absorption spectra of the a–$GeSe_2$ film at 300 K and 20 K. There is no hump structure in the spectra. The energy gap value increases with decreasing temperature.

Figure 54 shows the RT Raman spectra of the a–$GeSe_2$ film by various excitation photon energies, from 2.41 to 2.71 eV. For all spectra, three prominent bands, the A_1 band, the A_1^C band, and the A_G band are observed. Differing from the spectra of c–$GeSe_2$, there is no outstanding change in the spectra by varying the excitation photon energy. The situation is also true for the spectra by much lower excitation

Table 9: Raman peak positions and widths (FWHM) of the polycrystalline β–$GeSe_2$ film #1~#3 at room temperature in the (VV) configuration. The spectral resolution is about 1 cm^{-1} FWHM.

Sample	Excitation energy (eV)	211 cm^{-1} band Position (cm^{-1})	211 cm^{-1} band Width (cm^{-1})	216 cm^{-1} band Position (cm^{-1})	216 cm^{-1} band Width (cm^{-1})	216–211 splitting (cm^{-1})
#1	2.41	211.0	6.4	218.4	6.4	7.4
	2.47	212.0	6.4	219.6	6.6	7.6
	2.50	210.7	6.7	218.5	6.6	7.8
	2.54	211.0	6.7	218.8	6.6	7.8
	2.60	211.8	7.0	219.3	6.6	7.5
	2.71	210.7	7.0	218.0	6.6	7.3
	2.81	211.6	8.0	219.5	6.8	7.9
#2	2.41	211.4	5.2	217.3	4.6	5.9
	2.47	212.0	5.3	218.4	5.7	6.4
	2.50	211.1	5.5	217.7	6.1	6.6
	2.54	210.9	5.6	217.6	5.8	6.7
	2.60	211.5	5.8	218.2	5.6	6.7
	2.71	210.3	5.8	216.7	5.5	6.4
	2.81	211.7	6.5	218.2	5.7	6.5
#3	2.41	211.3	5.1	217.3	7.1	6.0
	2.47	211.9	5.0	218.0	7.1	6.1
	2.50	211.1	5.5	218.2	7.1	7.1
	2.54	211.2	5.5	218.3	7.1	7.1
	2.60	211.4	5.4	218.1	7.1	6.7
	2.71	211.3	5.8	217.6	7.0	6.3
	2.81	211.6	6.4	218.4	6.6	6.8

energy such as 1.17 eV (1.06 μm) [11] or 1.83 eV (6764 Å).[16]

As described in Sec. 2.2.2, the basic building-block in a–$GeSe_2$ is a $GeSe_{4/2}$ tetrahedron similarly to that in the crystal. In the Raman spectra of a–$GeSe_2$ (Fig. 45), there is the A_1 band at about 198 cm^{-1} which will be related to the symmetrical breathing mode of the $GeSe_{4/2}$ tetrahedra. Another Raman band called companion A_1 (A_1^C) band is observed at about 216 cm^{-1} which is characterized by the following two points: 1) It has relatively narrow band-width as compared to the A_1 band; 2) Assuming that the intensity of the A_1 in the Ge_xSe_{1-x} glass increases in proportion to x, that of the A_1^C band increases slowly in small x region and then rapidly as x approaches to 1/3. It has been considered that the A_1^C mode is associated with some cluster of atoms (medium-range structure). Then the problem is what is the structure responsible for the A_1^C band.

4.3.2 Medium-Range Structure

Amorphous $GeSe_2$ can be regarded as the most disordered counterpart of c–$GeSe_2$. The polycrystalline film is an intermediately disordered system between them. From this viewpoint, one may deduce the structure of a–$GeSe_2$ from the Raman scattering observations of the polycrystalline films.

In Table 10, the peak positions and widths of the A_1 and A_1^C bands for a–$GeSe_2$ are compared with those of the 211 cm^{-1} and 216 cm^{-1} bands for the single crystalline β–$GeSe_2$, the polycrystalline β–$GeSe_2$ film #1, and the light-induced crystals (See Sec. 4.4.2). The peak shifts of the 211 cm^{-1} and 216 cm^{-1} bands induced by the disorder are small among the polycrystals and the light-induced crystals. The peak position of the A_1^C band in a–$GeSe_2$ is very close to that of the crystalline 216 cm^{-1} band.

As described in Sec. 4.2.3, for the single crystal and the polycrystalline films, the excitation energy dependence of the intensity ratio I_{216}/I_{211} changes depending on the degree of the disorder in the sample. At the 2.41 eV excitation, the ratio is larger in the spectra of the polycrystalline film than those of the bulk single crystal.

Table 10: Raman peak positions and widths (FWHM) of amorphous $GeSe_2$, single crystalline β–$GeSe_2$, polycrystalline β–$GeSe_2$ film #1, and the light-induced crystals at RT. The spectral resolution is about 1 cm^{-1} FWHM.

	A_1 band* / 211 cm^{-1} band		A_1^C band* / 216 cm^{-1} band		
Excitation energy (eV)	Position (cm^{-1})	Width (cm^{-1})	Position (cm^{-1})	Width (cm^{-1})	216–211 splitting (cm^{-1})
			Amorphous film*		
2.41	198.5	19.1	216.5	10.4	18.0
			Single crystal		
2.41	211.4	5.0	217.3	4.1	5.9
2.71	210.5	5.7	216.6	5.8	6.1
			Polycrystalline film #1		
2.41	211.0	6.4	218.4	6.4	7.4
2.54	211.0	6.7	218.8	6.6	7.8
			Light-induced crystal		
2.54	210.8	8.1	219.0	5.6	8.2

Similar enhancement of the intensity ratio of two bands has already been observed in the 2.41 eV excited spectra of c–$GeSe_2$ prepared by various methods:[42] light-induced crystals from an amorphous film, crystals obtained by thermal annealing of an amorphous film, and crystalline powder prepared by grinding bulk crystals (Fig. 55). It should be noted that, when the crystal size is specially confined and/or the structure becomes more disordered, the intensity ratio of the 216 cm^{-1} band to the 211 cm^{-1} band becomes larger.

In Fig. 56, the intensity ratios of the A_1^C band to the A_1 band ($I_{A_1^C}/I_{A_1}$) for the amorphous film at various excitation photon energies are shown with the ratios I_{216}/I_{211} for the single crystal and the polycrystal. The ratio for amorphous film is regarded as a constant within the experimental accuracy. If the disordered crystals were further damaged and disordered, the peak of the intensity-ratio I_{216}/I_{211} around the resonance-energy would become broad and, finally, the behavior of the ratio I_{216}/I_{211} would come close to that of the ratio $I_{A_1^C}/I_{A_1}$. We imagine that the A_1^C band in a–$GeSe_2$ is related to the 216 cm^{-1} band in heavily disordered micro-crystals, and the A_1 band, to the 211 cm^{-1} band. Since the 216 cm^{-1} band comes from the quasi-localized vibration of the edge-sharing bi-tetrahedra, such bi-tetrahedral structure will be preserved in the amorphous phase.

The energy of the A_1 band (198 cm^{-1}) is lower than that of the 211cm^{-1} band by about 13 cm^{-1}, while the energy-difference between the A_1^C band and the 216 cm^{-1} band is about less than 3 cm^{-1}. The width of the A_1^C band ($\sim$10 cm^{-1} FWHM at RT) is narrower than that of the A_1 band ($\sim$19 cm^{-1}). These observations will be explained as follows. The vibration of the 216 cm^{-1} band is quasi-localized in the edge-sharing bi-tetrahedra. The band will not have much dispersion in the crystal. In the amorphous state, the k–selection rule in the Raman process of the crystalline state is broken. The 216 cm^{-1} band with small dispersion in the crystalline states contributes to the narrow A_1^C band around 216 cm^{-1} in the amorphous states. On the other hand, the vibration of the 211 cm^{-1} band will be extended in the corner-sharing chain and makes a band with large dispersion in the crystal. In the amor-

phous state, this extended vibration of corner-sharing tetrahedra will be distributed in the frequency range lower than 211 cm^{-1} and will contribute to the A_1 band. Although the 216 cm^{-1} vibration is quasi-localized at the edge-sharing $Ge_2Se_{8/2}$ bi-tetrahedra, the completely different environmental structure around bi-tetrahedra from that in the crystalline structure will significantly affect the vibrational energies of the 211 cm^{-1} and 216 cm^{-1} bands. Thus the environmental structure around the bi-tetrahedra in a–$GeSe_2$ should be topologically similar to that in the layered crystalline form. In other words, the a–$GeSe_2$ structure contains the medium-range structure which is topologically similar to the layered c–$GeSe_2$.

Let us compare the topologically layered-crystalline-like medium-range structure model described above with some previous structural models for a–$GeSe_2$. Bridenbaugh et al.[12] have proposed a model for the medium-range structure which is composed of a fragment of topologically crystal-layer-like structure with Se–Se bonds at the cluster edge (outrigger raft cluster). They have assigned the A_1^C band to the breathing vibration of pairs of neighboring corner-shared tetrahedra with the additive Se–Se bonds in the outrigger raft cluster (Fig. 57 A). A weak point of the outrigger raft cluster model is that the calculation of the vibration does not necessarily give the higher energy for the A_1^C band than that for the A_1 band.[13] Although Nemanich et al.[17] proposed the vibration of Ge_6Se_6 ring structure for the A_1^C band (Fig. 57 B), a weak point of the model is that it requires the high existence probability of the ring structure which is never observed in the crystalline structure. Lucovsky et al.[15] and Nemanich et al.[16] have suggested that the Ge_2Se_2 4-atom rings, which is included in the $Ge_2Se_{8/2}$ bi-tetrahedra, are responsible for the A_1^C band (Fig. 57 C). However, as described above, the environmental structure around the $Ge_2Se_{8/2}$ bi-tetrahedra is also important to explain the vibrational energy of the A_1^C and A_1 bands. The existence of layered c–$GeSe_2$ like fragments in a–$GeSe_2$ is also suggested in the work on the light-induced crystallization of a–$GeSe_2$[27,42,56] which will be discussed in Sec. 4.4.3.

When the structure of amorphous states is discussed, the structural model must

explain all the observations on that material, not only the vibrational investigations but also the diffraction measurement and others. Quite recently, Susman et al. have reported the precise neutron diffraction data for amorphous $GeSe_2$.[58] The total correlation function is shown in Fig. 58. They have shown that the first four nearest neighbor in the total correlation function can be ascribed to the Ge–Se correlation in the $GeSe_{4/2}$ tetrahedra (2.385 Å), the Ge–Ge correlation in the edge-sharing $Ge_2Se_{8/2}$ bi-tetrahedra (3.02 Å), the Ge–Ge correlation in the neighboring corner-sharing $GeSe_{4/2}$ tetrahedra (3.57 Å), and the Se–Se correlation (3.93 Å), respectively. These values agree well with the corresponding values for the crystal, 2.355 Å, 3.05 Å, 3.55 Å, and 3.83 Å. The weighted coordination number of the Ge–Ge correlation in the edge-sharing bi-tetrahedra is 0.14 for the glass which is very close to the value $\frac{1}{3} \times \frac{1}{2} \times 1 = 0.17$ for the crystal. The fraction of Ge atoms which contribute to the edge-sharing tetrahedra in the glass is about 40%, which is close to that in the crystal (50%). This result agrees with our structural model of layered-crystalline-like fragment. However, it should be noted that, if the portion of the single crystal whose lateral extent is greater than about 10 Å exists in the glass without any distortion, it will give too many structures in the neutron or X–ray structure factor which is not observed in the experiments.[59] Thus, if there is such large layered-cluster in the glass, it should be heavily distorted.

The molecular dynamics (MD) calculation is also an interesting approach to the investigation of the medium-range order. Vashishta et al.[40] have reported that the fraction of the Ge atoms which contribute to the edge-sharing tetrahedra in the glass is about 32%. In the single crystal, there are many rings with 8 Ge atoms which consist of two chains of the corner-sharing tetrahedra connected by two neighboring edge-sharing bridge bi-tetrahedra. From the layered-crystal-like fragment model, it is expected that the fraction of the existence of the rings with 8 Ge atoms in the glass is close to the fraction in the single crystal. However, the calculated fraction in the glass is considerably lower ($\sim 1/10$) than that in the crystal. The disagreement might be due to too large quenching rate in the preparation of the glass from the

melt in the MD calculation.

As described above, there are many approaches to investigate the medium-range structure: X–ray and neutron diffraction, EXAFS, Raman scattering, molecular dynamics calculation, etc.. Our resonant Raman measurement technique provides a powerful method to the investigation of the medium-range order.

4.4 Light-Induced Crystallization

4.4.1 Temperatures under Illumination

In order to distinguish the photo-process from the thermal-process in the light-induced crystallization, it is important to know the local-temperature at the laser-irradiated region where the light-induced crystallization is taking place. This section describes how one can estimate the temperature of the crystalline $GeSe_2$ samples by the Raman measurement.

Figure 59 shows the temperature dependence of the peak position of the 211 cm^{-1} band in the Raman spectra of single crystalline β–$GeSe_2$. The excitation energy was 2.41 eV (5145 Å). The excitation power was such low level as about 0.5 mW to avoid the heating, though the point-focusing geometry was used. The temperature of the sample was varied by the electric furnace. The peak position of the 211 cm^{-1} band shifts toward the lower energy side as the temperature increases. There is no difference observed in the temperature dependence of the 211 cm^{-1} peak position between the c(a,a)$\bar{c}$ and the c(b,b)$\bar{c}$ configurations. The temperature coefficient is about -0.01 cm^{-1}/K.

Figure 60 shows the temperature dependence of the intensity of the 211 cm^{-1} peak in the Raman spectra by the 2.41 eV (5145 Å) excitation. The temperature dependence of the absorption coefficient below RT suggests that the absorption coefficient increases with increasing temperatures above RT. The decrease of the Raman intensity with increasing temperature is mainly due to this darkening of the sample at high temperatures.

Figure 61 shows the temperature dependence of the peak position of the 211 cm^{-1} band for the bulk single crystal (□), the polycrystalline film #1 (△) and the light-induced crystals (○). The excitation photon energy was 2.41 eV (5145 Å) and the power was about 5 mW. The measurement was made using the point-focusing geometry which makes the sample heating nonnegligible. The peak position shifts to the low energy side with increasing temperature. The temperature coefficients of the peak energy are estimated to be -0.0098 ± 0.0007 cm^{-1}/K for the light-induced crystals, -0.0089 ± 0.0005 cm^{-1}/K for the polycrystalline film #1, and -0.0103 ± 0.0003 cm^{-1}/K for the bulk single crystal. These values agree well with each other within the experimental accuracy.

When laser light is irradiated onto the sample surface, the temperature under the illuminated portion of the sample becomes higher than the environmental temperature by the absorption of the light. The abscissa in Fig. 61 is the environmental temperature. The lower peak positions for the light-induced crystals and the polycrystalline film than for the bulk single crystal at given environmental temperatures shown in Fig. 61 are ascribed to the difference of the degree of this heating effect by the probe light among three crystalline samples.

Figure 62 shows the excitation power dependence of the peak position of the 211 cm^{-1} band for the bulk single crystalline β–$GeSe_2$ (□), the polycrystalline film #1 (△), and the crystals obtained by the light-induced crystallization (○). For all crystals, the heating effect of the sample surfaces by the light absorption is clearly shown by the fact that the peak positions shift toward the low energy side as the excitation power increases.

A large excitation power coefficient of the Raman shift for the light-induced crystals in Fig. 62 is due to the large absorption coefficient and a small heat conduction through the surrounding amorphous state. Extrapolated peak positions at power=zero in the different crystals are very close to each other. Small grain sizes of the light-induced crystals or other properties connected to the imperfection of the light-induced crystals seem not to affect the position of the 211 cm^{-1} band at the

power=zero.

The actual temperature at the irradiated portion of the sample surface in the light-induced crystallization is deduced from the Raman spectra by the following procedures: 1) Measure the excitation power dependence of the peak position of the 211 cm^{-1} band on the light-induced crystals and plot that as in Fig. 62. 2) Estimate the peak position at power=zero by extrapolating the excitation power dependence of the peak position. 3) From the energy difference between the peak position at power=zero and that at the power where the light-induced crystallization occurred, a difference between the temperature at the illuminated portion and the environmental temperature can be estimated by using the temperature coefficient of the peak position. The estimated temperatures are 230 $\sim$ 450 °C for the environmental temperature of 480 K (210 °C), 160 $\sim$ 430 °C for RT (20 °C), 150 $\sim$ 360 °C for 90 K, and 140 $\sim$ 360 °C for 30 K. The minimum light-induced crystallization temperatures are well below the minimum thermal crystallization temperature ($\sim$ 375 °C) for all environmental temperatures.

4.4.2 Raman Spectra of Light-Induced Crystals

As shown in Fig. 55 (II) and (III), the relative Raman intensity of the 216 cm^{-1} band to the 211 cm^{-1} band in the light-induced crystal is comparable with that in the polycrystalline films at the 2.41 eV excitation. The excitation photon energy dependence of the 216 cm^{-1} band in the light-induced crystal is also similar to that in the polycrystalline film, that is, the intensity ratio of the 216 cm^{-1} band to the 211 cm^{-1} band becomes maximized at the energy lower than the maximizing energy 2.71 eV for the single crystal. Figure 63 shows the Raman spectra of the light-induced crystal by 2.54 eV (4880 Å) excitation with various powers. The intensity ratio of the 216 cm^{-1} band to the 211 cm^{-1} band changes with decreasing probe light power, which corresponds to the temperature-tuning of the exciton transition energy through the heating effect by the irradiation. The ratio is maximized at the 2.1 mW excitation in this case.

From these observations, it is concluded that the light-induced crystal has almost the same disorder as the polycrystalline film #1 does. The well thermal annealing produces a crystalline sample like the film #2 in which the intensity ratio of the 216 cm^{-1} band to the 211 cm^{-1} band is maximized at the 2.71 eV excitation (Fig. 50). On the other hand, the light-induced crystallization always produces more disordered crystal in which the ratio maximizing energy is lower than 2.71 eV.

4.4.3 Phase Diagram for Light-Induced Crystallization

In this section, roles of the thermal-excitation and the photo-excitation in the light-induced crystallization process will be discussed. Figure 64 shows the excitation power dependence of the latent period in the light-induced crystallization processes at various environmental temperatures, 30 K, 90 K, 300 K, and 480 K. The excitation photon energy is 2.41 eV (5145 Å). The threshold excitation powers for the crystallization were approximately 6 mW at 480 K, 14 mW at 300 K, 35 mW at 90 K, and 60 mW at 30 K which are shown in Fig. 65. As the environmental temperature decreases, the threshold power increases. By extrapolating the curve to zero threshold power, the environmental temperature seems to approach the minimum thermal crystallization temperature (> 600 K) which will be just above the glass transition temperature.

Figure 66 shows the excitation power dependence of the estimated temperature at the laser illuminated portion of the sample surface. The data points which belongs to the same environmental temperature are distributed over the region of the excitation power higher than the threshold power (Fig. 64) and of the temperature higher than a certain value which is the minimum light-induced crystallization temperature. The minimum light-induced crystallization temperature which is shown by the solid line in Fig. 66 is about 450 K for the excitation power above 10 mW and are well below the minimum thermal crystallization temperature (> 600 K). It should be noted that an extrapolation of the solid line to the excitation power=zero provides the minimum light-induced crystallization temperature of about 600 K which agrees

with the minimum thermal crystallization temperature as well as the curve of the environmental temperature vs. the threshold power does in Fig. 65. Figure 66 is regarded as a kind of phase diagram of the light-induced crystallization which shows the region of the excitation light power and the temperature under illumination where the light-induced crystallization occurs.

The fact that the light-induced crystallization process occurs at the temperature well below the thermal crystallization temperature shows that the light-induced crystallization is not merely induced by thermal process. Thus the excitation of the electrons by light irradiation and their relaxations play an important role in the crystallization. On the other hand, the fact that the minimum-crystallization temperature at the irradiated portion is about 450 K for the excitation light power larger than about 10 mW indicates that the thermal excitation or the back ground temperature rise is also indispensable for the light-induced crystallization.

As described in Sec. 2.3, the light-induced crystallization process can be divided to two types; in the type A, β–$GeSe_2$ grows dominantly and in the type B, α–$GeSe_2$ and β–$GeSe_2$ grow seccessively. Two crystallization types, A and B, appear independently of the excitation power and the type A is much more likely to appear than the type B.[57] The light-induced crystallization is completely different from the pure thermal crystallization where the final state of the crystallization is uniquely determined by the annealing temperature as shown in Fig. 5. The appearance of α–$GeSe_2$ seems to be favorable just above the glass transition temperature. On the other hand, it seems that the crystallization type by the light-induced process is destined by a medium-range or "mesoscopic" structure of the sample. The observation suggests that the β–phase-like medium-range structure is the majority in the amorphous structure. This is consistent with the conclusion from the Raman measurement described in Sec. 4.3.2.

The relaxation of the photo-excited electrons is one of the key processes in the light-induced crystallization. Figures 67 and 68 show the photo-luminescence spectra of the amorphous $GeSe_2$ film and the single crystalline β–$GeSe_2$. The excitation was

2.54 eV (4880 Å). There is a PL band around 1.0 eV for both samples. These large Stokes-shifts ($\sim$ 1 eV) suggest that the electron–phonon interaction is very strong in these material.

The mechanism of the light-induced crystallization process is imagined as follows. By the light irradiation, the Se lone-pair electrons, the electrons at the Se–Se sites, and those at the Ge–Ge sites are excited to form the excitons which are supposed to be localized preferably at the "edge" of the crystalline-like cluster. These excitons have large electron–phonon interactions and may cause the bond breaking and the bond re-construction around the cluster edge. These bond re-constructions make the clusters grow laterally. The neighboring planes of the clusters rotate each other to be settled in the position of crystal. The movement of the cluster may be activated by the thermal-process. Within the latent period, these clusters form the embryos of the crystals which could not be realized by the Raman measurement. Local heating may occur around the cluster edge which accelerate the growth of the embryos to crystalline nuclei. After the volume of a crystallite exceeds a certain value, it begins to be detected by the Raman scattering as the crystal. The empirical growing function $N = N_{max}(1 - \exp(-k(t - t_0)))$ corresponds to a rate equation of the crystallization

$$\frac{dN}{dt} = k(N_{max} - N),$$

where N is the fraction of the crystal in the sample, N_{max} the saturated value of N, k a constant, and t_0 the latent period. There are $\propto N_{max}$ sites which are capable of crystallization at $t = t_0$. These sites may be destined by the initial structure in the sample. The crystallization will proceed at the expense of these crystallization-capable sites.

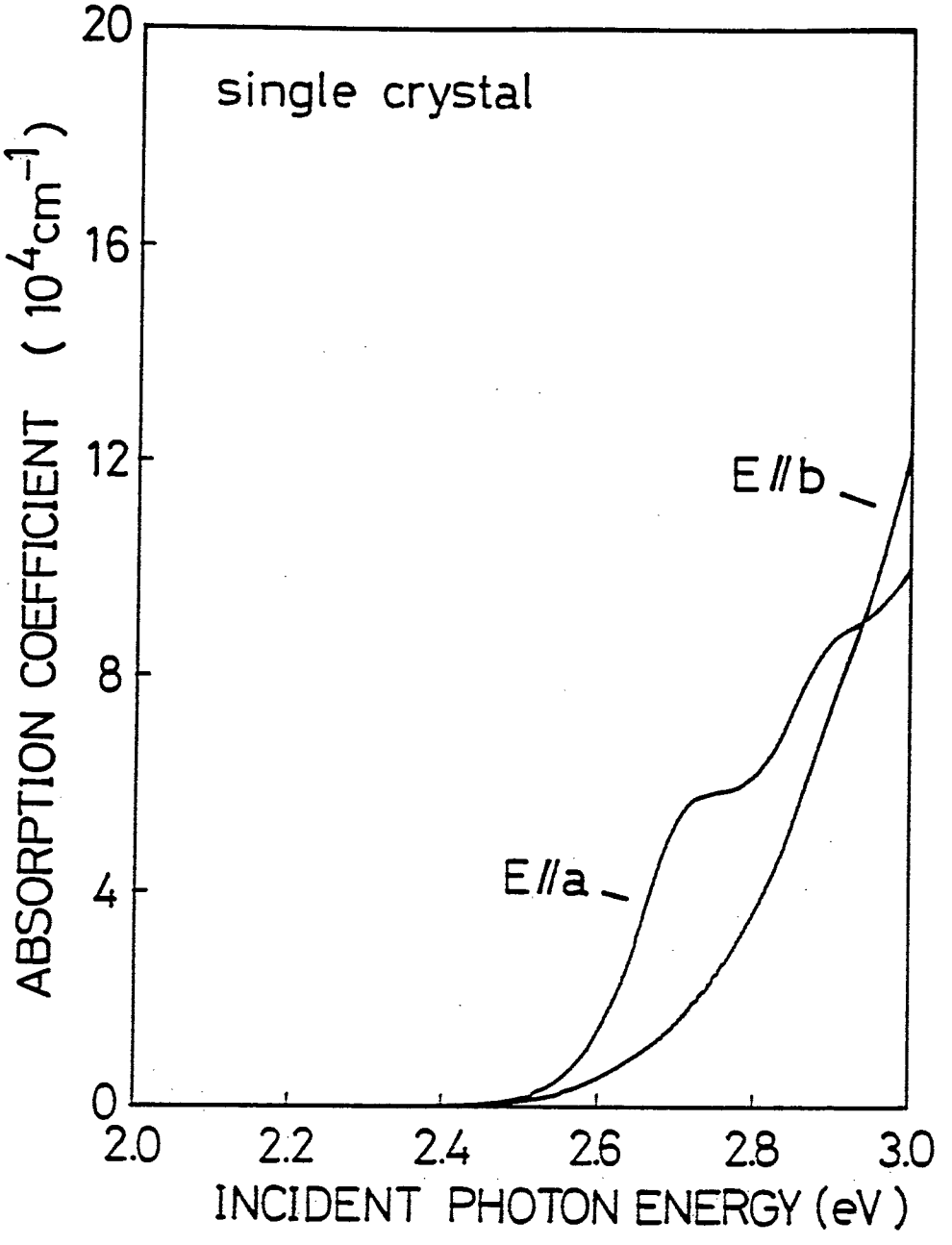

Figure 26: Absorption spectra of bulk single crystalline β–$GeSe_2$ in the $E \parallel a$ and $E \parallel b$ polarizations at RT. An exciton absorption peak is observed at about 2.70 eV in the $E \parallel a$ spectrum.

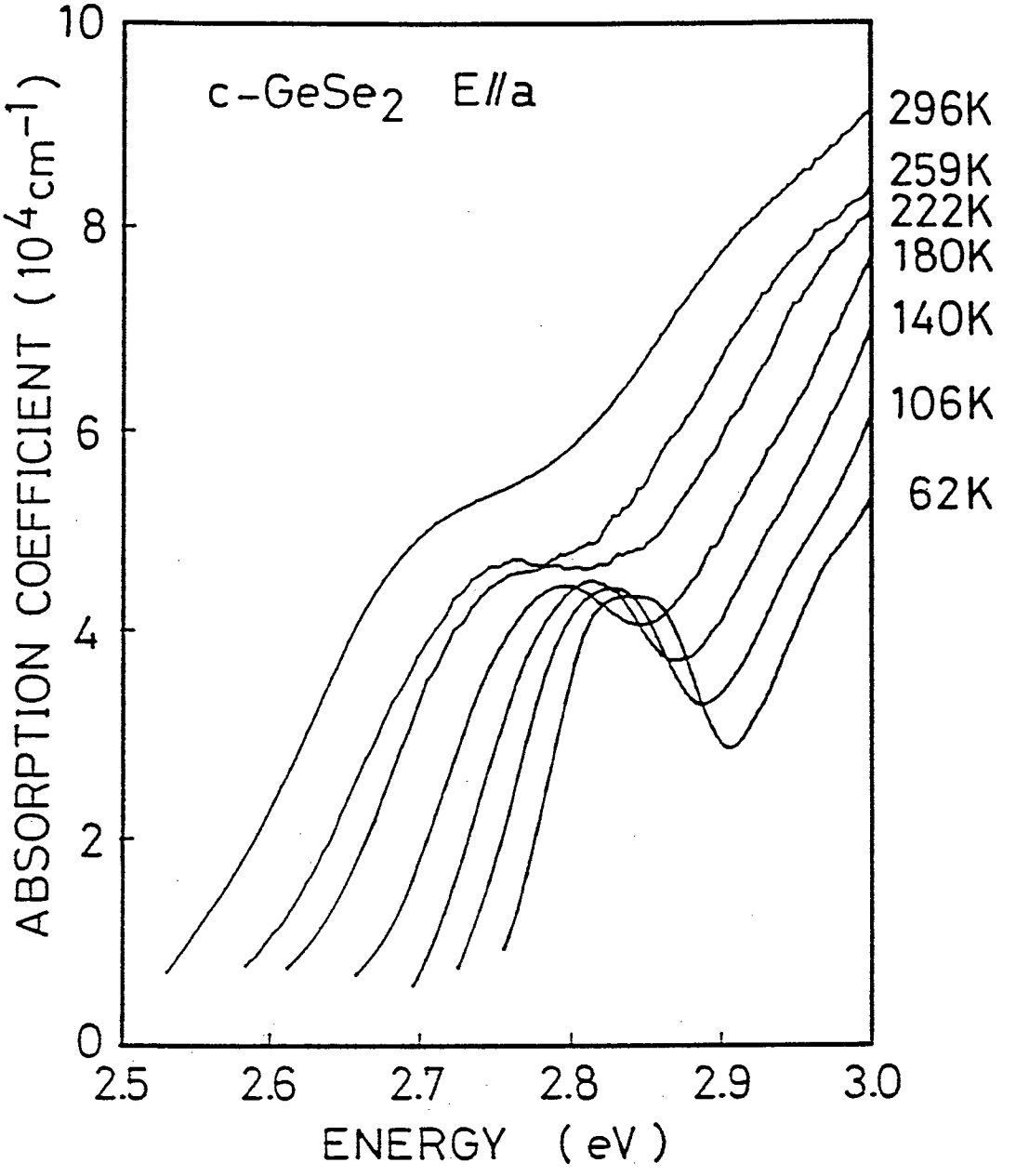

Figure 27: Absorption spectra of bulk single crystalline β–$GeSe_2$ in the $\boldsymbol{E} \parallel \boldsymbol{a}$ polarization at temperatures from 60 K to 300 K. The exciton absorption peak shifts to the higher energy side and becomes sharpened as the temperature decreases.

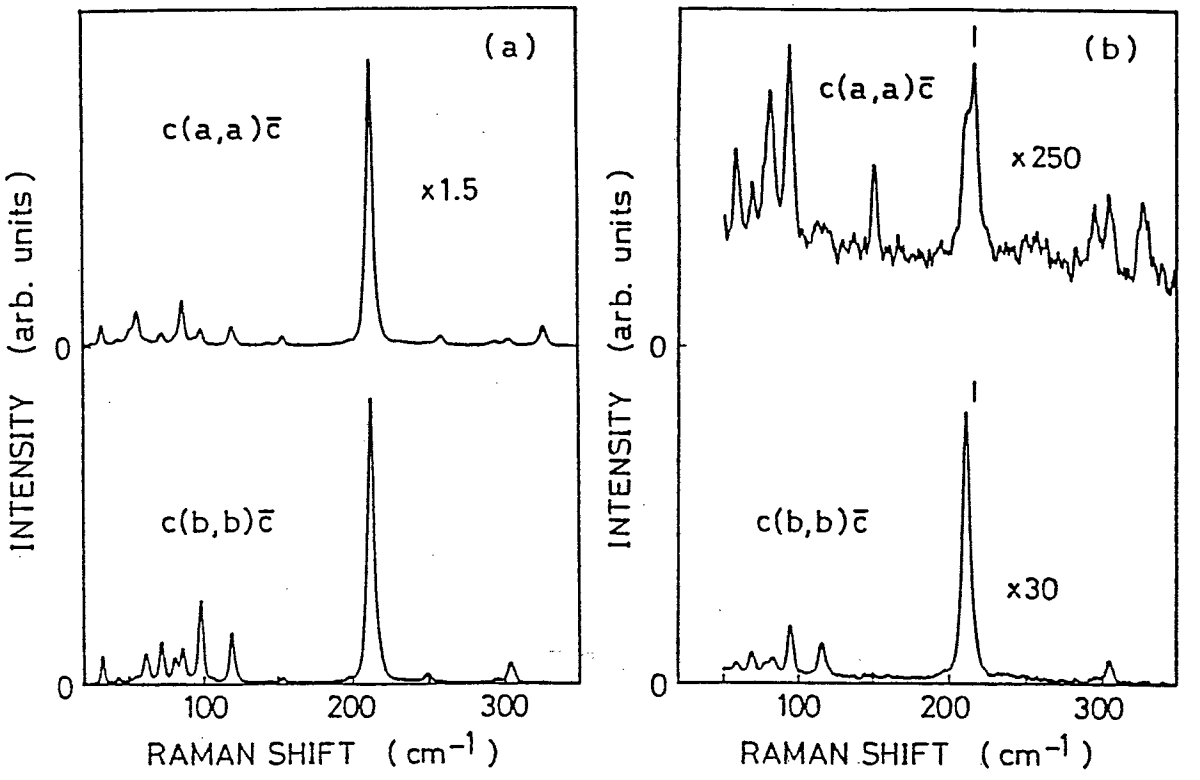

Figure 28: Polarized Raman spectra of single crystalline $GeSe_2$ at RT in the c(a,a)$\bar{c}$ and c(b,b)$\bar{c}$ configurations. The excitation photon energies are a) 2.41 eV (5145 Å) and b) 2.71 eV (4579 Å). A drastic change is observed in the spectra of 2.71 eV excitation in the c(a,a)$\bar{c}$ configuration where the 216 cm^{-1} band becomes stronger than the 211 cm^{-1} band. To avoid the sample heating, the excitation power was less than 10 mW and the line-focusing geometry was used.

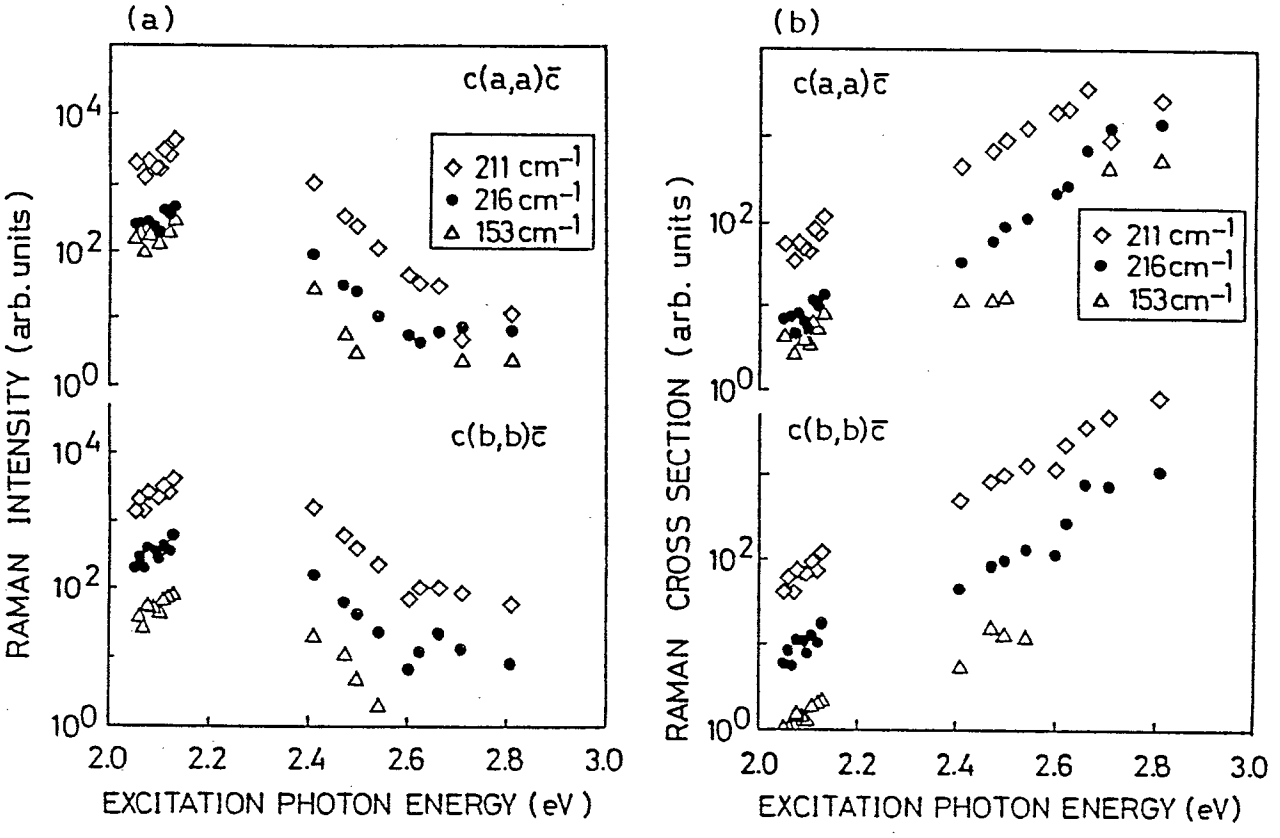

Figure 29: Excitation energy dependence of (a) Raman intensity and (b) Raman cross section for single crystalline β–$GeSe_2$. Three Raman bands at 211 cm^{-1}, 216 cm^{-1}, and 153 cm^{-1} are of interest. At 2.71 eV excitation in the c(a,a)$\bar{c}$ configuration, the 216 cm^{-1} band is stronger than the 211 cm^{-1} band.

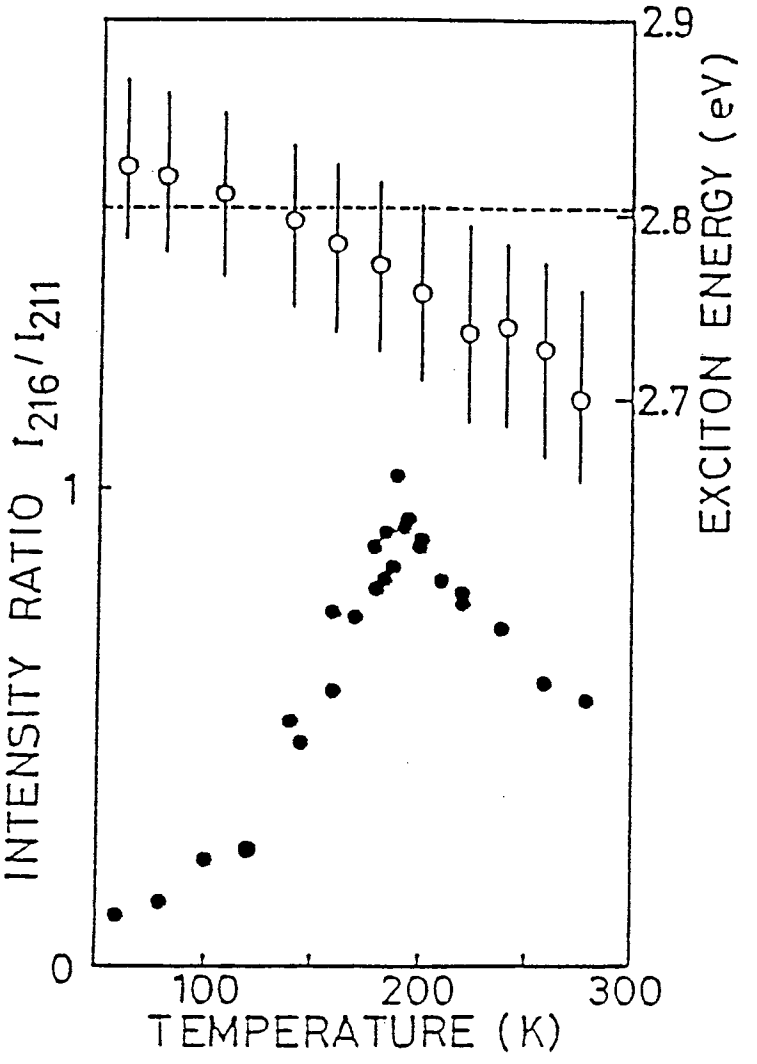

Figure 30: Upper half: Temperature dependence of the exciton transition energy for single crystalline β–$GeSe_2$. Open circles show the exciton transition energies, and the exciton band-widths (FWHM) are shown by vertical bars. Lower half: Raman intensity ratio I_{216}/I_{211} in the c(a,a)$\bar{c}$ configuration vs. temperature. Excitation energy is 2.81 eV (4416 Å), which is shown by a broken line in the upper part.

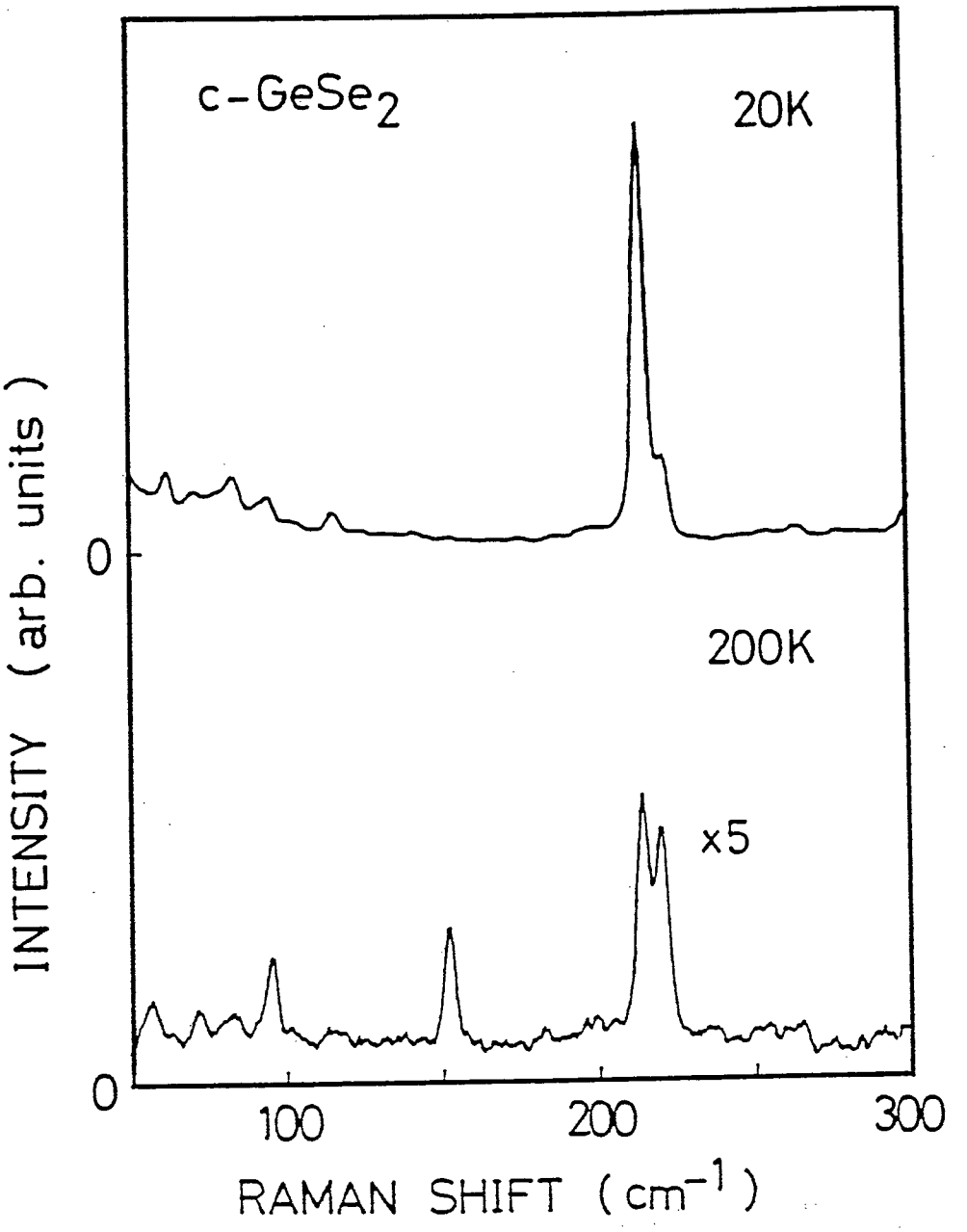

Figure 31: Low temperature Raman spectra for single crystalline β–$GeSe_2$ by 2.81 eV (4416 Å) excitation in the c(a,a)$\bar{c}$ configuration. The relative intensity of the 216 cm^{-1} band to the 211 cm^{-1} band is much larger in the spectrum at 200 K than that at 20 K.

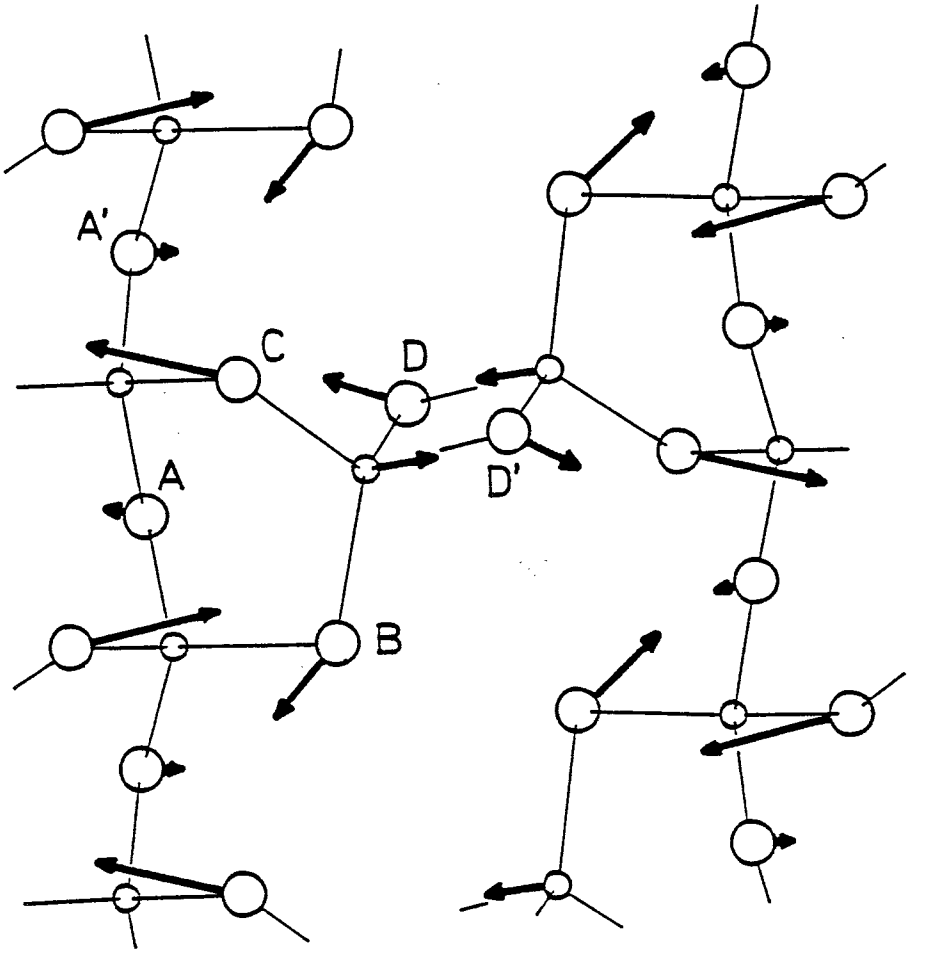

Figure 32: Schematic illustration of the 216 cm^{-1} vibration in β–$GeSe_2$. Vibrational amplitude of Se atoms in edge-sharing tetrahedra (B,C,D) is much greater than that of Se atom in corner-sharing tetrahedra (A) (From Ref. 32).

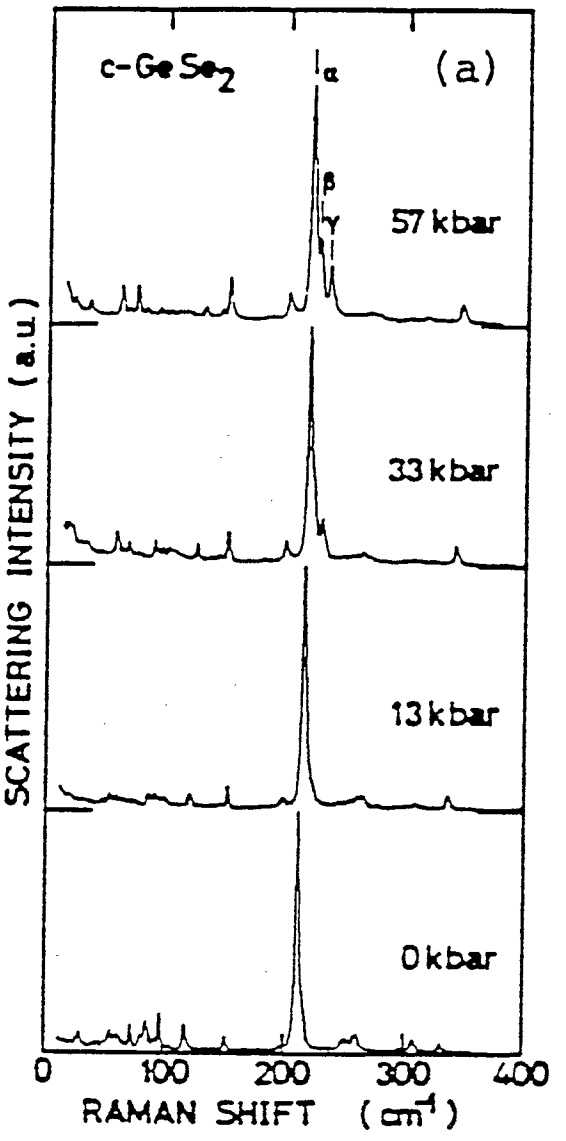

Figure 33: High pressure Raman spectra of β–$GeSe_2$. At 33 kbar, an extra band γ is clearly observed at just above the 211 cm^{-1} band (α) (From Ref. 54).

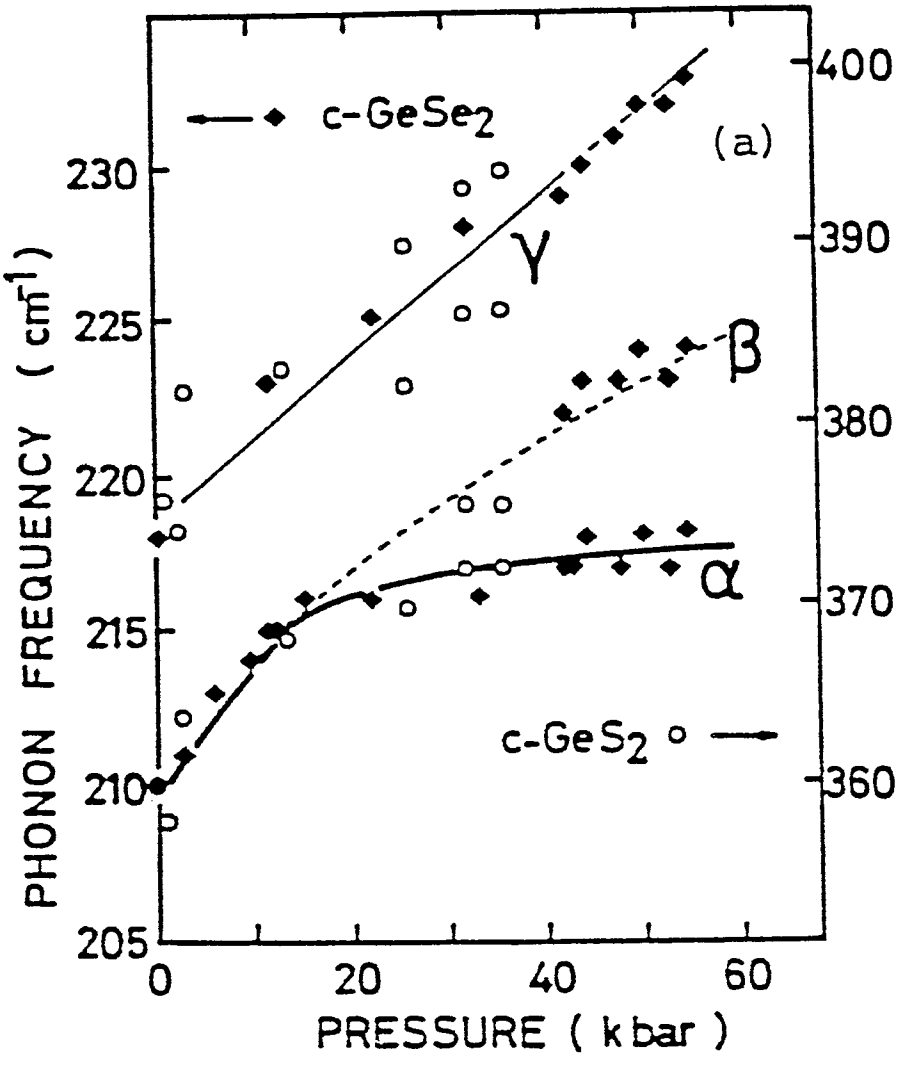

Figure 34: Pressure dependence of Raman peak positions of β–$GeSe_2$. The notations α, β, and γ correspond to those in Fig. 33 (From Ref. 54).

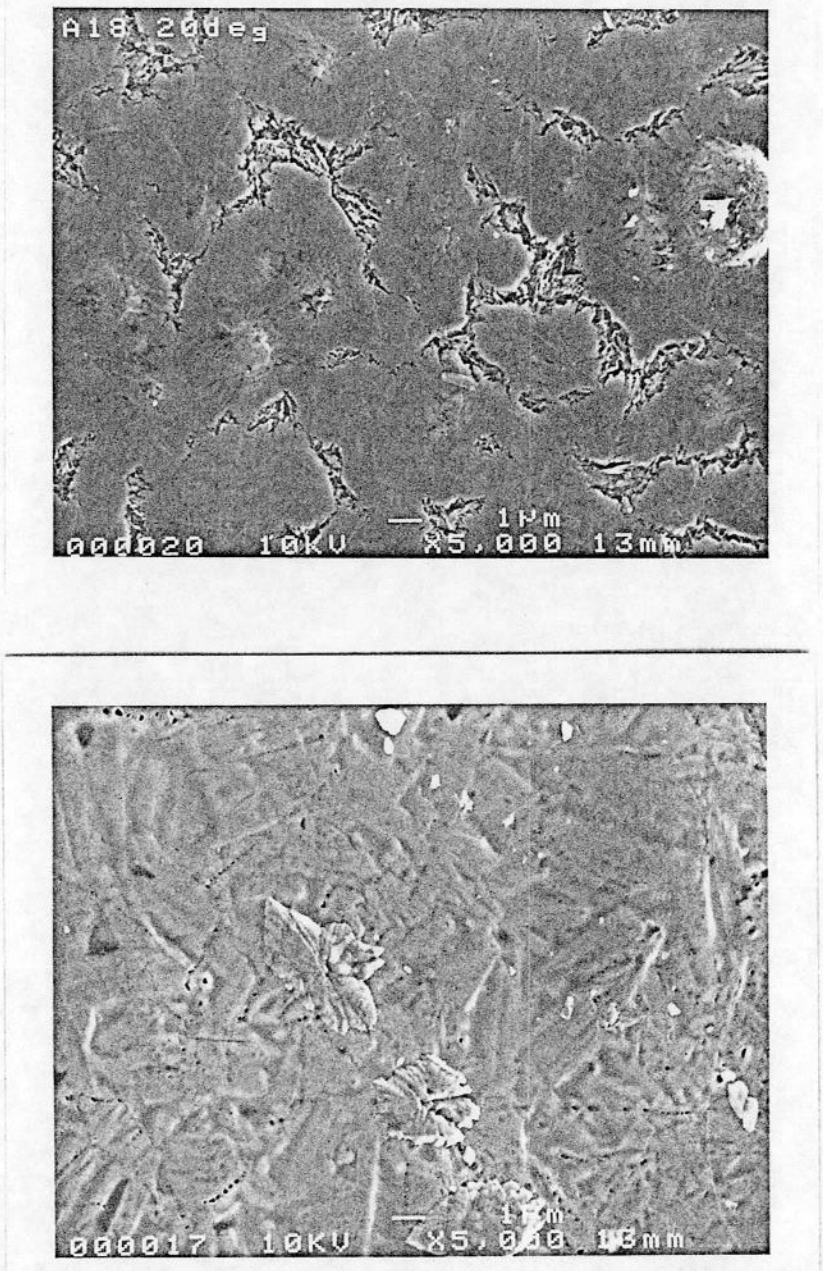

Figure 35: Upper: Vacuum-evaporated film annealed at 425 °C for 18 hours (sample #1) seen by SEM (× 5000). The thickness of the as-deposited film was about 6000Å. Lower: Vacuum-evaporated film annealed at 435 °C for 18 hours (sample #2, × 5000). The thickness of the as-deposited film was about 3μm. For both films, the small platlet-structure is embedded in the flat island region.

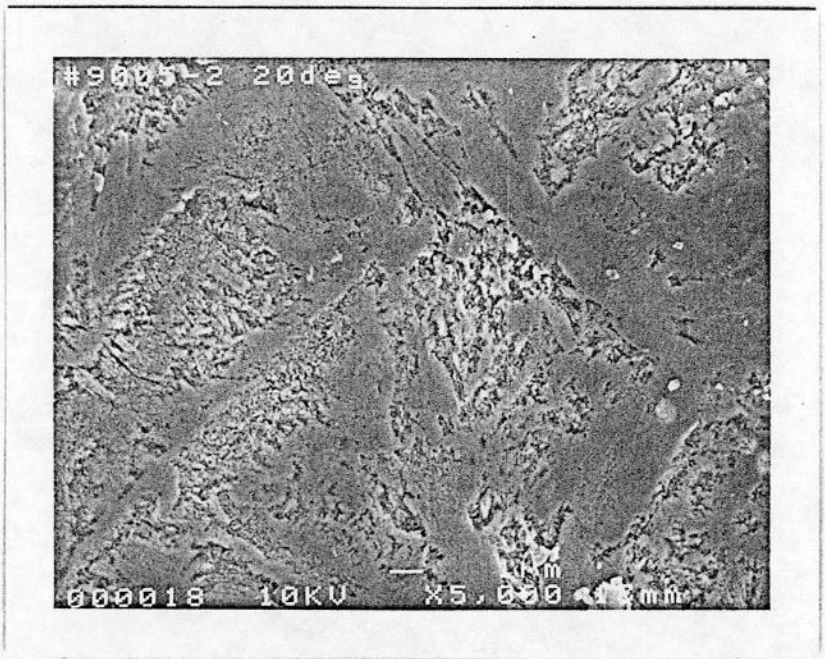

Figure 36: Vacuum-evaporated film annealed at 460 °C for 90 minutes (sample #3) seen by SEM (× 5000). The thickness of the as-deposited film was about 3 μm. In the flat island region, the small platlet-structure is embedded.

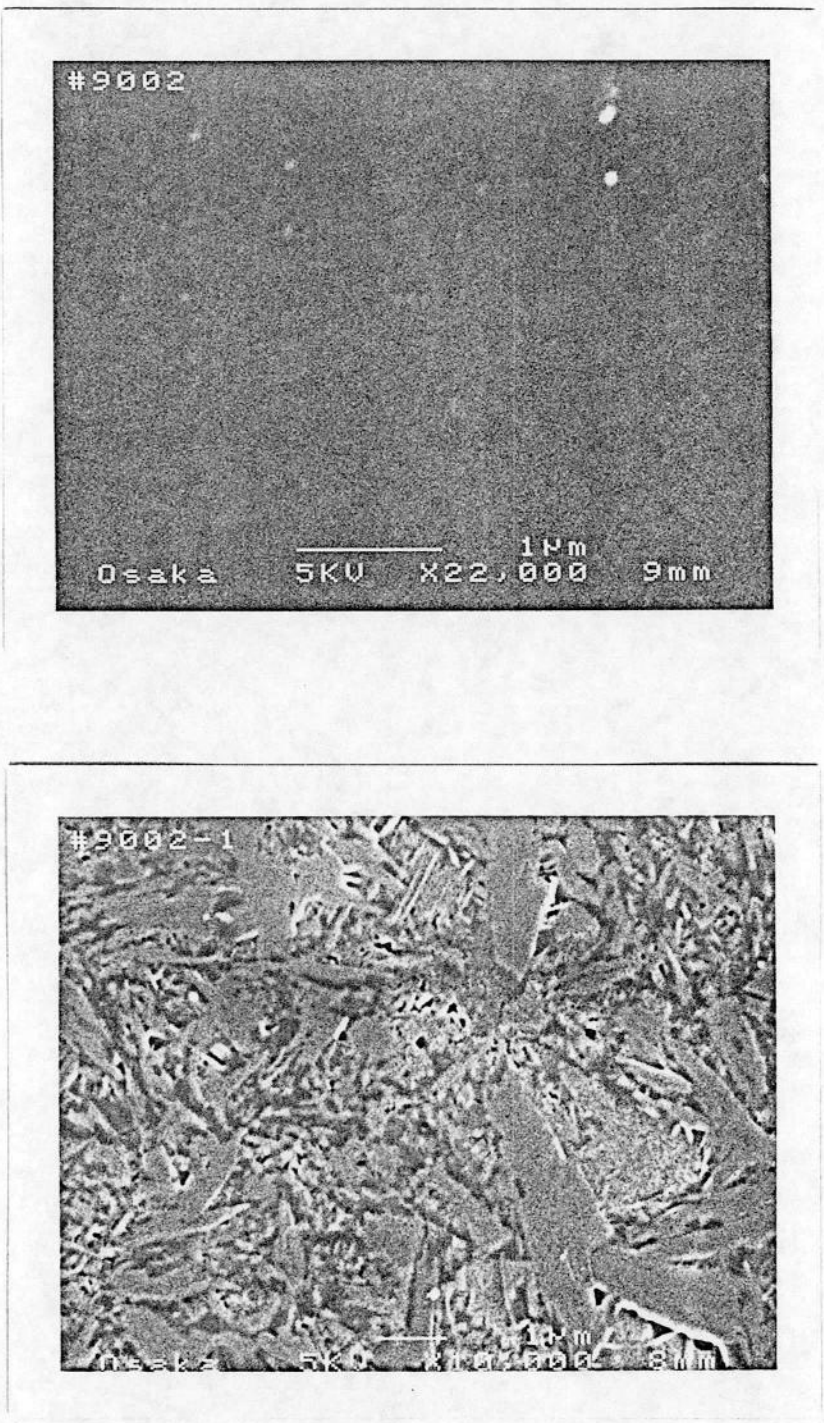

Figure 37: Vacuum-evaporated film of 6000 Å thickness (sample #4) seen by SEM. Upper: as-deposited film (× 22000). The surface is flat and featureless. Lower: annealed at 425 °C for 18 hours (× 10000). In the flat island region, the small platlet-structure is embedded.

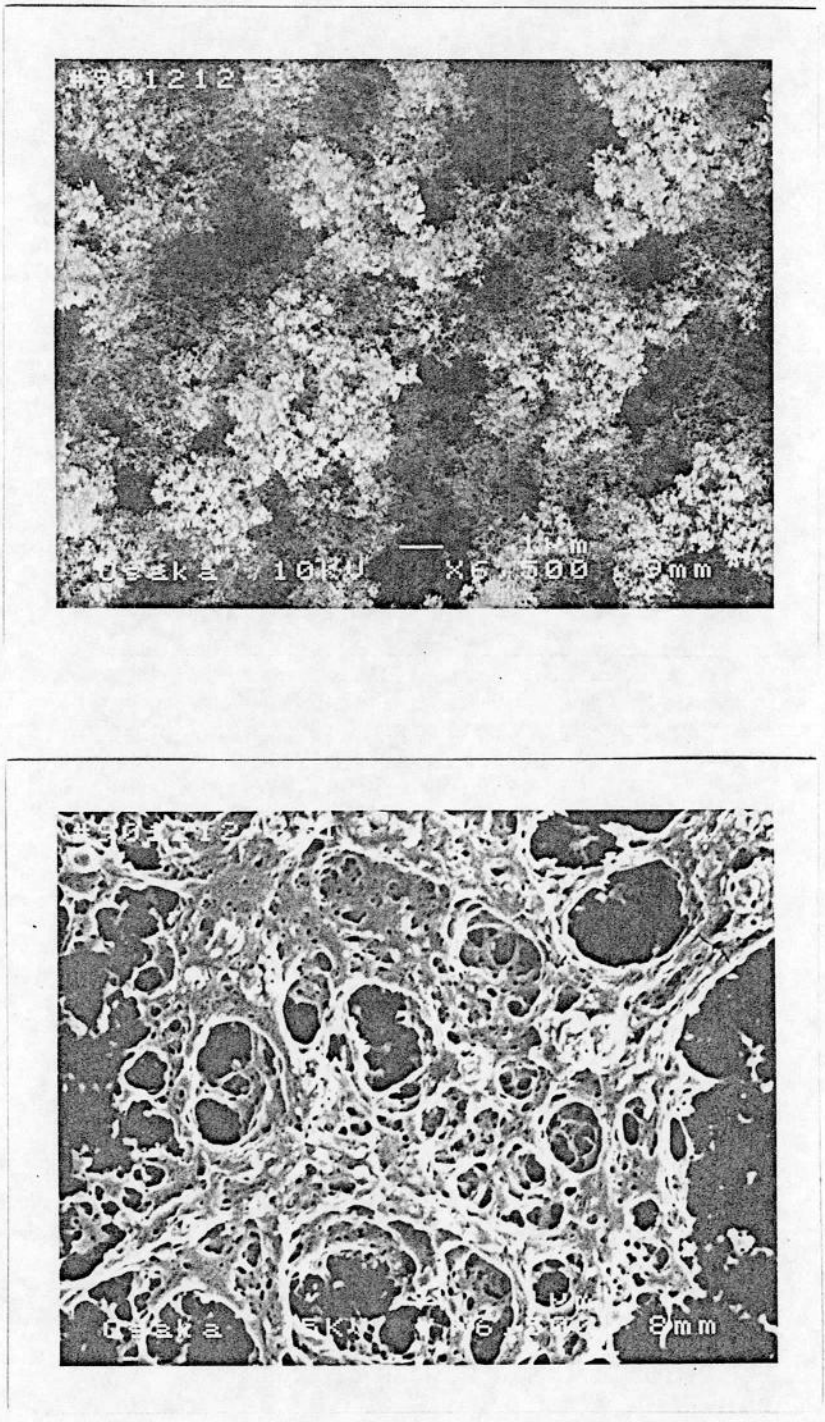

Figure 38: Gas-evaporated film in 2 Torr Ar gas (sample #5) seen by SEM. Upper: as-deposited film (cotton-candy-like, × 6500). Lower: annealed at 421 °C for 18 hours (glue-like, × 6500).

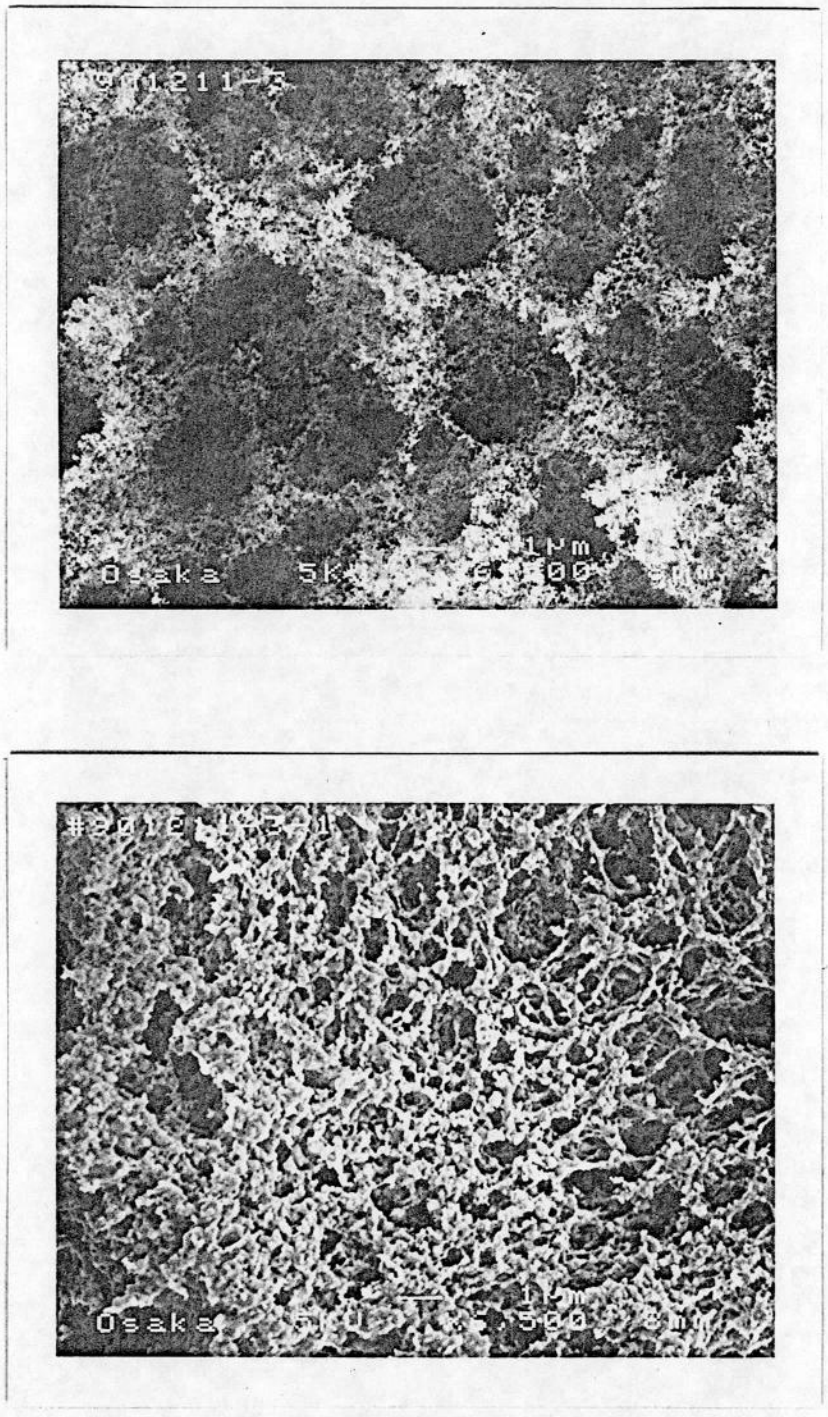

Figure 39: Gas-evaporated film in 1.2 Torr Ar gas (sample #6) seen by SEM. Upper: as-deposited film (cotton-candy like, × 6500). Lower: annealed at 423 °C for 18 hours (coral-like, × 6500).

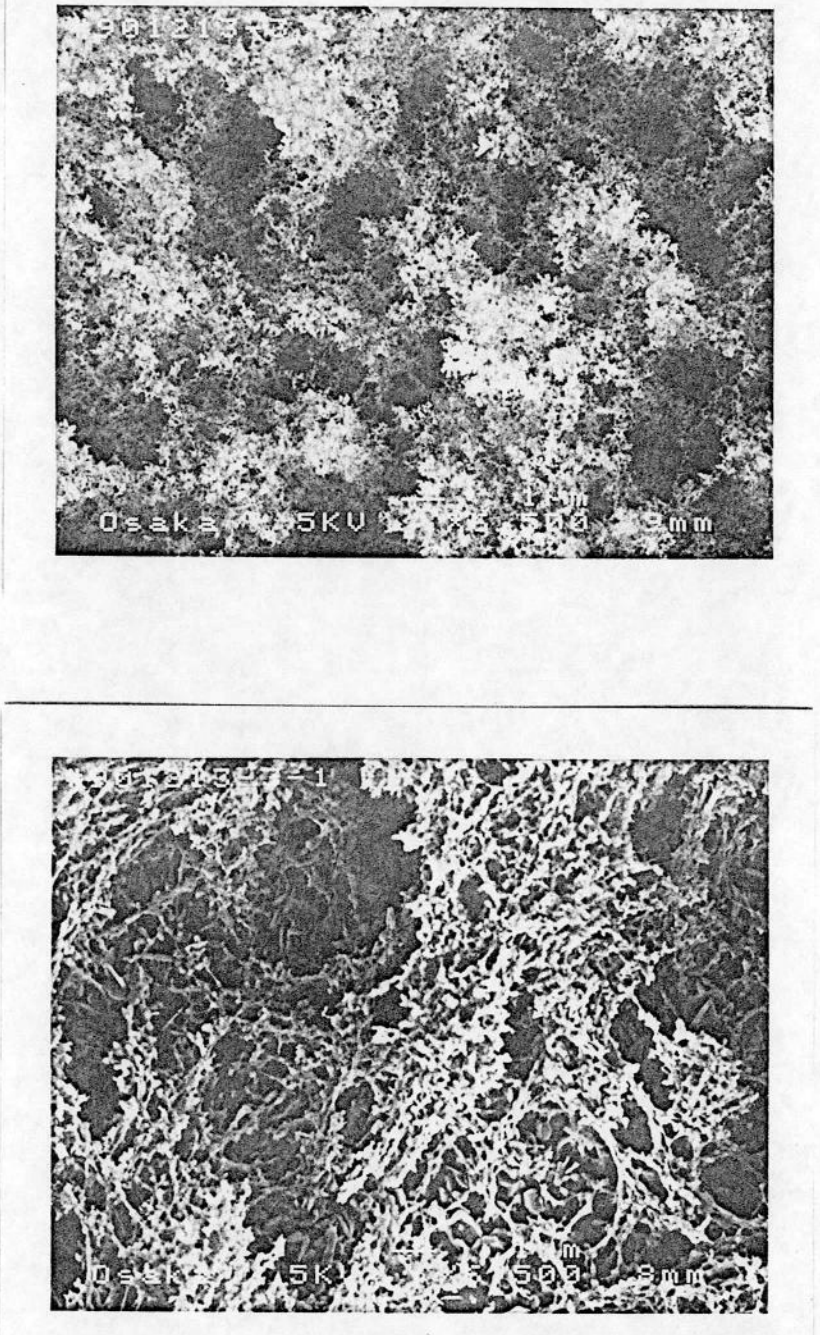

Figure 40: Gas-evaporated film in 0.45 Torr Ar gas (sample #7) seen by SEM. Upper: as-deposited film (cotton-candy like, × 6500). Lower: annealed at 423 °C for 18 hours (coral-like, × 6500).

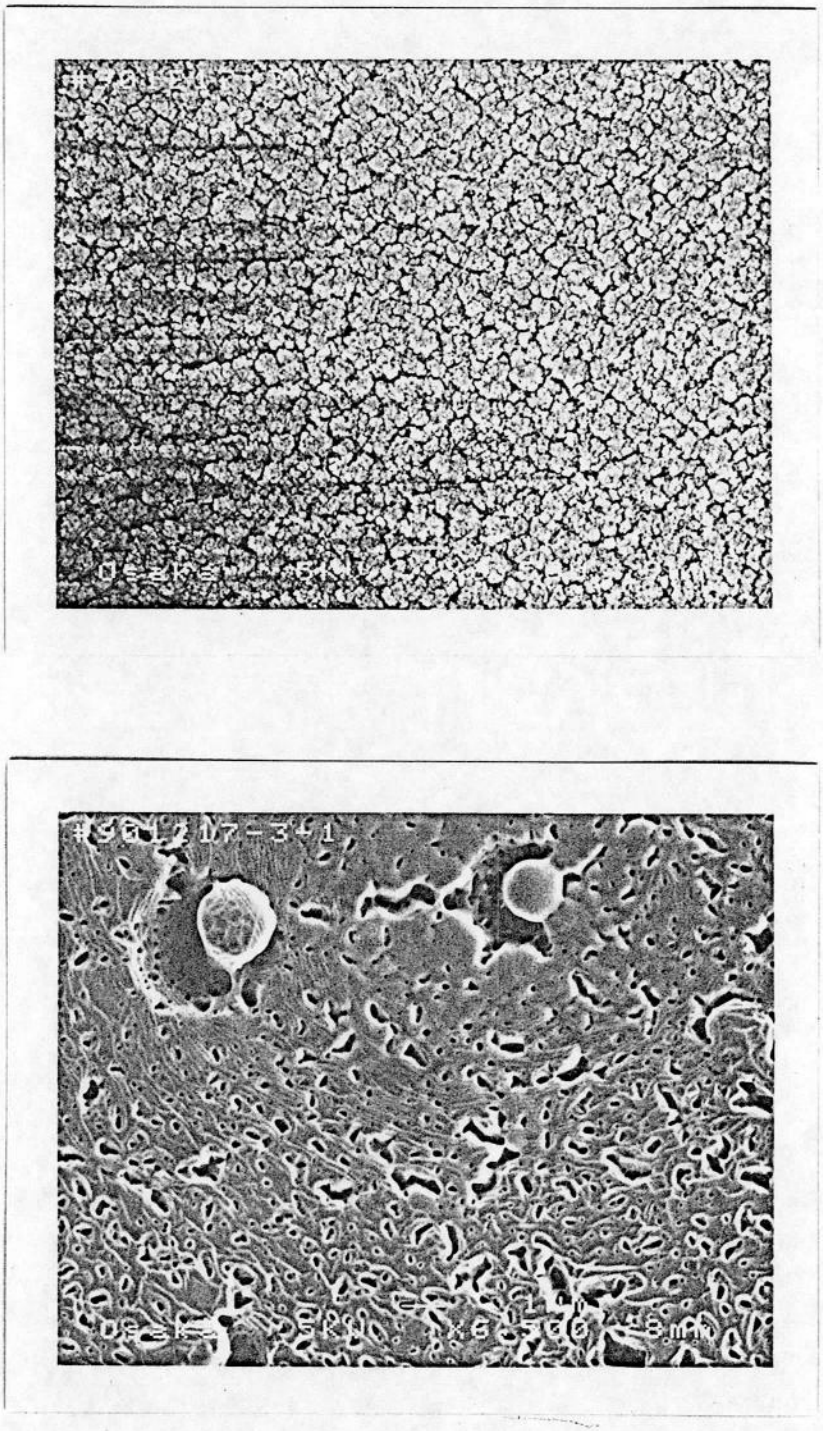

Figure 41: Gas-evaporated film in 0.1 Torr Ar gas (sample #8) seen by SEM. Upper: as-deposited film (cloud-like, × 6500). Lower: annealed at 424 °C for 18 hours (glassy-lava-like, × 6500).

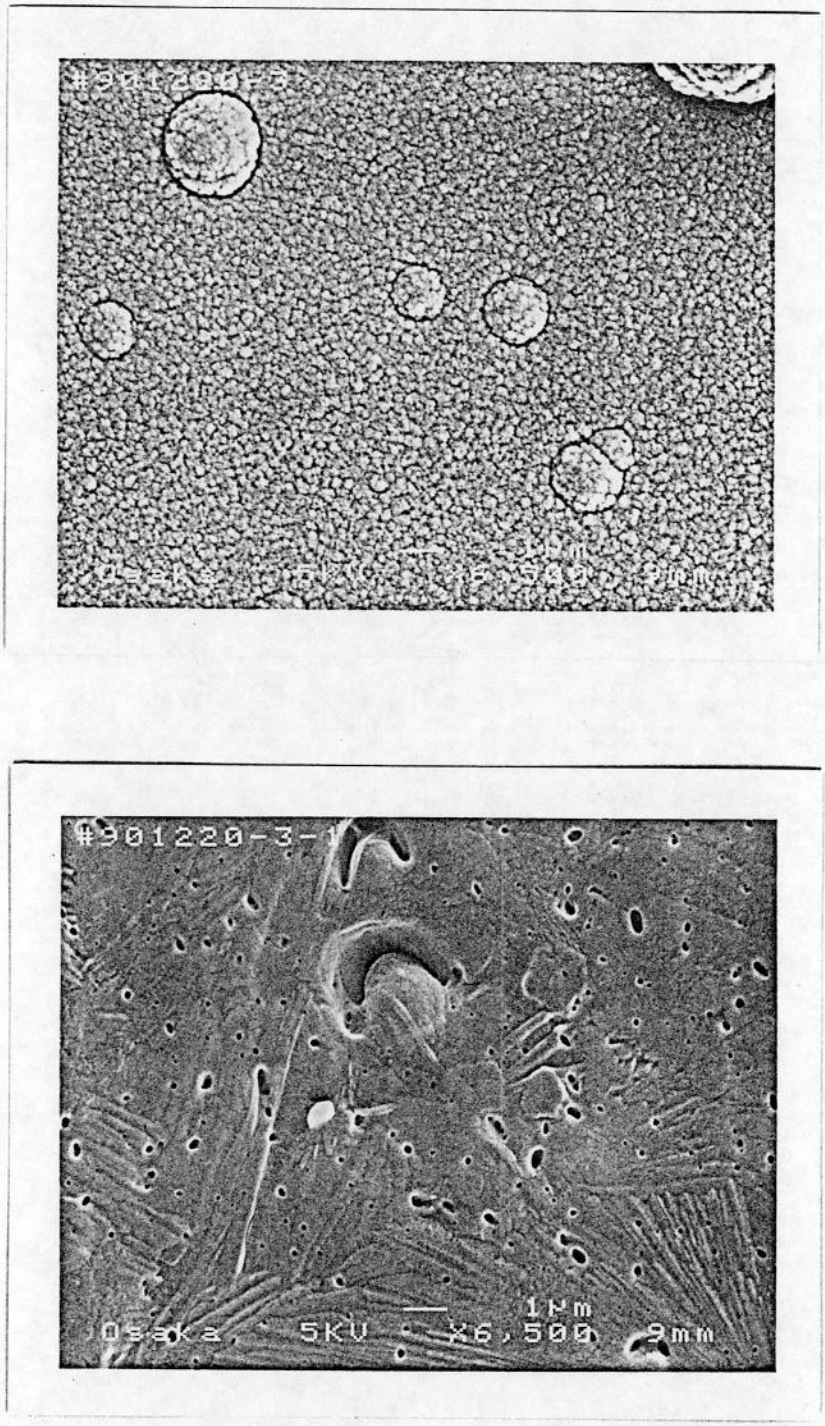

Figure 42: Gas-evaporated film in 0.08 Torr Ar gas (sample #9) seen by SEM. Upper: as-deposited film (cloud-like, × 6500). Lower: annealed at 424 °C for 18 hours (glassy-lava-like, × 6500). In the glassy-lava like region, the needle-like structure is embedded.

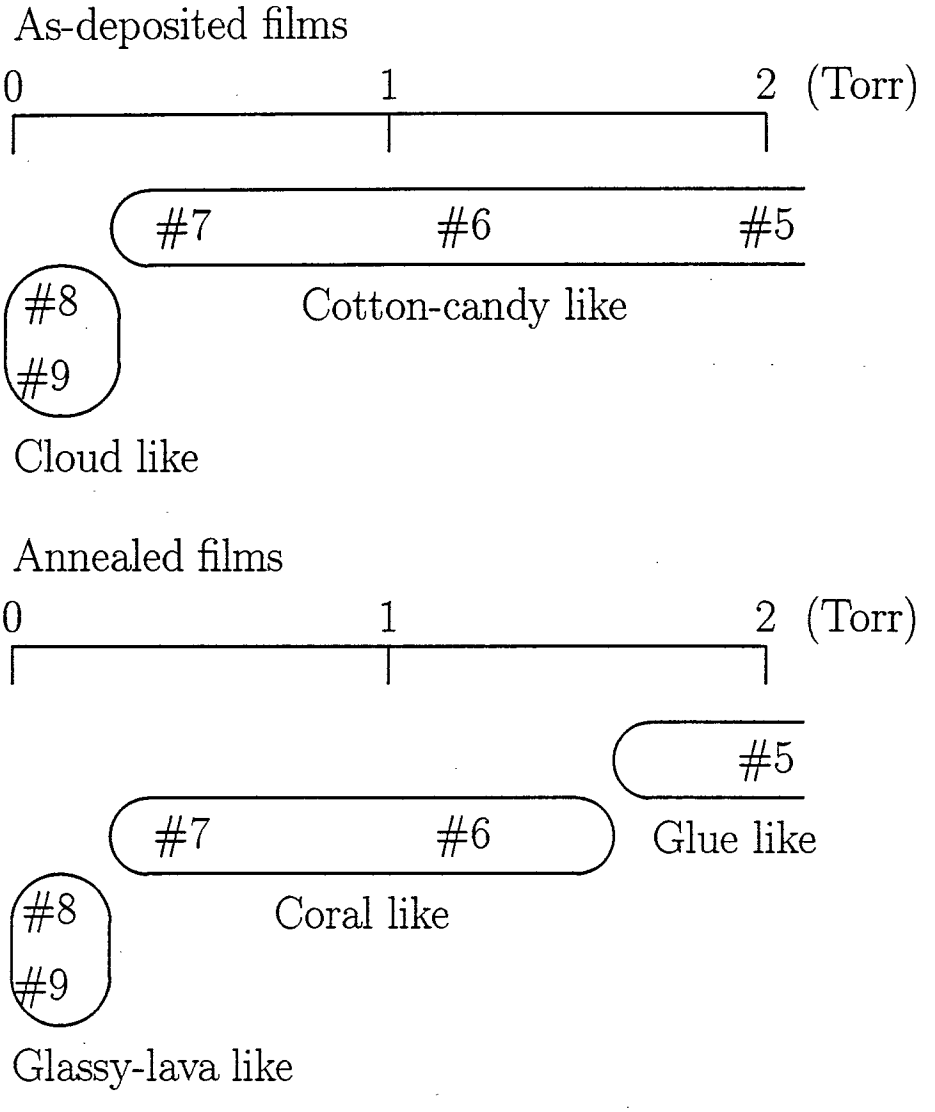

Figure 43: A rough relation between the pressure of Ar gas at the evaporation and the morphology of the evaporated films.

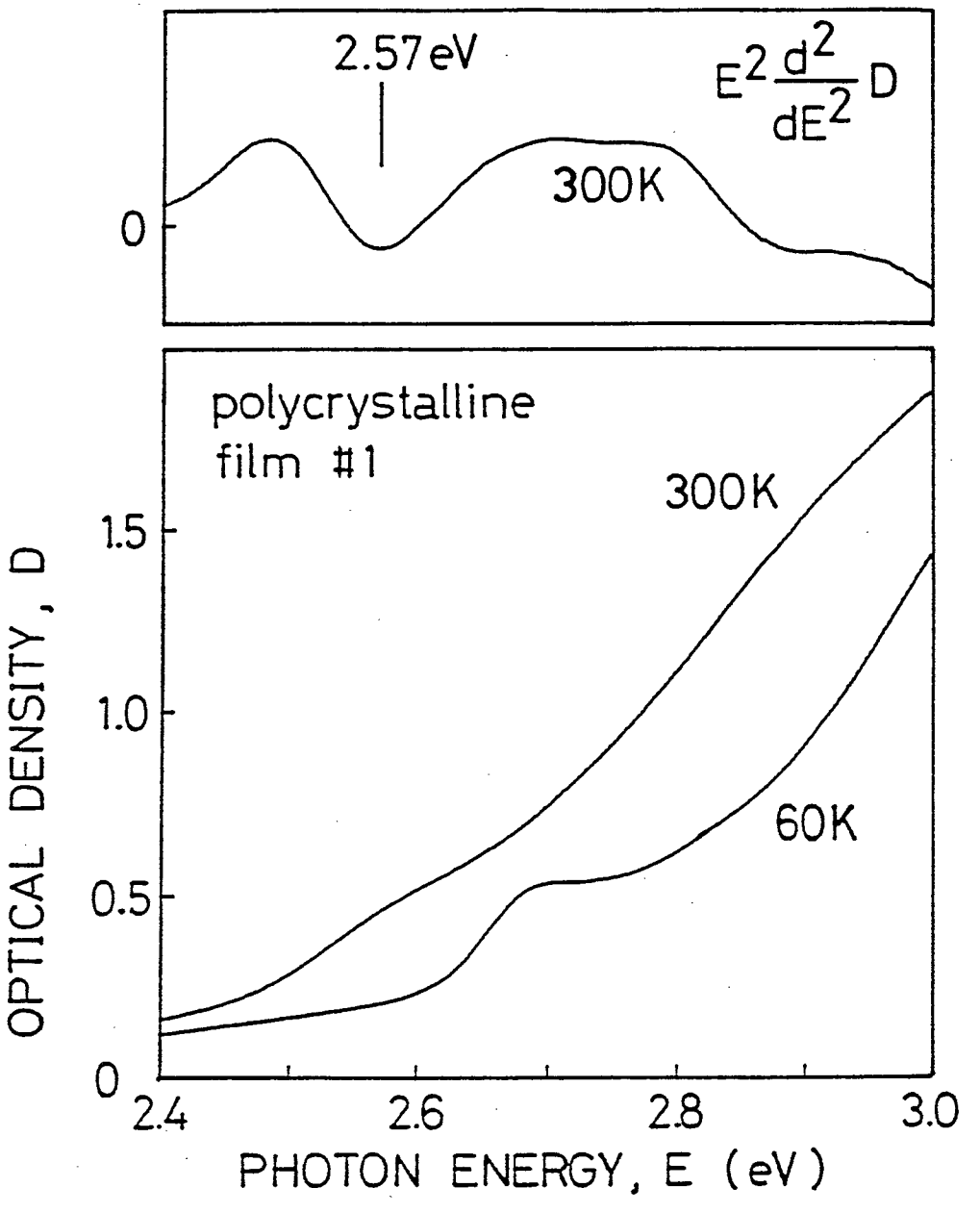

Figure 44: Temperature dependence of optical density for polycrystalline β–$GeSe_2$ film #1. The uppermost curve is the second-energy-derivative of the optical density curve at 300 K showing that the exciton energy is around 2.57 eV.

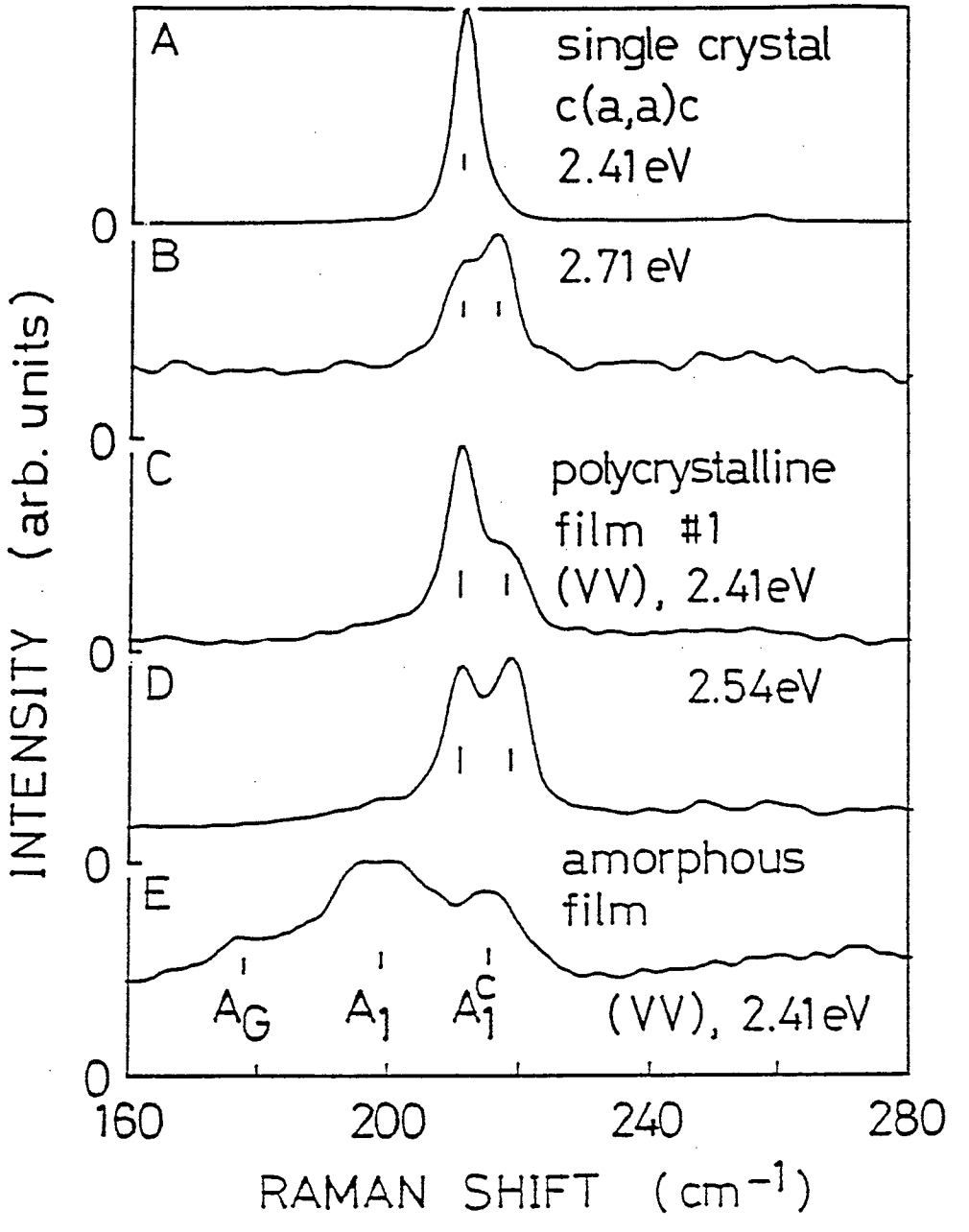

Figure 45: Raman spectra of $GeSe_2$ for (A) the single crystal in c(a,a)$\bar{c}$ by 2.41 eV excitation, (B) the single crystal in c(a,a)$\bar{c}$ by 2.71 eV excitation, (C) the polycrystalline film #1 in (VV) by 2.41 eV excitation, (D) the polycrystalline film #1 in (VV) by 2.54 eV excitation, and (E) the amorphous film in (VV) by 2.41 eV excitation. Vertical bars in A–D indicate the 211 cm^{-1} band and the 216 cm^{-1} band. The crystalline 216 cm^{-1} band is located near the amorphous A_1^C band. To avoid the sample heating, the excitation power was less than 10 mW and the line-focusing geometry was used.

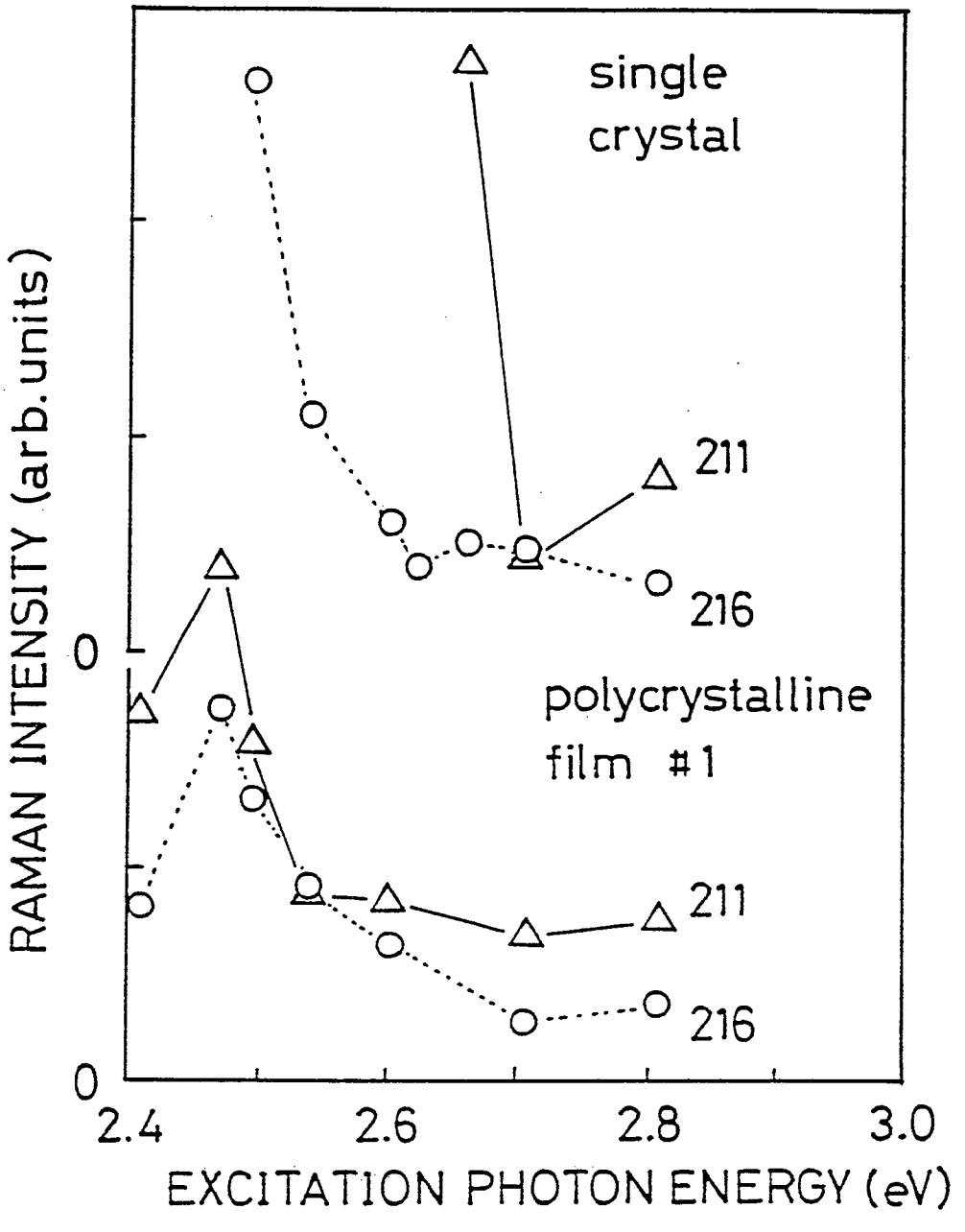

Figure 46: Raman scattering intensity of the 211 cm^{-1} band (△) and the 216 cm^{-1} band (○) at RT for the single crystalline β–$GeSe_2$ (upper half) and the polycrystalline film #1 (lower half). For both crystals, the 216 cm^{-1} band increases at the expense of the 211 cm^{-1} band.

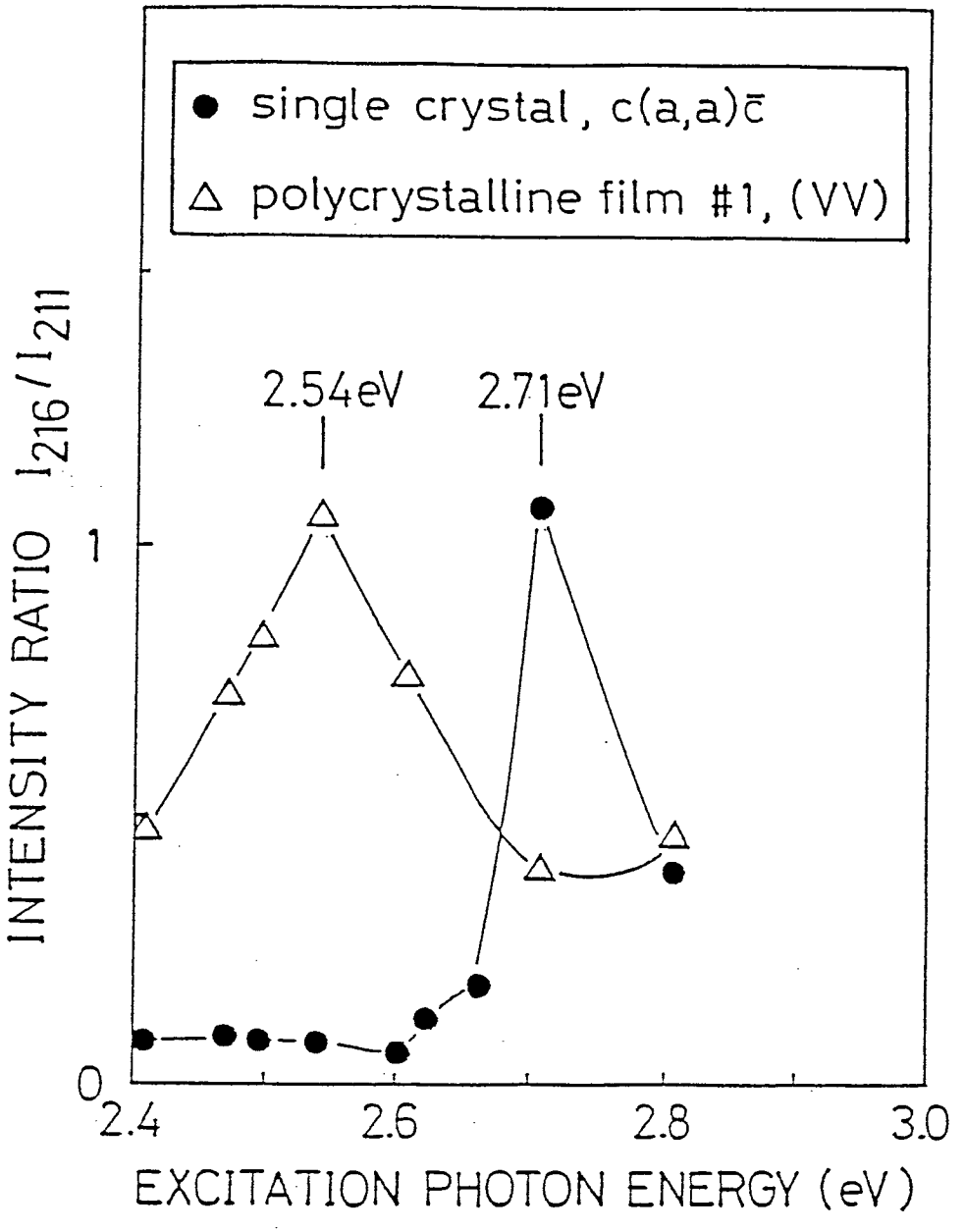

Figure 47: Excitation energy dependence of Raman intensity ratio I_{216}/I_{211} at RT for single crystalline and polycrystalline β–$GeSe_2$. Lines are guides to the eyes. The peak position for the polycrystalline film is lower than that for the single crystal.

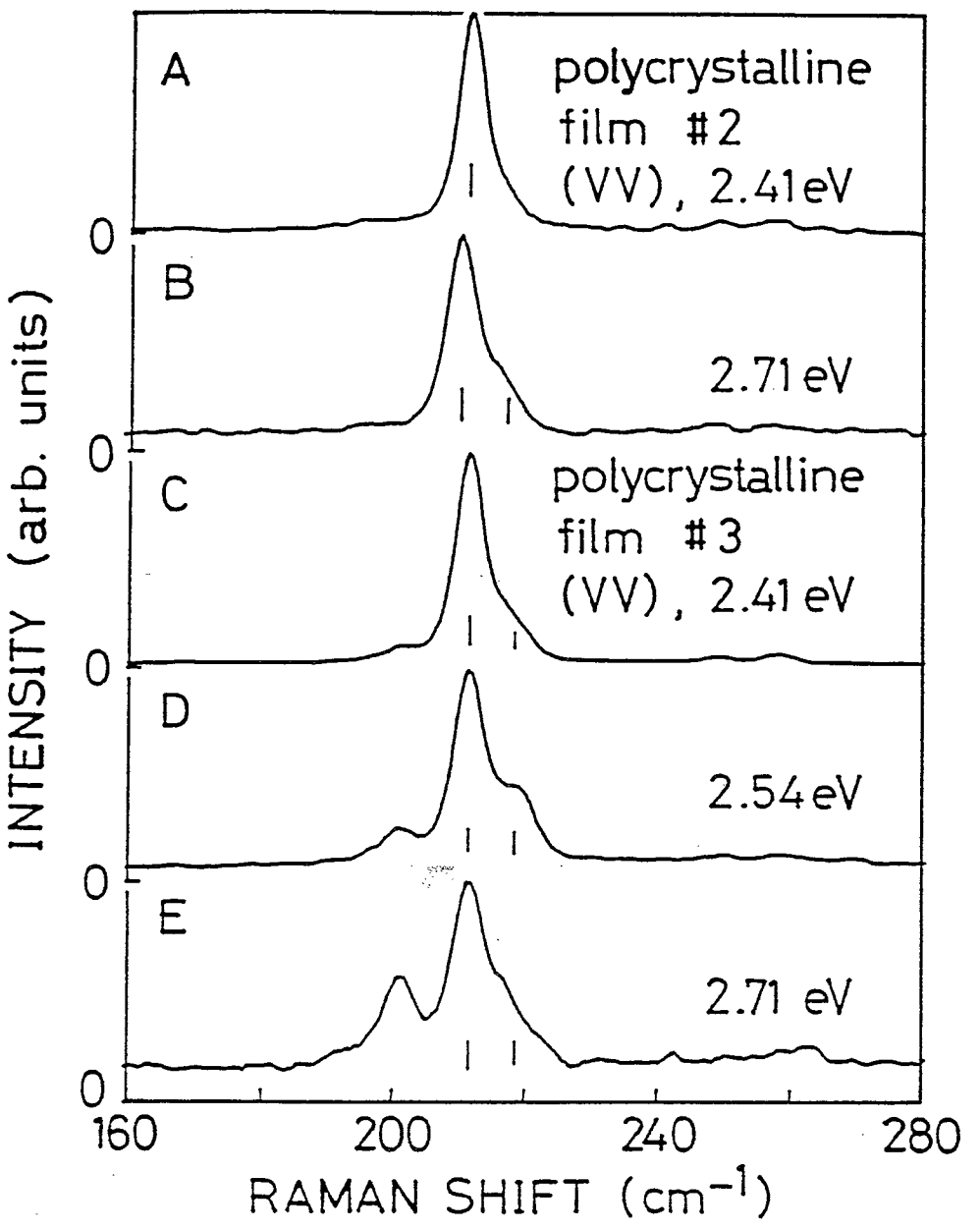

Figure 48: Raman spectra of $GeSe_2$ for (A) the polycrystalline film #2 in (VV) by 2.41 eV excitation, (B) #2 by 2.71 eV excitation, (C) the polycrystalline film #3 in (VV) by 2.41 eV excitation, (D) #3 by 2.54 eV excitation, and (E) #3 by 2.71 eV excitation. Vertical bars indicate the 211 cm^{-1} bands and the 216 cm^{-1} bands. In (E), a peak at about 200 cm^{-1} appears which is due to α–$GeSe_2$. To avoid the sample heating, the excitation power was less than 10 mW and the line-focusing geometry was used.

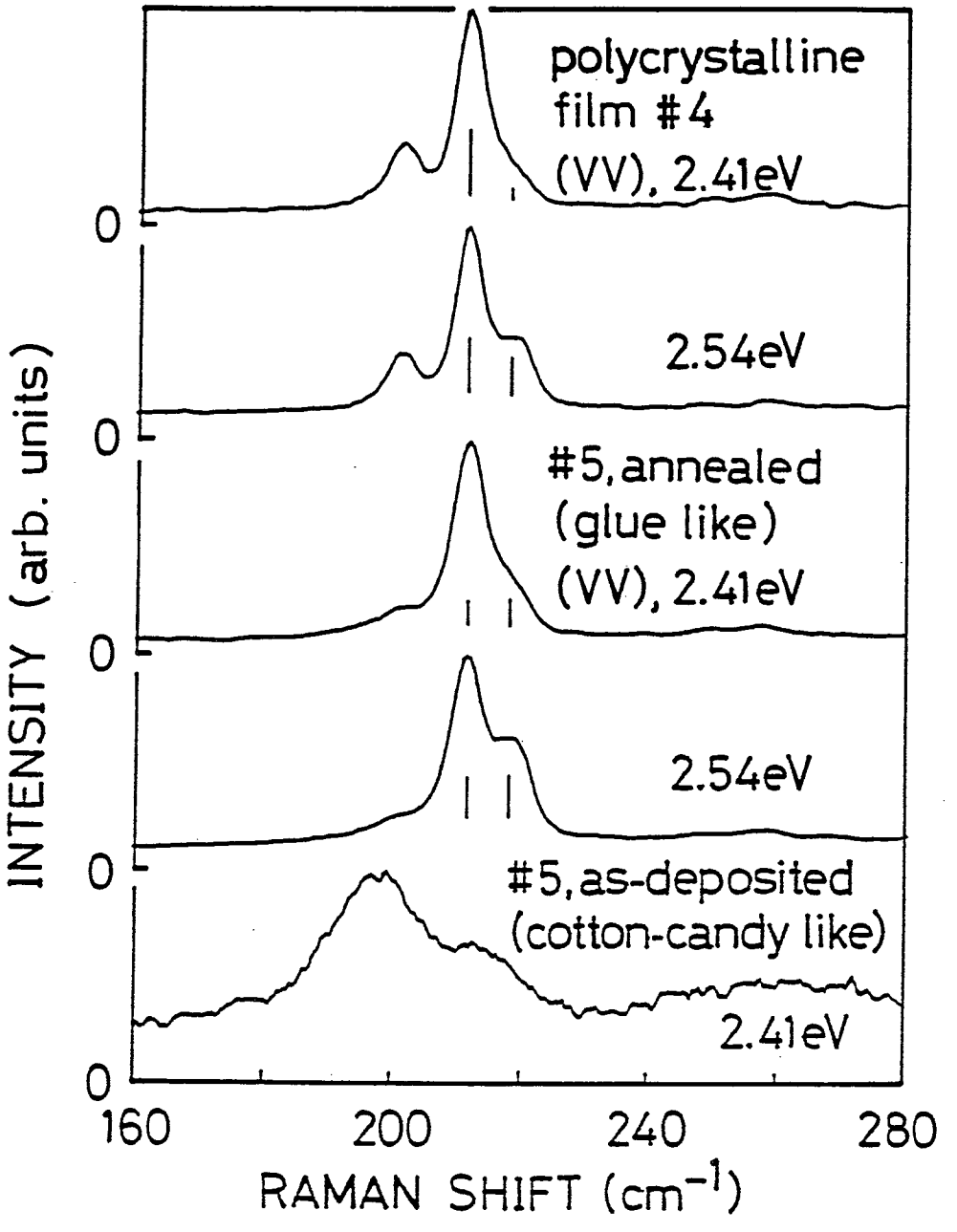

Figure 49: Raman spectra of $GeSe_2$ for (A) the polycrystalline film #4 (vacuum-evaporated and annealed) in (VV) by 2.41 eV excitation, (B) #4 by 2.54 eV excitation, (C) the polycrystalline film #5 (gas-evaporated and annealed) in (VV) by 2.41 eV excitation, (D) #5 by 2.54 eV excitation, and (E) as-deposited #5 by 2.41 eV excitation. Vertical bars indicate the 211 cm^{-1} bands and the 216 cm^{-1} bands. To avoid the sample heating, the excitation power was less than 10 mW and the line-focusing geometry was used.

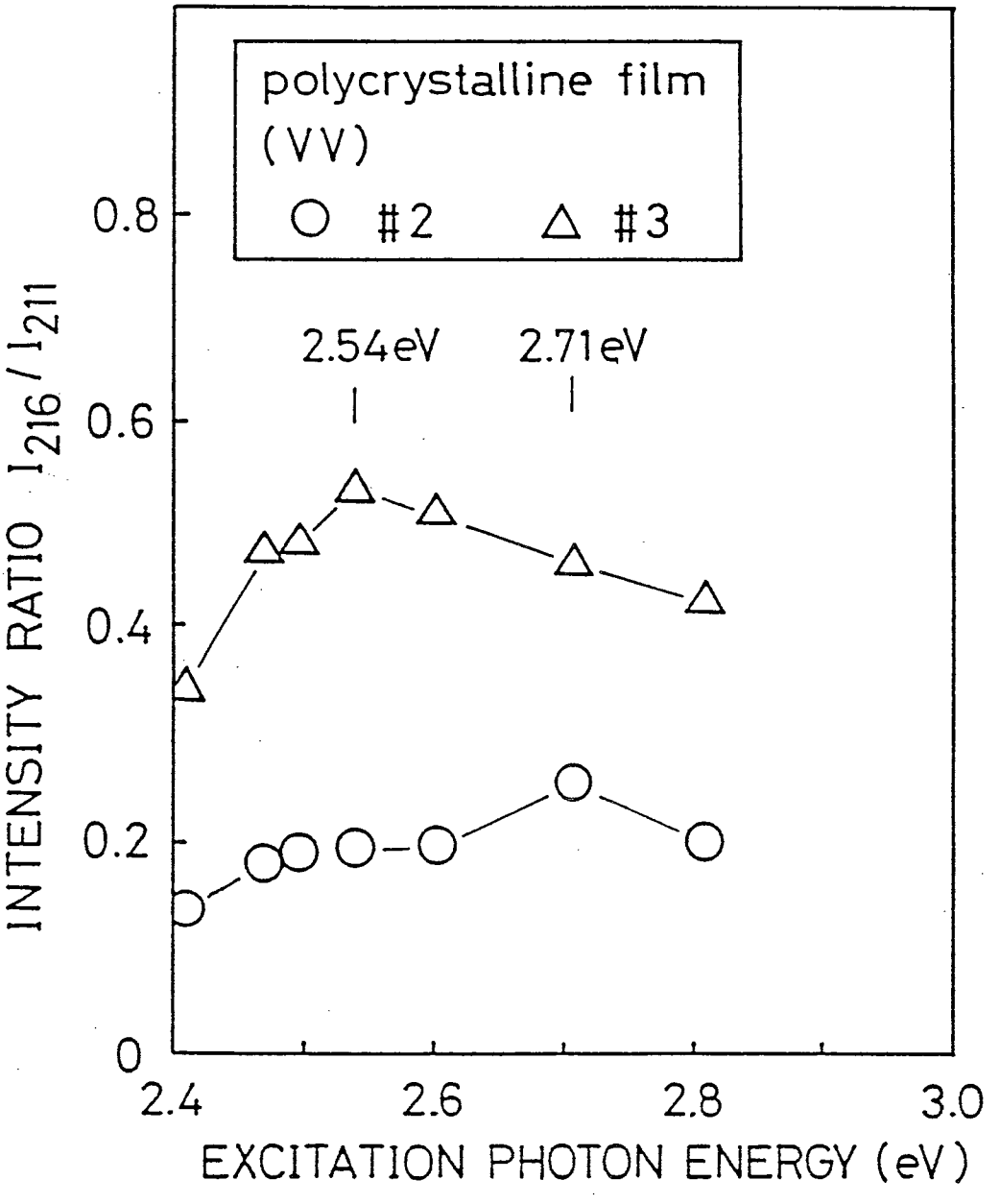

Figure 50: I_{216}/I_{211} spectra for polycrystalline $GeSe_2$ film #2 and #3. Lines are guides to the eyes. The excitation energies where the intensity ratios I_{216}/I_{211} are maximized are different between the films #2 (2.71 eV) and #3 (2.54 eV).

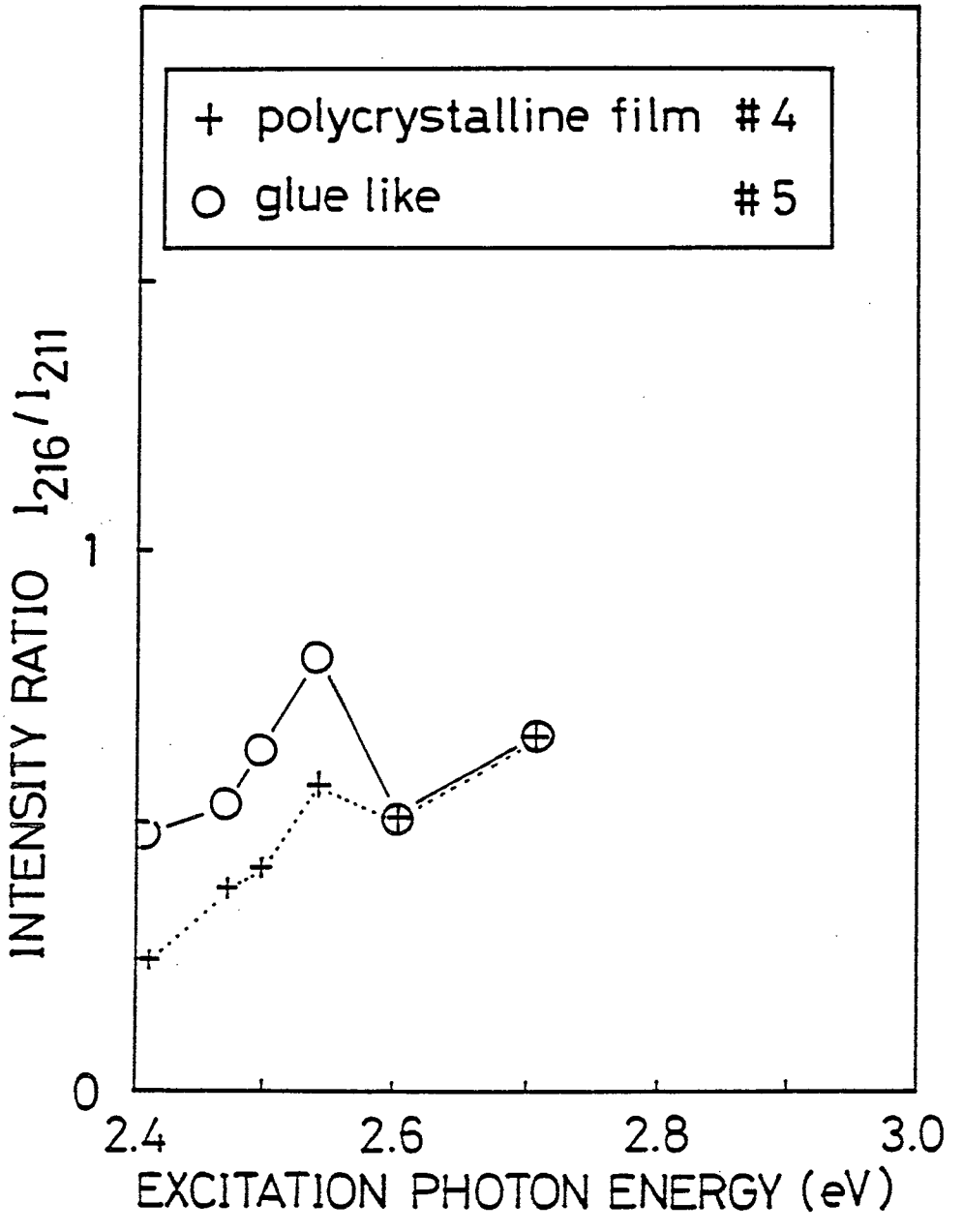

Figure 51: I_{216}/I_{211} spectra for polycrystalline $GeSe_2$ film #4 and #5. Lines are guides to the eyes. The excitation energies where the intensity ratios I_{216}/I_{211} are maximized are 2.54 eV for both films #4 and #5.

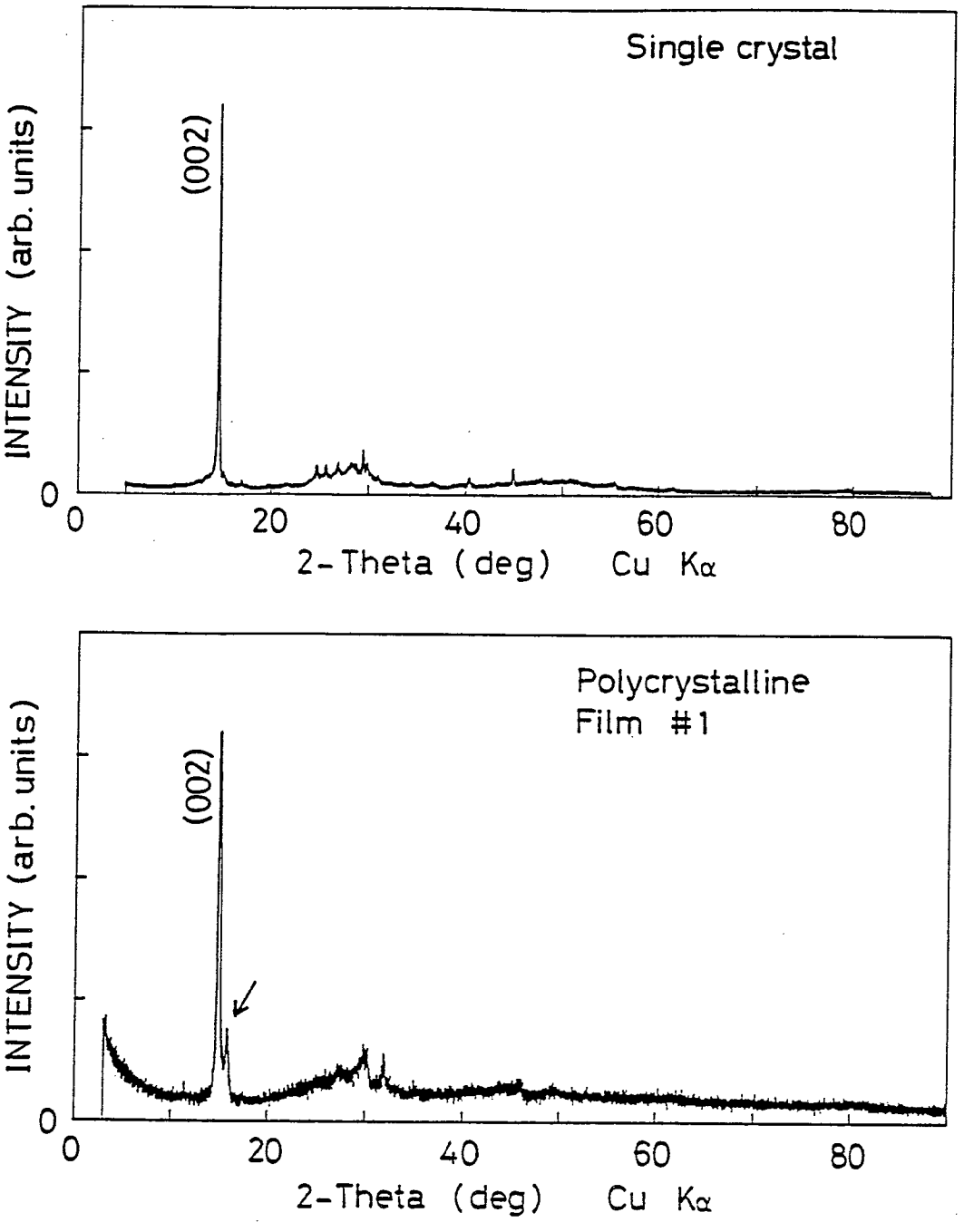

Figure 52: X-ray diffraction data for the powder of the single crystalline $GeSe_2$ (Upper half) and the polycrystalline film #1 (Lower half). The most intense line is the (002) peak. The (002) peak in the film #1 is accompanied by a satellite peak (arrow).

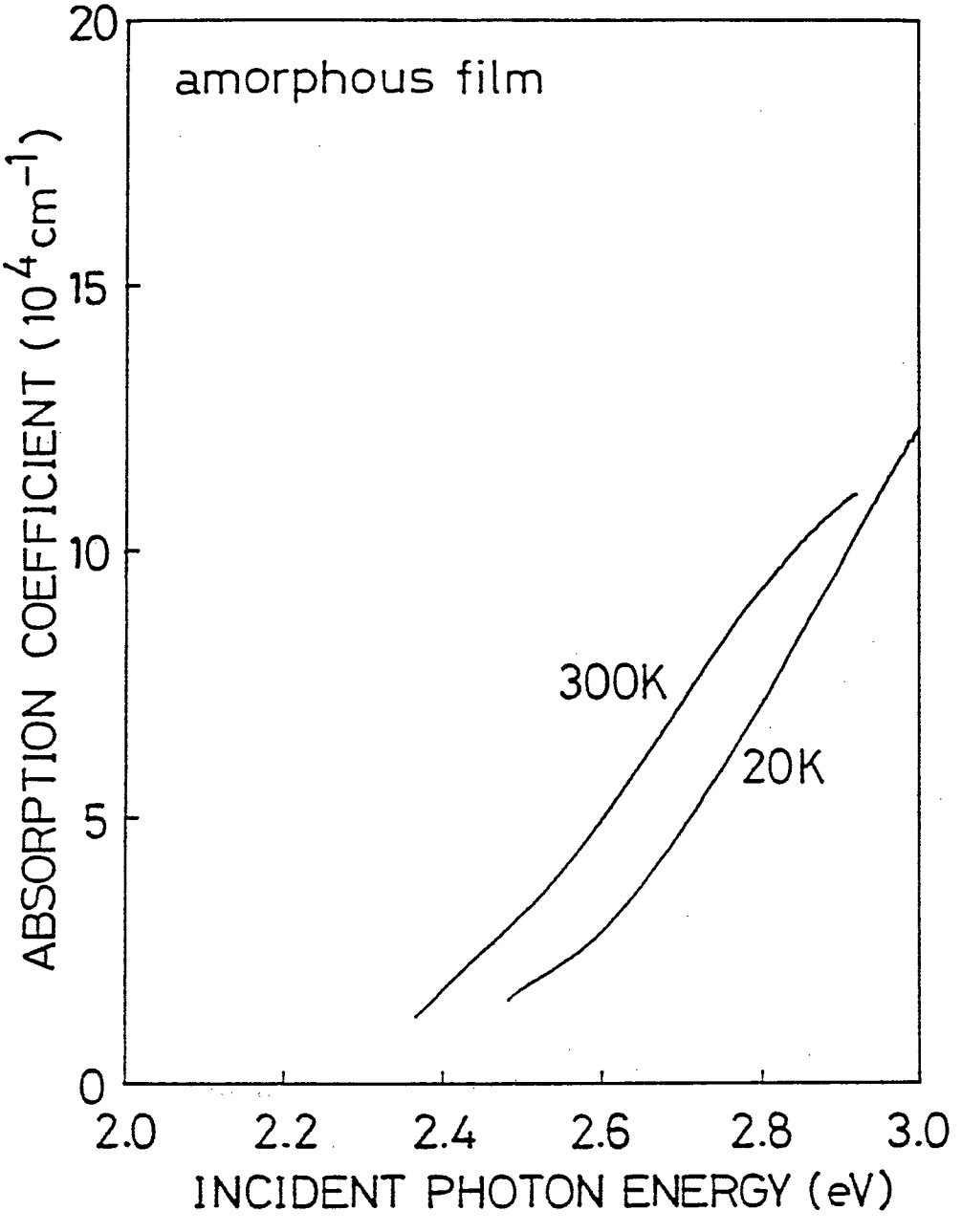

Figure 53: Absorption spectra for a–$GeSe_2$ at 20 K and 300 K. As the temperature decreases, the absorption edge moves toward the high energy side.

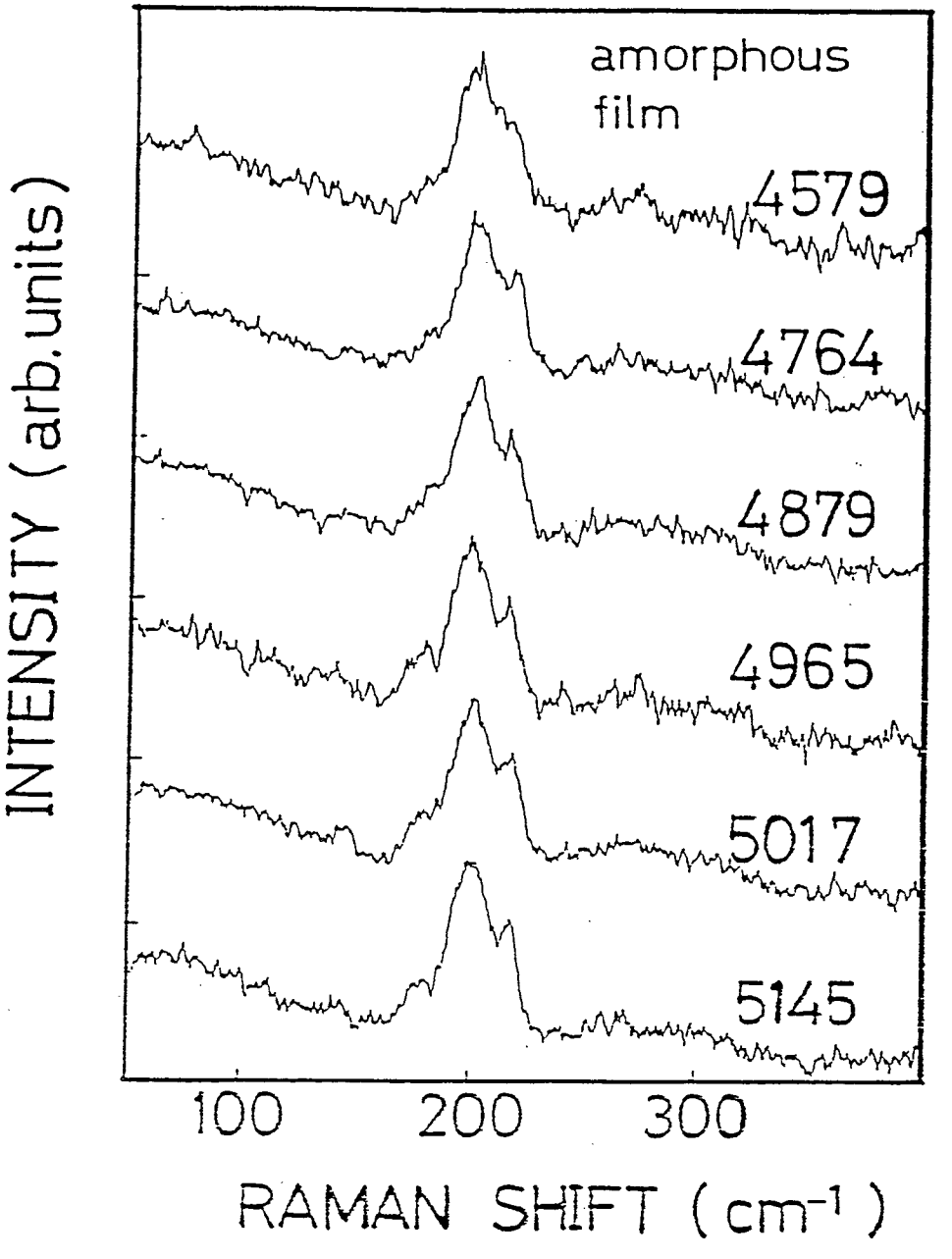

Figure 54: Excitation photon energy dependence of Raman spectra for a–$GeSe_2$ in the (VV) configuration. Wave length (Å) of the excitation light is shown in the figure. To avoid the sample heating, the excitation power was less than 10 mW and the line focusing geometry was used.

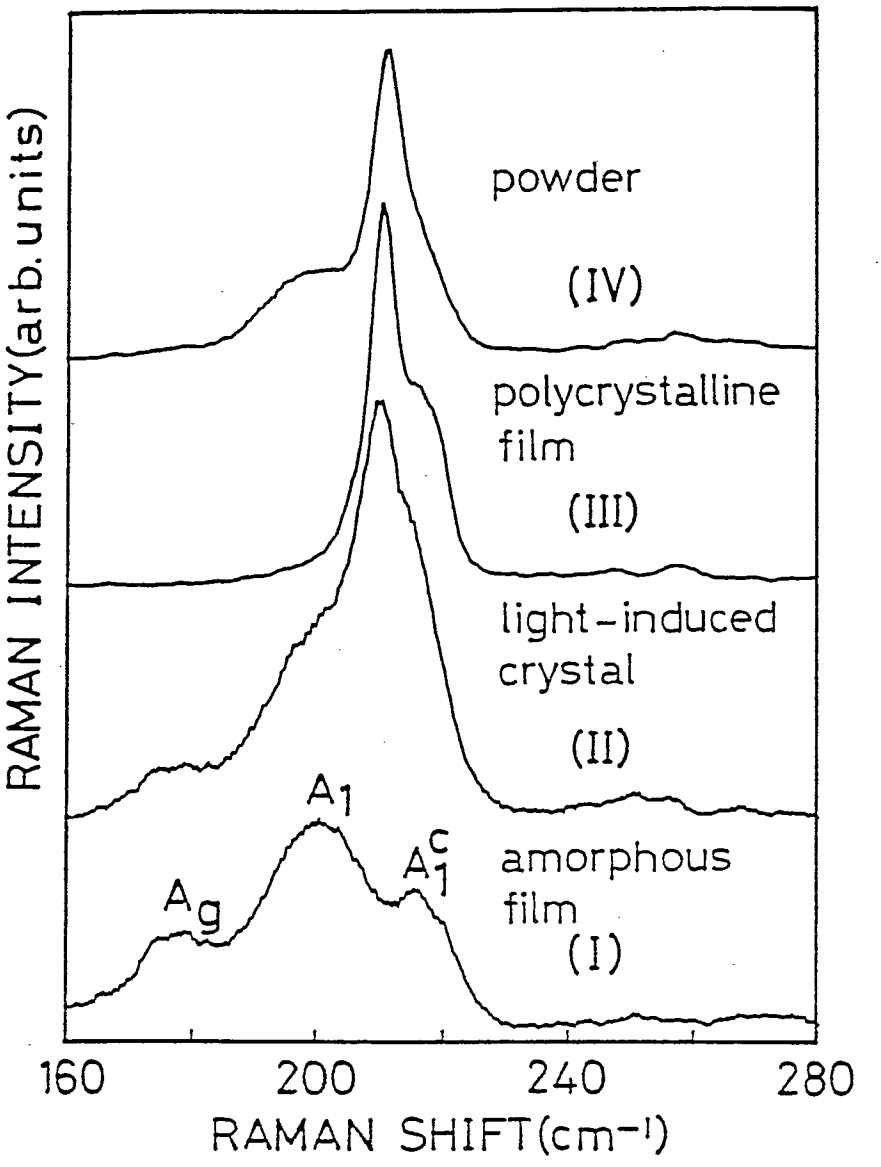

Figure 55: Raman spectra of a- and c-$GeSe_2$ prepared by various methods; (I) amorphous film, (II) light-induced micro crystal from amorphous film, coexisting with amorphous phase, (III) poly-crystalline film by thermal annealing of amorphous film, and (IV) ground c-$GeSe_2$ powder. The excitation energy is 2.41 eV (5145 Å). The 216 cm^{-1} band appear in (II)-(IV), and its position is almost the same as the A_1^C band position. It should be noticed that the A_1 band at 199 cm^{-1} even appears in (IV). The A_G mode at 178 cm^{-1}, observed in (I) and (II), comes from Ge-Ge bonds due to a chemical disorder which is absent in (III) and (IV) (From Ref. 42).

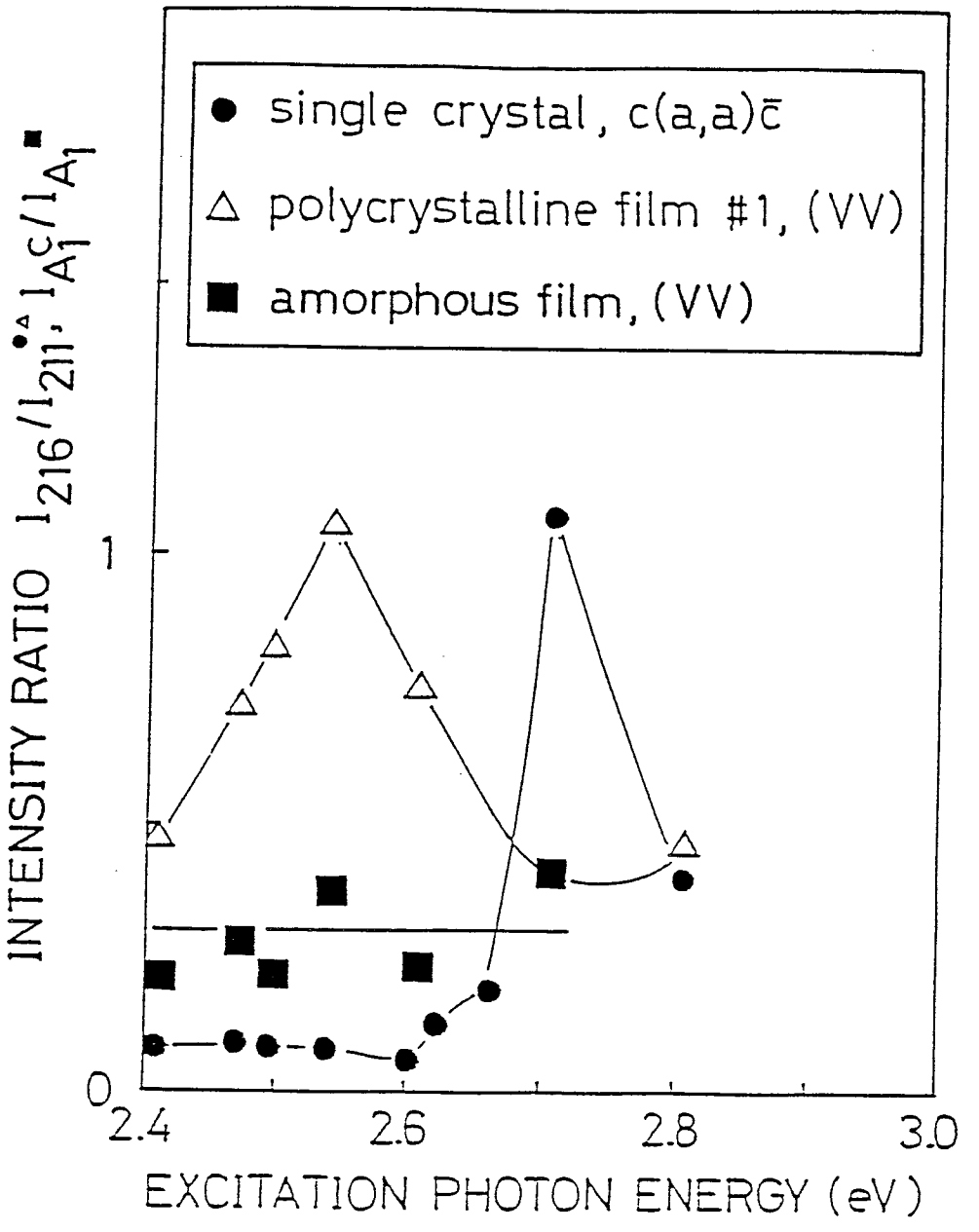

Figure 56: Intensity ratios of two Raman bands. ●: I_{216}/I_{211} for the single crystalline β–$GeSe_2$ in the c(a,a)c̄ configuration. △: I_{216}/I_{211} for the polycrystalline $GeSe_2$ film #1 in the (VV) configuration. ■: Ratio of the A_1^C band to the A_1 band for the amorphous $GeSe_2$ film in the (VV) configuration. Lines are guides to the eyes.

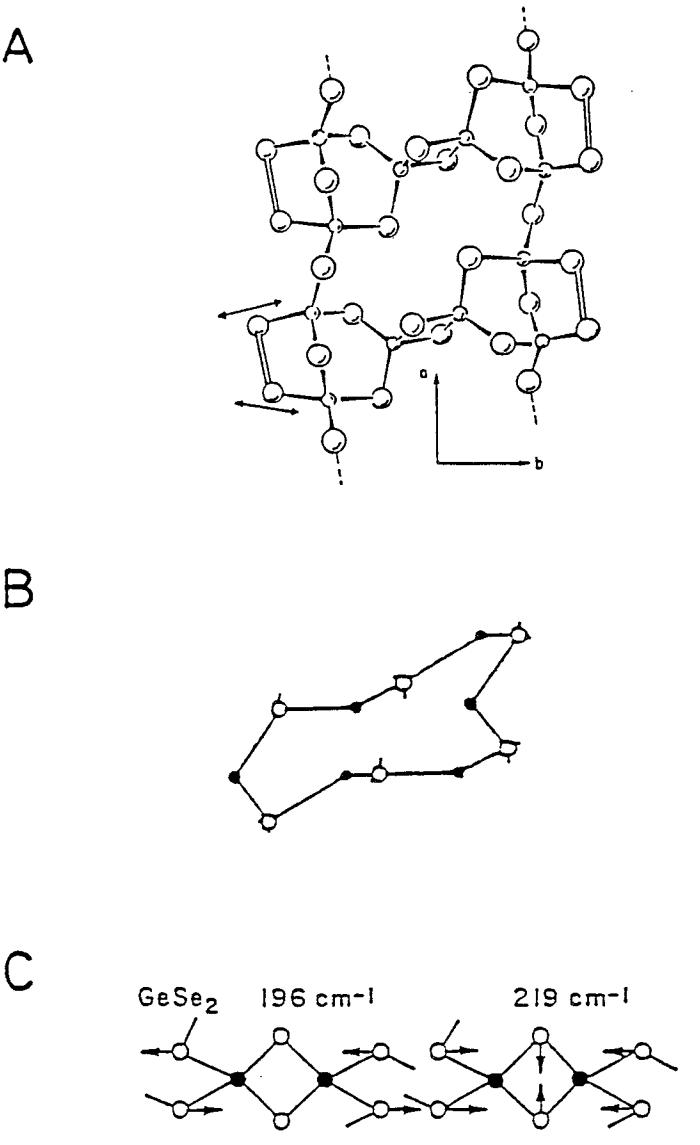

Figure 57: Some structural models for a–$GeSe_2$. A: The outrigger raft model. Larger circles denote Se atoms and smaller ones Ge atoms (From Ref. 12). B: The Ge_6Se_6 ring structure. Open circles denote Ge atoms and closed ones Se atoms (From Ref. 17). C: The Ge_2Se_2 ring structure. Open circles denote Se atoms and closed ones Ge atoms. The vibrational modes for the A_1 (196 cm^{-1}) and A_1^C (219 cm^{-1}) bands are also shown (From Ref. 15).

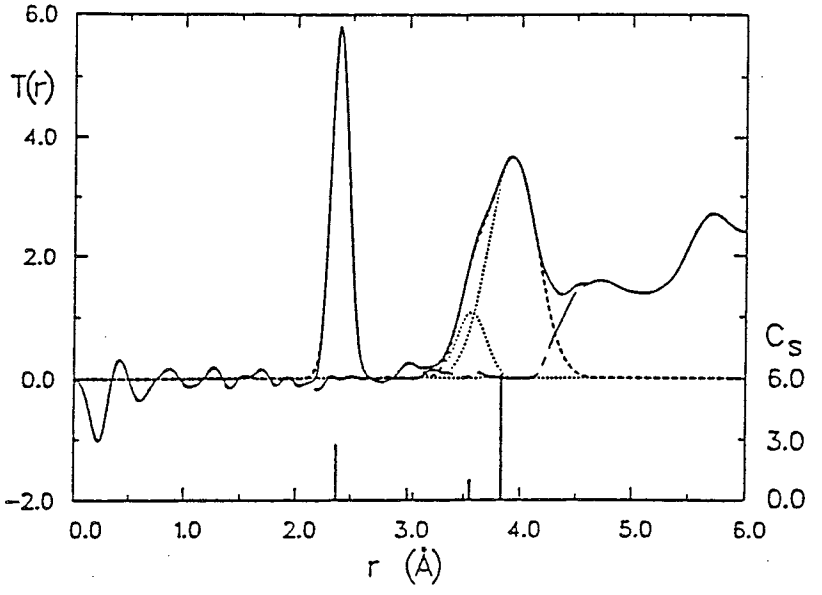

Figure 58: Total correlation function for amorphous $GeSe_2$ at 10 K (Solid line). The dashed line shows the fit of the first four nearest neighbor by gaussians. The bars show the characteristic inter-atomic distances in the crystal: Ge–Se in the tetrahedra (2.385 Å), Ge–Ge in the edge-sharing bi-tetrahedra (3.02 Å), Ge–Ge in the corner-sharing tetrahedra (3.57 Å), and Se–Se (3.93 Å). These distances agree well with the positions of four gaussians (From Ref. 58).

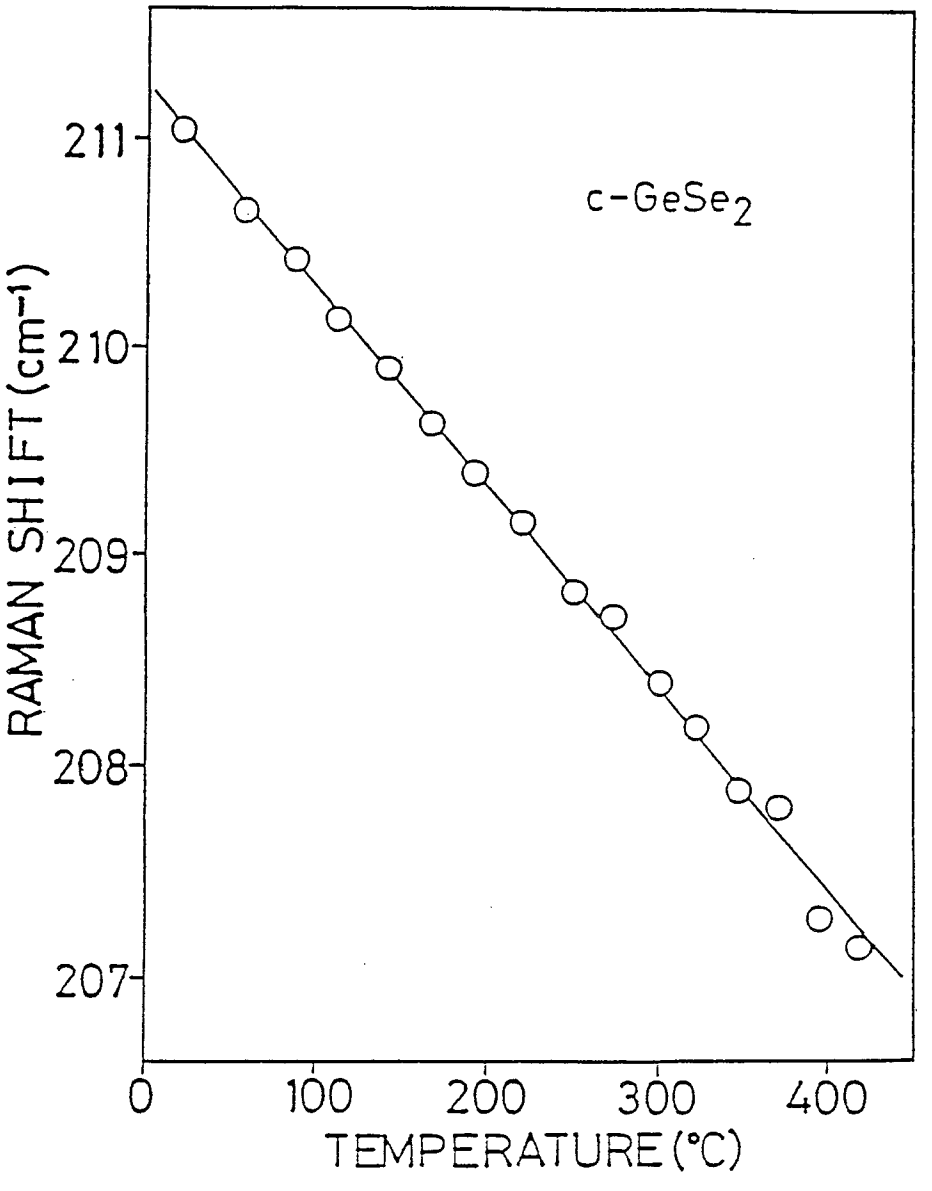

Figure 59: Temperature dependence of peak position of 211 cm^{-1} band for single crystalline β–$GeSe_2$. Excitation was 0.5 mW (point-focusing), 2.41 eV (5145 Å).

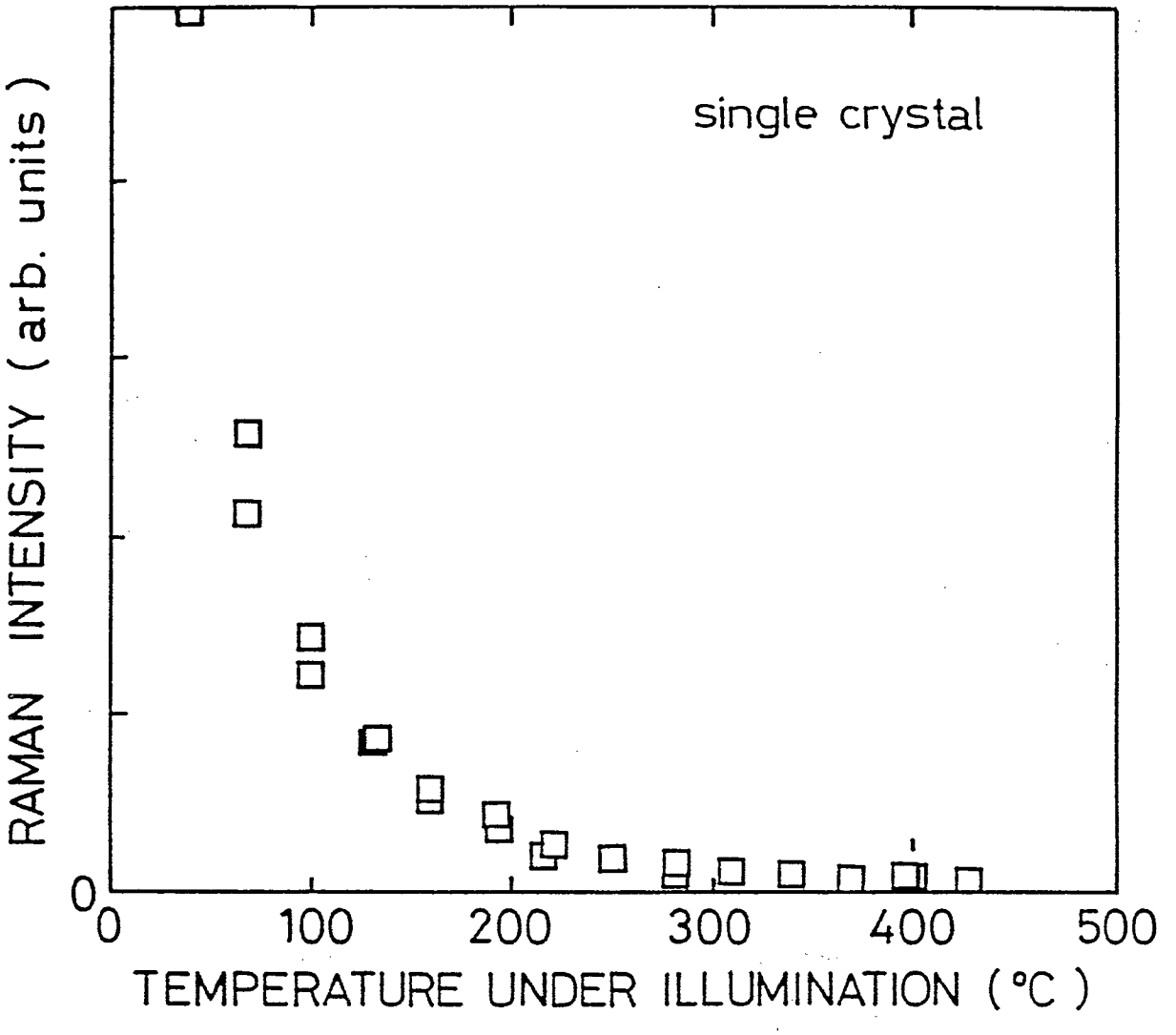

Figure 60: Temperature dependence of intensity of 211 cm^{-1} band for single crystalline β–$GeSe_2$. Excitation was 0.5 mW (point-focusing), 2.41 eV (5145 Å).

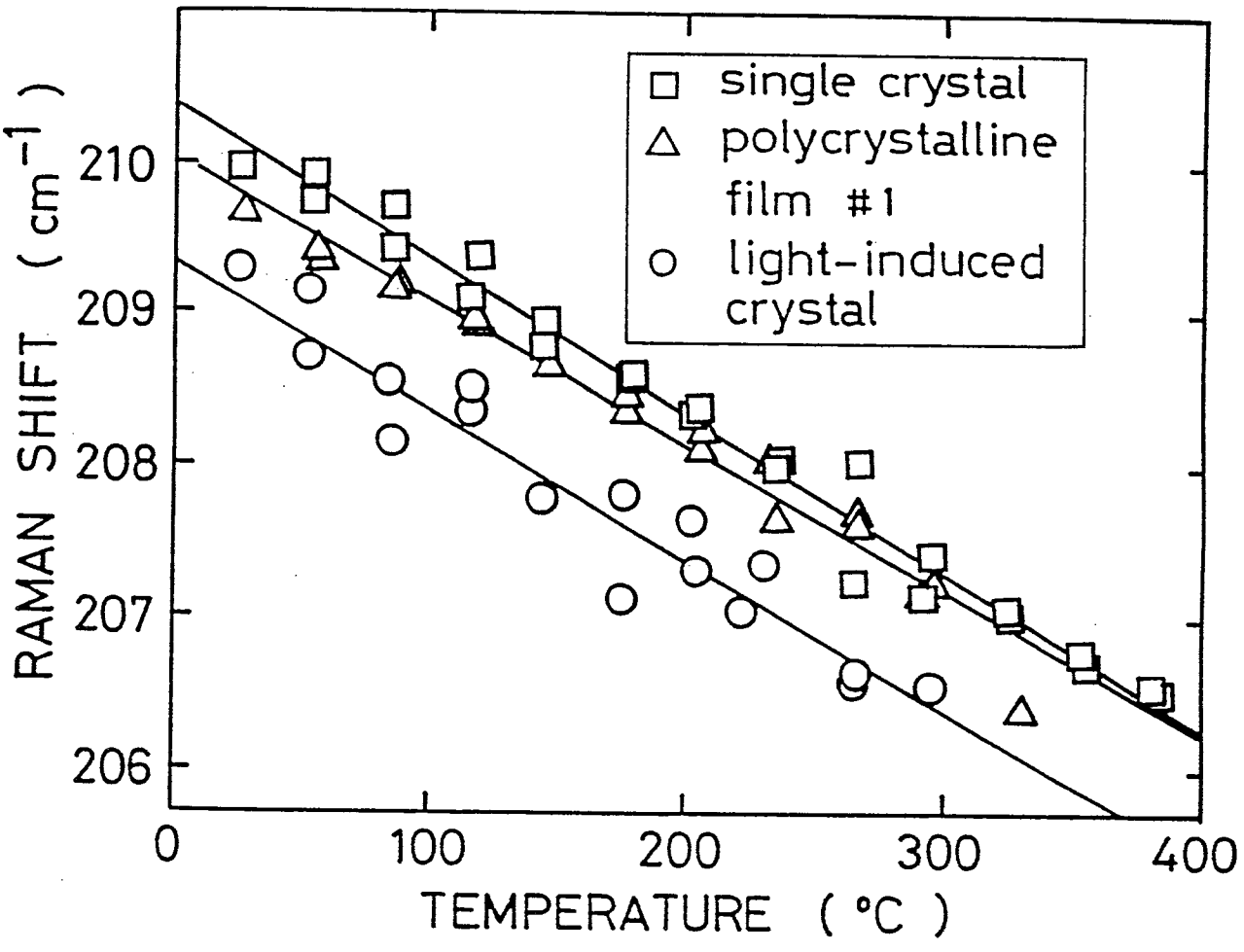

Figure 61: Environmental temperature dependence of the peak position of the 211 cm^{-1} band for bulk single crystalline β-$GeSe_2$ (□), polycrystalline film #1 (△), and light-induced micro crystal (○). Temperature coefficients of the peak position agree well for all crystals within the experimental accuracy. The parallel shifts among three lines are due to the sample heating. Excitation photon energy was 2.41 eV and the point-focusing geometry was used.

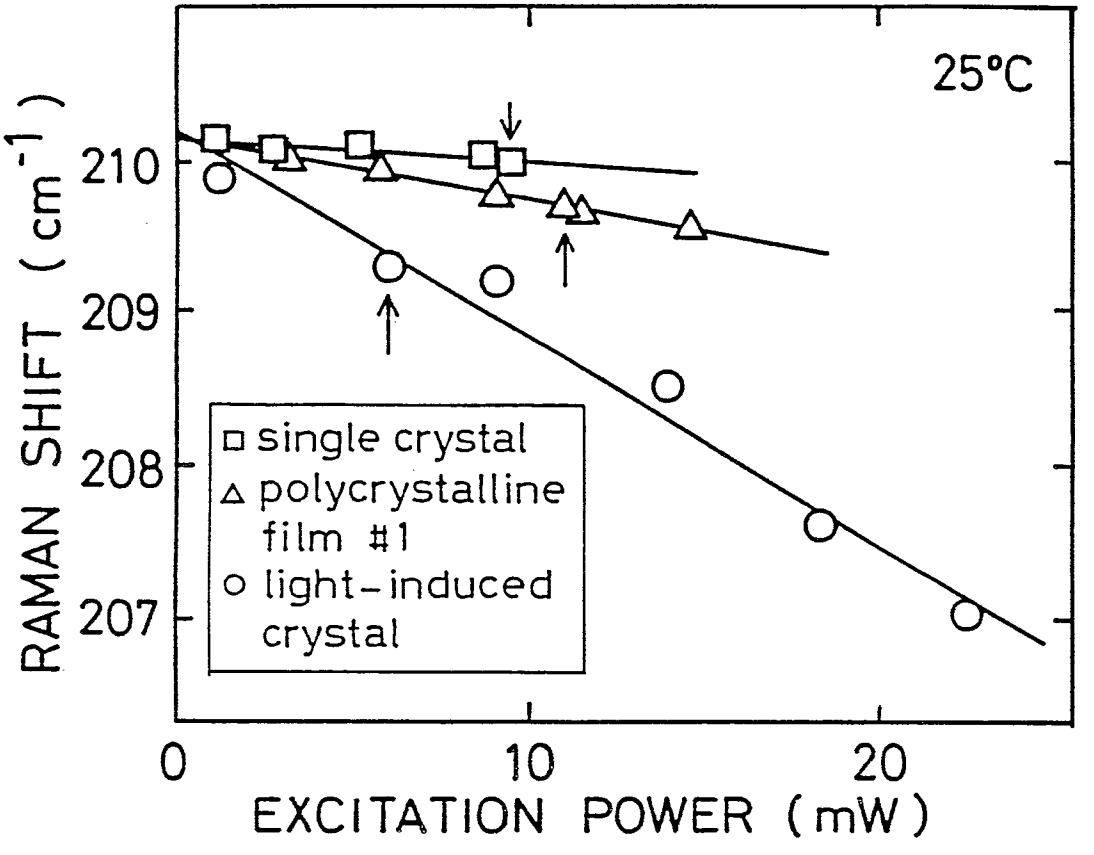

Figure 62: Excitation power dependence of the peak position of the 211 cm^{-1} band for bulk single crystalline β–$GeSe_2$ (□), polycrystalline film #1 (△), and light-induced micro crystal (○). The peak positions extrapolated to power zero agrees well for all crystals. Excitation photon energy was 2.41 eV and the point-focusing geometry was used. Arrows indicate the excitation powers for the measurement in Fig. 61.

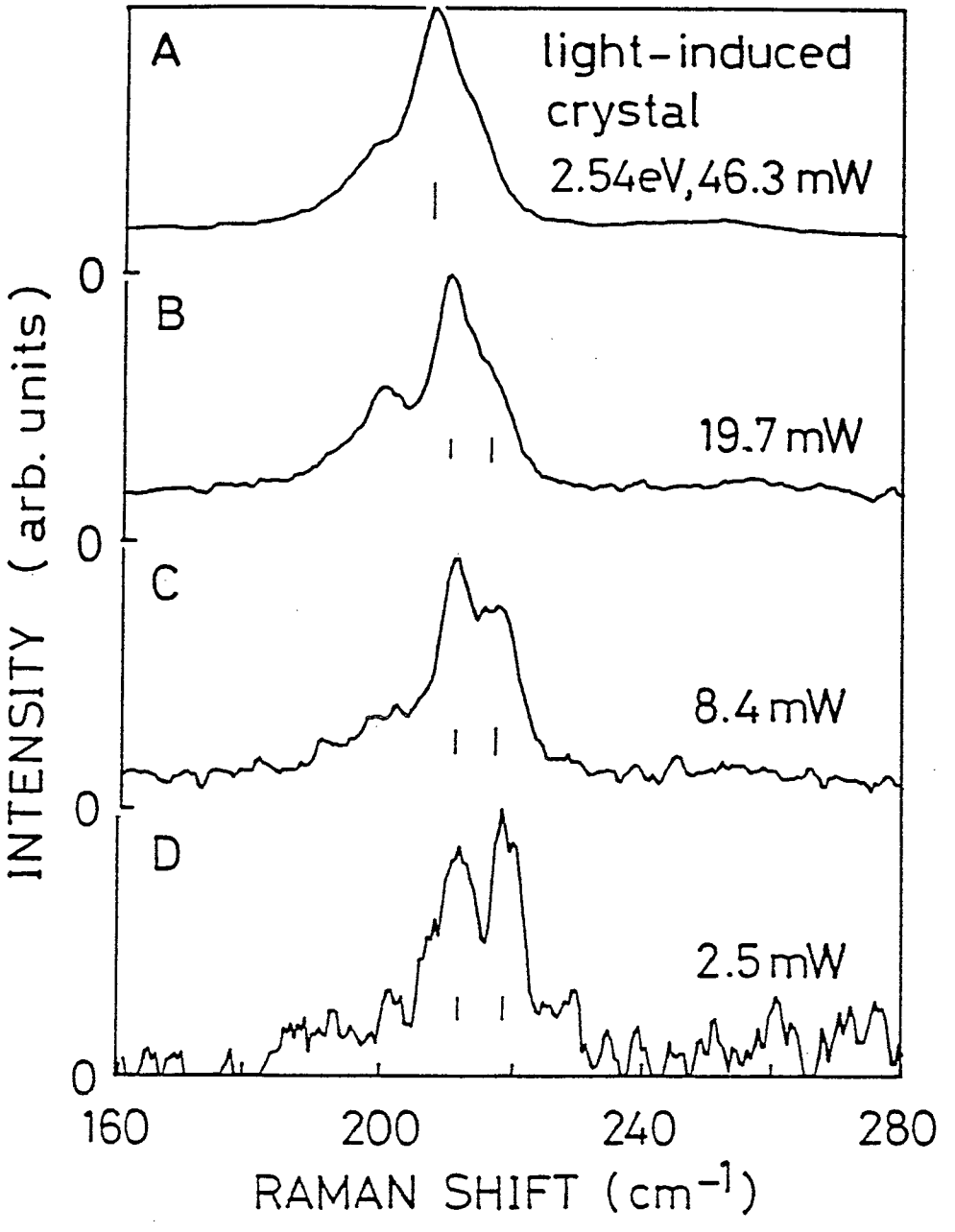

Figure 63: Raman spectra of light-induced crystallized sample at various probing powers; A: 46.3 mW, B: 19.7 mW, C: 8.4 mW, and D: 2.5 mW. The intensity ratio I_{216}/I_{211} increases with decreasing prove light power. The excitation photon energy is 2.54 eV (4880 Å). Point-focusing geometry was used.

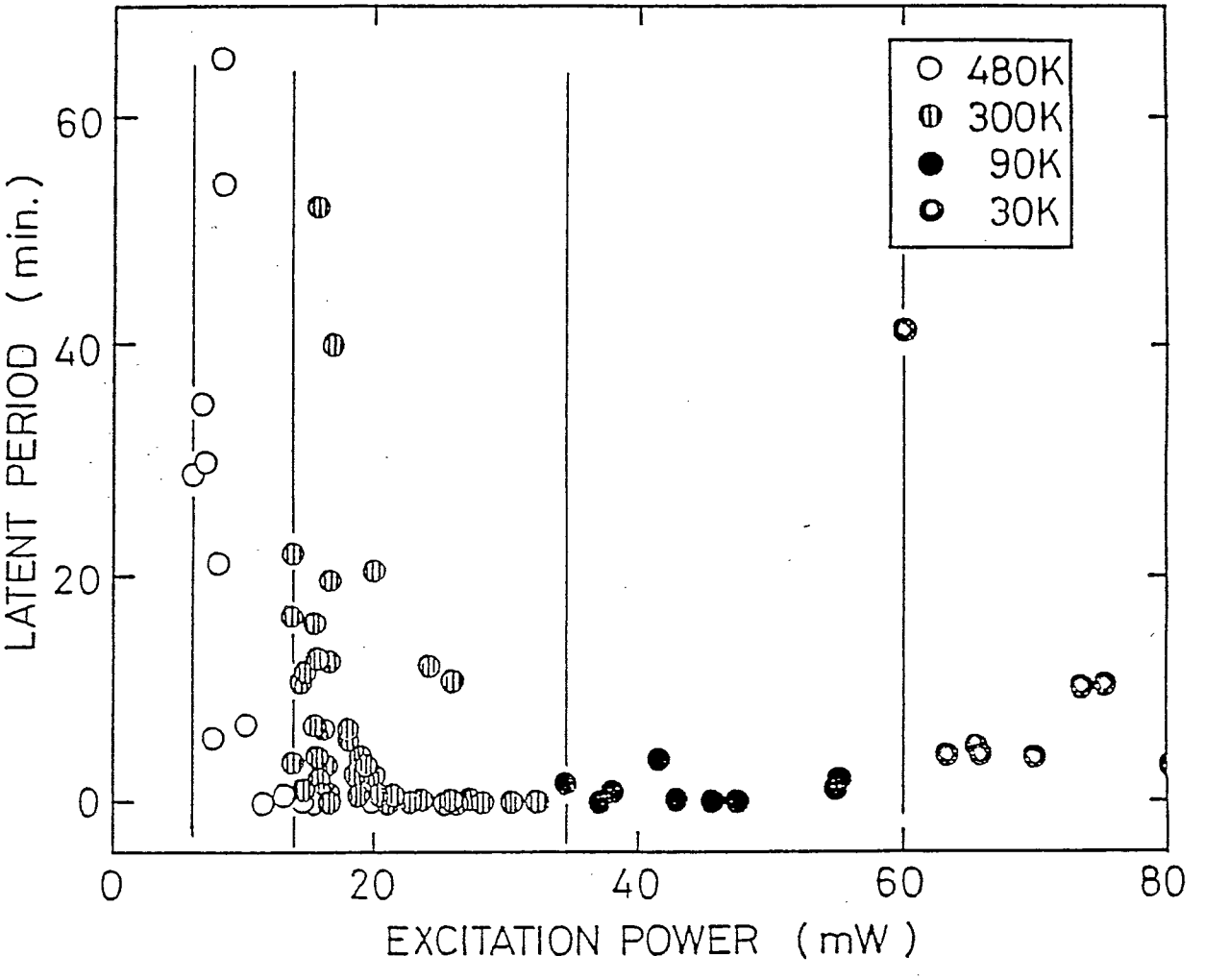

Figure 64: Excitation power dependence of the latent period t_0. The excitation photon energy is 2.41 eV (5145 Å). The threshold power for the crystallization increases with decreasing environmental temperature of the sample.

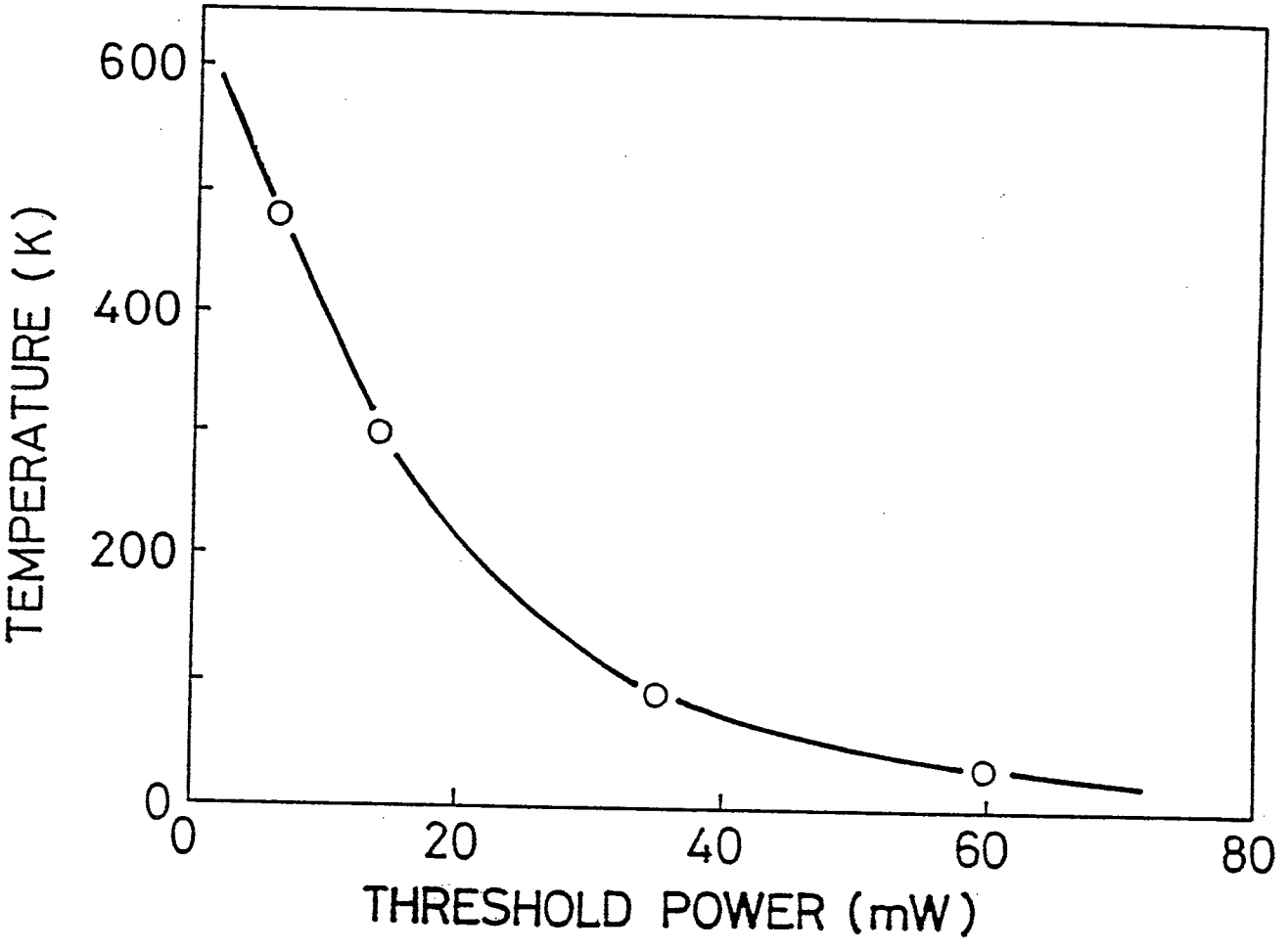

Figure 65: Environmental temperature dependence of the threshold power. The excitation photon energy is 2.41 eV (5145 Å). The threshold power increases with decreasing environmental temperature.

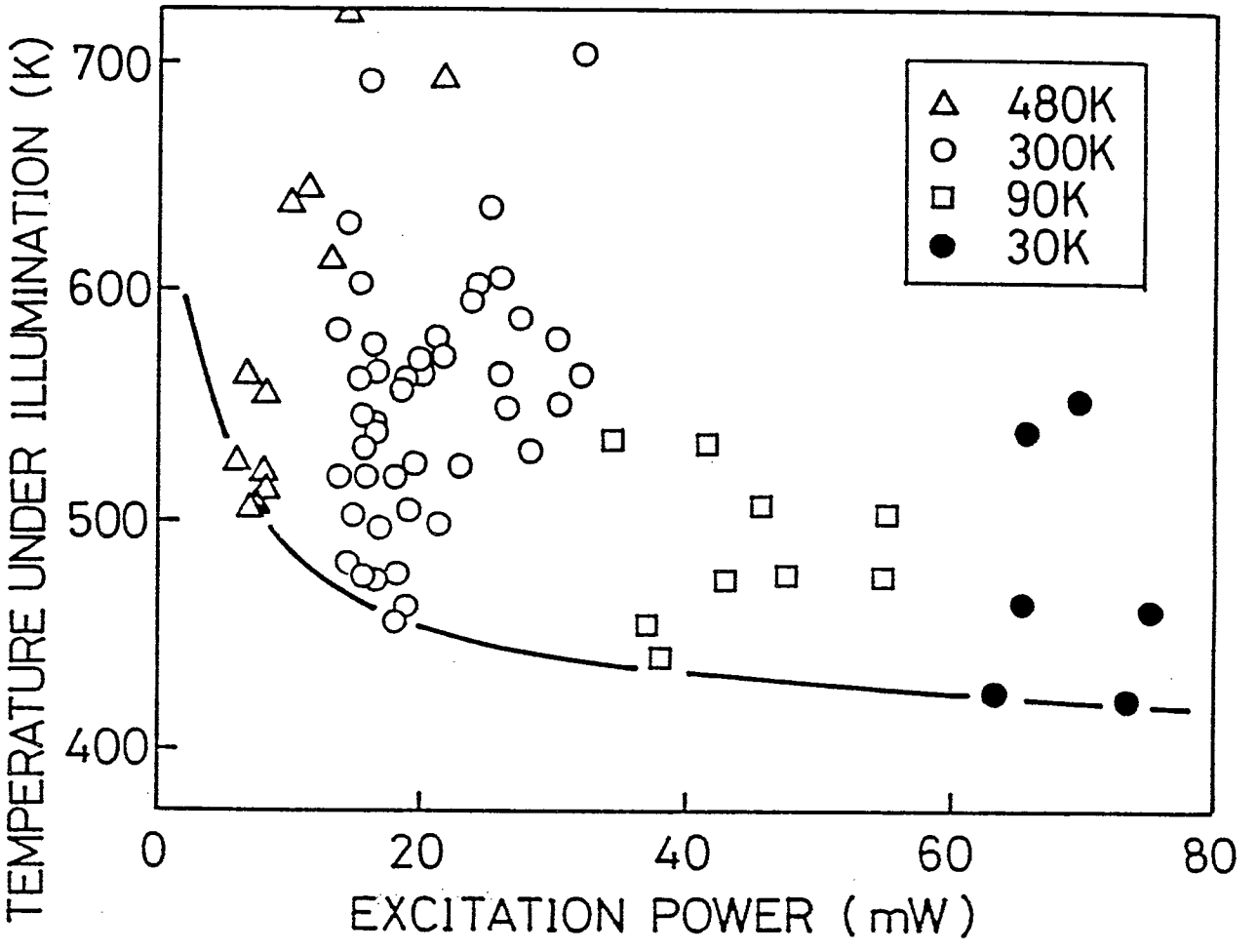

Figure 66: The relation between the excitation power and the temperature under illumination which leads the light-induced crystallization. In the above region with respect to the solid line, the light-induced crystallization occurs with 2.41 eV (5145 Å) light. It is considered to be the phase-diagram of the light-induced crystallization.

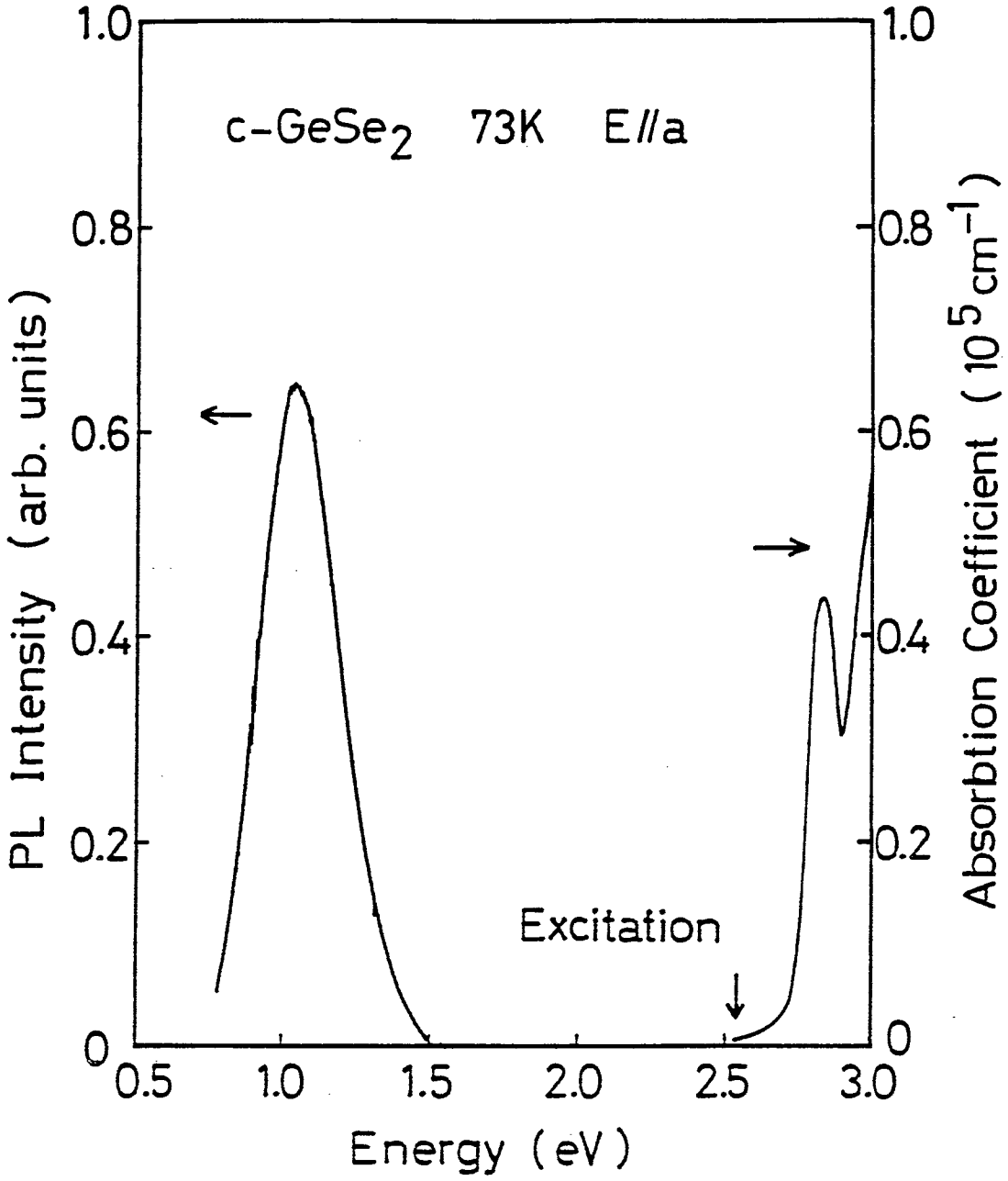

Figure 67: Photo-luminescence spectra (left side) and absorption spectra (right side) of β–$GeSe_2$ by 2.54 eV excitation at 73 K.

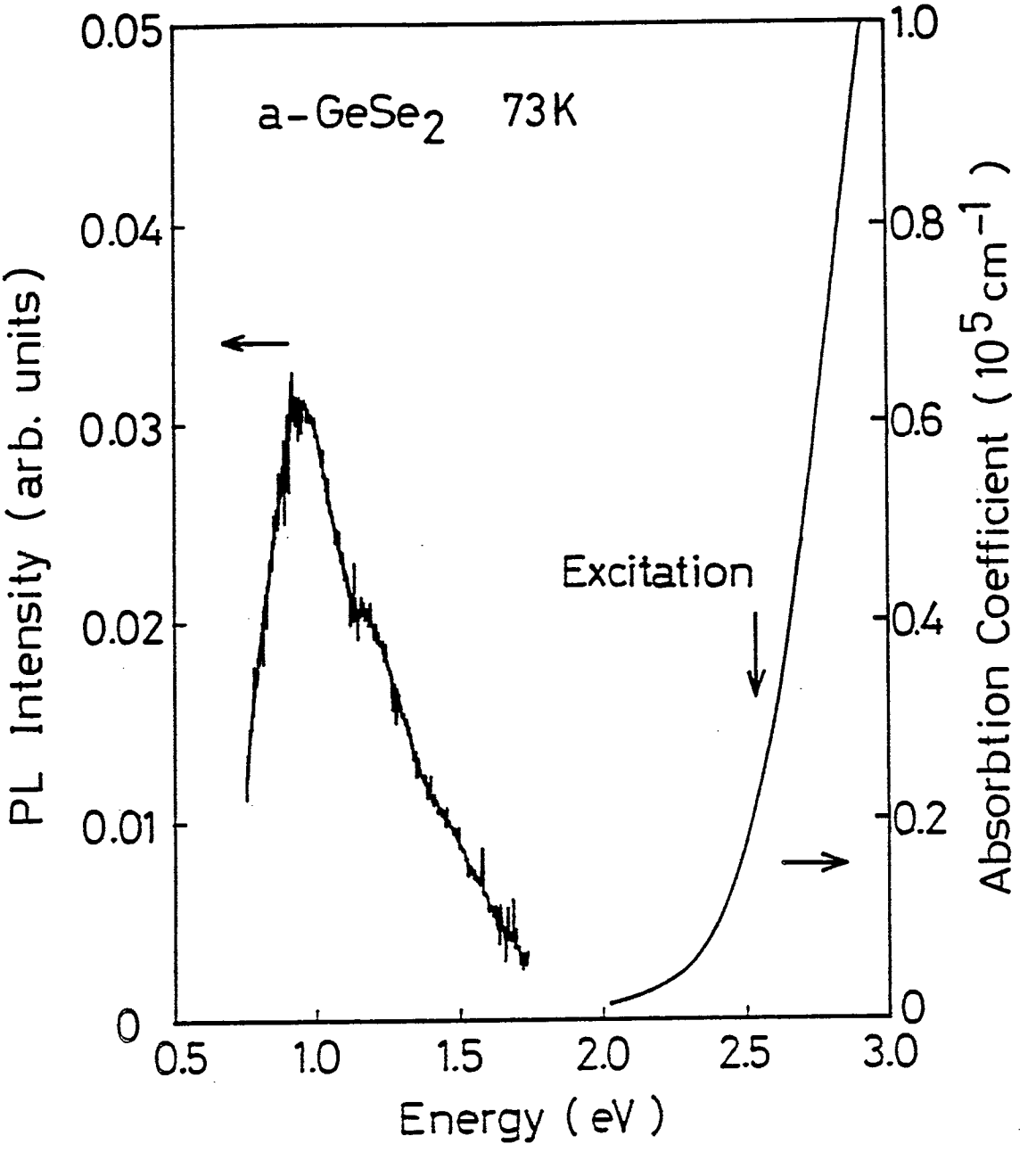

Figure 68: Photo-luminescence spectra (left side) and absorption spectra (right side) of a–$GeSe_2$ by 2.54 eV excitation at 73 K.

5 Summary

In this thesis, two subjects relating to the photo-crystallization of $GeSe_2$ were reported. One was to clarify the vibrational and electronic properties of various forms of $GeSe_2$, from the amorphous state to the crystalline state. For this purpose, we studied the Raman spectra of single crystalline $GeSe_2$, polycrystalline $GeSe_2$, amorphous $GeSe_2$, and light-induced crystalline $GeSe_2$ with various excitation photon energies from 2.0 to 2.8 eV. The other was to clarify the roles of the electronic excitation and of the thermal excitation in the light-induced crystallization process. For this purpose, the light-induced crystallization at various environmental temperatures was examined.

In the case of the single crystalline $GeSe_2$, the Raman scattering cross section increases, as the excitation energy increases near the optical gap. In most cases, the intensity of the Raman 211 cm^{-1} band, which is due to the breathing motion of the corner-sharing chain $GeSe_{4/2}$ tetrahedra, is much stronger than that of the 216 cm^{-1} band, which is due to the breathing motion of the edge-sharing bridge bi-tetrahedra. However, at the 2.71 eV (4579 Å) excitation in the $c(a,a)\bar{c}$ configuration, the 216 cm^{-1} band becomes nearly equal to the 211 cm^{-1} band in intensity at the expense of the 211 cm^{-1} band.

These phenomena were connected with the exciton transition which is observed in the absorption spectra of $\boldsymbol{E} \parallel \boldsymbol{a}$ near 2.7 eV. We have proposed a model as follows. 1) The exciton is related to the electronic transition from the $4p$ lone pair states quasi-localized at the Se atoms of the edge-sharing bridge $Ge_2Se_{8/2}$ bi-tetrahedra to the s–like anti-bonding states of the Ge atoms of the edge-sharing bridge bi-tetrahedra. 2) The 216 cm^{-1} mode is a symmetric breathing mode quasi-localized on the edge-sharing bridge $Ge_2Se_{8/2}$ bi-tetrahedra. The relative enhancement of the 216 cm^{-1} band will be due to an electron-phonon interaction between the exciton and the 216 cm^{-1} phonon.

As for the polycrystalline $GeSe_2$ films, the excitation energy dependence of the

Raman spectra is different from sample to sample depending on the preparation conditions. In some cases, it was observed that the 216 cm^{-1} band becomes slightly stronger than the 211 cm^{-1} band at 2.54 eV excitation at the expense of the 211 cm^{-1} intensity. The energy 2.54 eV is much lower than the energy 2.70 eV where the enhancement takes place in the single crystal. This energy difference comes from the disorder involved in the polycrystal. Although the disorder seems to be related to the stacking fault of the crystalline layers, the concrete description of the disorder is the subject in the future.

From the behavior of the 216 cm^{-1} band in disordered micro-crystals, we conclude that the A_1^C band in a–$GeSe_2$ originates from the edge-sharing $Ge_2Se_{8/2}$ bi-tetrahedra in the medium-range order of topologically layered-crystalline-like fragments.

It should be stressed that the resonant Raman experiments described here provide a powerful method to the investigation of the disorder in the crystals or that of the medium-range structure in the glass.

The light-induced crystallization process at various environmental temperatures was observed by the time resolved Raman experiment. We conclude that the photo-crystallization is not caused by a purely thermal process, though the thermal excitation is also indispensable. Both the electronic excitation by light irradiation and thermal excitation are essentially important to the crystallization. The final crystalline state of the light-induced crystallization, that is the type A (β–$GeSe_2$) or the type B (α–$GeSe_2$ + β–$GeSe_2$), depends on the medium-range structure in the initial amorphous state. On the other hand, in the thermal equilibrium process, the final state of the crystallization, that is α–$GeSe_2$ or β–$GeSe_2$, is uniquely destined by the annealing temperature.

The subjects to be investigated in future are as follows:

- The mechanism of the lowering of the exciton transition energy by the disorder in the crystal.

- The detailed description of the disorder in the crystal.
- The relaxation process of the excited electrons in the light-induced crystallization.

References

1. K. Tanaka, in *Fundamentals of Amophous Semicondumtors* (In Japanese), ed. by M. Kikuchi and K. Tanaka (Ohm, Tokyo, 1982), p.129.
2. K. Tanaka, *Appl. Phys. Lett.* **26**, 243 (1975).
3. J. Hajtó, *J. Phys. (Paris)* **41**, C4–63 (1980).
4. J. E. Griffiths, G. P. Espinosa, J. P. Remeika, and J. C. Phillips, *Solid State Commun.* **40**, 1077 (1981).
5. I. Abdulhalim, R. Beserman, and Yu. L. Khait, *J. Non-Cryst. Solids* **97 & 98**, 387 (1987).
6. A. E. Owen, A. P. Firth, P. J. S. Ewen, *Philos. Mag.* **B52**, 347 (1985).
7. K. A. Rubin and M. Chen, *This Solid Films* **181**, 129 (1989).
8. W. Leung, A. R. Neureuther, and W. G. Oldham, *J. Vac. Sci. Technol. B* **3(1)**, 310 (1985).
9. K. J. Polasko, R. F. W. Pease, E. E. Marinero, and M. R. Cagan, *J. Vac. Sci. Technol. B* **3(1)**, 319 (1985).
10. P. Tronc, M. Bensoussan, A. Brenac, and C. Sebenne, *Phys. Rev. B* **8**, 5947 (1973).
11. P. Tronc, M. Bensoussan, A. Brenac, G. Errandonea, and C. Sebenne, *J. Phys. (Paris)* **38**, 1493 (1977).
12. P. M. Bridenbaugh, G. P. Espinosa, J. E. Griffiths, J. C. Phillips, and J. P. Remeika, *Phys. Rev. B* **20**, 4140 (1979).
13. J. A. Aronovitz, J. R. Banavar, M. A. Marcus, and J. C. Phillips, *Phys. Rev. B* **28**, 4454 (1983).
14. N. Kumagai, J. Shirafuji, and Y. Inuishi, *J. Phys. Soc. Jpn.* **42**, 1262 (1977).
15. G. Lucovsky, C. K. Wong, and W. B. Pollard, *J. Non-Cryst. Solids* **59 & 60**, 839 (1983).
16. R. J. Nemanich, F. L. Galeener, J. C. Mikkelsen, Jr., G. A. N. Connell, G. Etherington, A. C. Wright, and R. N. Sinclair, *Physica* **117B & 118B**, 959

(1983).

17. R. J. Nemanich, S. A. Solin, and G. Lucovsky, *Solid State Commun.* **21**, 273 (1977).
18. K. Murase, T. Fukunaga, K. Yakushiji, T. Yoshimi, and I. Yunoki, *J. Non-Cryst. Solids* **59** & **60**, 883 (1983).
19. D. E. Aspnes, J. C. Phillips, K. L. Tai, and P. M. Bridenbaugh, *Phys. Rev. B* **23**, 816 (1981).
20. Z. V. Popović and A. Breitschwerdt, *Phys. Lett.* **110A**, 426 (1985).
21. K. Inoue, T. Katayama, K. Kawamoto, and K. Murase, *Phys. Rev. B* **35**, 7496 (1987). The crystal orientation is mistaken in the literature; replace $\parallel a$ with $\perp a$, and vice versa. It will cause no influence on conclusions.
22. S. A. Boiko, D. I. Bletskan, and S. F. Terekhova, *phys. stat. sol. (b)* **90**, K49 (1978).
23. Z. V. Popović and H. J. Stolz, *phys. stat. sol. (b)* **108**, 153 (1981).
24. Von. G. Dittmer and H. Schäfer, *Acta Cryst.* **B32**, 2726 (1976).
25. Von. G. Dittmer and H. Schäfer, *Acta Cryst.* **B32**, 1188 (1976).
26. Von. G. Dittmer and H. Schäfer, *Acta Cryst.* **B31**, 2060 (1975).
27. K. Inoue, K. Kawamoto, and K. Murase, *J. Non-Cryst. Solids* **95** & **96**, 517 (1987).
28. Liu Ch'ün-hua, A. S. Pashinkin, and A. V. Novoselova, *Russ. J. Inorg. Chem.* **7**, 1117 (1962).
29. D. I. Bletskan, V. S. Gerasimenko, and M. Yu. Sichka, *Sov. Phys. Crystallogr.* **24**, 45 (1979), translated from *Krystallografiya* **24**, 83 (1979).
30. V. V. Sobolev, V. M. Kramar', and Z. D. Kovalyuk, *Zh. Prikl. Spektrosk.* **39**, 52 (1983).
31. R. S. Tobias, *J. Chem. Education* **44**, 2 (1967).
32. K. Inoue, O. Matsuda, and K. Murase, to be published.
33. K. Inoue, O. Matsuda, and K. Murase, in *Proc. 20th Int. Conf. Phys. Semicond., Thessaloniki, Greece* (1990, in printing).

34. T. Katayama, Master's thesis at Osaka Univ. (1986).

35. S. G. Louie, *Phys. Rev. B* **26**, 5993 (1982).

36. O. Uemura, Y. Sagara, and T. Satow, *phys. stat. sol. (a)* **32**, K91 (1975).

37. P. H. Fuoss, P. Eisenberger, W. K. Warburton, and A. Bienenstock, *Phys. Rev. Let.* **46**, 1537 (1981).

38. D. E. Sayers, F. W. Lytle, and E. A. Stern, in *Amorphous and Liquid Semiconductors* **1**, *Proc. Intern. Conf. Amorphous and Liq. Semicond., Garmisch-Partenkirchen, FRG*, ed. by J. Stuke and W. Brenig (Taylor & Francis Ltd., London, 1974), p.403.

39. O. Uemura, Y. Sagara, D. Muno, and T. Satow, *J. Non-Cryst. Solids* **30**, 155 (1978).

40. P. Vashishta, R. Kalia, G. A. Antonio, and I. Ebbsjö, *Phys. Rev. Let.* **62**, 1651 (1989).

41. T. Fukunaga, Doctral thesis at Osaka Univ. (1982).

42. K. Murase and K. Inoue, in *DISORDERED SEMICONDUCTORS*, ed. by M. A. Kastner, G. A. Thomas and S. R. Ovshinsky (Plenum, New York, 1987), p.297.

43. S. C. Agarwal and H. Fritzsche, *Bull. Am. Phys. Soc.* **15**, 244 (1970).

44. H. Fritzsche, *J. Non-Cryst. Solids* **6**, 49 (1971).

45. K. Murase and T. Fukunaga, *Mat. Res. Soc. Symp. Proc.* **61**, 101 (1986).

46. R. J. Nemanich, *Phys. Rev. B* **16**, 1655 (1977).

47. E. Haro, Z. S. Xu, J. -F. Morhange, M. Balkanski, G. P. Espinosa, and J. C. Phillips, *Phys. Rev. B* **32**, 969 (1985).

48. S. Sugai, *Phys. Rev. Lett.* **57**, 456 (1986).

49. S. Sugai, *Phys. Rev. B* **35**, 1345 (1986).

50. E. A. Irene and H. Wiedemeier, *Z. anorg. allg. Chem.* **424**, 277 (1976).

51. O. Matsuda, K. Inoue, and K. Murase, *Solid State Commun.* **75**, 303 (1990).

52. K. Murase, K. Yakushiji, and T. Fukunaga, *J. Non-Cryst Solids* **59 & 60**, 855 (1983).

53. B. A. Weinstein, R. Zallen, M. L. Slade, and J. C. Mikkelsen, Jr., *Phys. Rev. B* **25**, 781 (1982).

54. K. Murase and T. Fukunaga, in *AIP Conf. Proc.* **120**, *Optical Effects in Amorphous Semiconductors, Snowbird, Utah*, ed. by P. C. Taylor and S. G. Bishop (American Institute of Physics, New York, 1984), p.449.

55. O. Matsuda, K. Inoue, and K. Murase, in *Proc. 20th Int. Conf. Phys. Semicond., Thessaloniki, Greece*, ed. by E. M. Anastassakis and J. D. Joannopoulos (World Scientific, Singapore, 1990), p.2135.

56. K. Inoue, O. Matsuda, and K. Murase, in *Proc. 19th Int. Conf. Phys. Semicond., Warsaw*, ed. by W. Zawadzki (Institute of Physics, Polish Academy of Sciences, 1988), p.1665.

57. K. Murase, K. Inoue, and O. Matsuda, *Atomic Processes Induced by Electronic Excitation in Non-Metallic Solids, Proc. US-Japan Seminar, Nagoya, Japan*, ed. by W. B. Fowler and N. Itoh (World Scientific, Singapore, 1990), *Rev. Solid State Sci.* **4**, 661 (1990).

58. S. Susman, K. J. Volin, D. G. Montague, and D. L. Price, *J. Non-Cryst. Solids* **125**, 168 (1990).

59. L. Červinka, *J. Non-Cryst. Solids* **97 & 98**, 207 (1987).